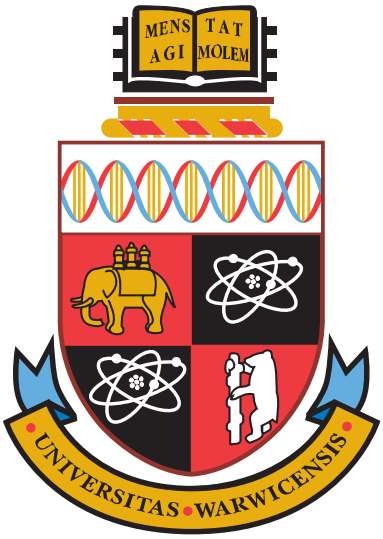

Ionisation Effects for Laser-Plasma Interactions by Particle-in-Cell Code

by

Alistair Lawrence-Douglas

Thesis

Submitted to the University of Warwick

for the degree of

Doctor of Philosophy

Department of Physics

April 2013

THE UNIVERSITY OF WARWICK

Contents

List of Tables

List of Figures

Acknowledgments

Firstly I would like to thank my supervisor Prof. Tony Arber for his insight and guidance throughout this study. I would also like to thank the EPSRC for the HEC studentship that made undertaking this Ph.D. possible. I would like to acknowledge Dr. Christopher Brady for providing helpful advice on numerous occasions and Dr. Keith Bennett for suffering the barrage of bug reports. The kind support from my friends and family has been invaluable, I would especially like to thank Siobhan Riley for the constant encouragement and the constant supply of tea. Finally I would like to mention my pet cat, Kupo Nut, for keeping me company during the later nights writing and who sadly passed away in the months leading up to submission.

Declarations

This thesis is my own work except where based upon collaborative research, in which case the nature and extent of my contribution has been indicated at the beginning of the relevant chapters. Some of the algorithms and results within this thesis have been published during the course of this Ph.D. or are otherwise awaiting publication. In particular, a condensed description of the field ionisation module and the results for laser filamentation in ionising hydrogen and plastic are included in Physics of Plasmas in June 2012, a collaborative publication with C.S. Brady and T.D. Arber at the University of Warwick [1]. In addition a description of the field and collisional ionisation module, the partial superparticle ionisation scheme, and the results for laser wakefield acceleration are soon to be submitted for publication in the Journal for Computational Physics. I also declare that this thesis has not been submitted for a degree at another university.

Abstract

The particle-in-cell code EPOCH was extended to include field and collisional ionisation for use in simulating initially neutral or partially-ionised targets in laser-plasma interactions. The means by which particles ionise in the the field of an intense laser was described and physical models were included to determine the instantaneous ionisation rate at particles within the simulation domain for multiphoton, tunnelling, barrier-suppression and electron-impact ionisation. The algorithms used to implement these models were presented and demonstrated to produce the correct ionisation statistics. A scheme allowing for modelling small amounts of ionisation for an arbitrarily low number of superparticles was also presented for comparison and it was shown that for sufficient simulation time the two schemes converge. The three major mechanisms of ionisation in laser-plasma interactions were described as being ionisation-induced defocussing, fast shuttering and ionisation injection. Simulations for these three effects were presented and shown to be in good agreement with theory and experiment. For fast-shuttering, plasma mirrors were simulated using the pulse profile for the Astra Gemini laser at the Central Laser Facility. Rapid switch-on and the theoretical maximum for contrast ratio was observed. For ionisation injection, simulations for laser wakefield acceleration in a helium gas were performed and the accelerated electron population was shown to be greatly increased through use of a 1% nitrogen dopant consistent with the experimental results of McGuffey *et al.* A study of the laser filamentation instability due to SRS backscatter at the relativistically corrected quarter critical surface (RCQCS) was performed in collaboration with C.S. Brady and T.D. Arber at the University of Warwick [1]. It was found that for hydrogen and plastic the instability was unaffected by the inclusion of ionisation. Further study with argon revealed a flattening of the RCQCS and it was demonstrated that for a material with multiple ionisation levels ionising strongly near the self-focussed intensities at the RCQCS, rapid ionisation caused an inversion of the RCQCS that suppressed the filamentation instability.

Abbreviations

ADK	-	Ammosov-Delone-Krainov
BSI	-	Barrier-Suppression Ionisation
CDF	-	Cumulative Distribution Function
DPM	-	Double Plasma Mirror
EM	-	Electromagnetic
EP	-	Electron Plasma
EPOCH	-	Extendable PIC Open Collaboration
FDTD	-	Finite Difference Time Domain
FWHM	-	Full-Width at Half Maximum
IA	-	Ion Acoustic
ICF	-	Inertial Confinement Fusion
LPCR	-	Laser Pulse Contrast Ratio
LWFA	-	Laser Wakefield Acceleration

MCF	-	Magnetic Confinement Fusion
MHD	-	Magnetohydrodynamics
NIF	-	National Ignition Facility
PDI	-	Plasma Decay Instability
PSC	-	Plasma Simulation Code
PWFA	-	Plasma Wakefield Acceleration
QED	-	Quantum Electron Dynamics
RCQCS	-	Relativistically Corrected Quarter Critical Surface
SBS	-	Stimulated Brillioun Scattering
SRS	-	Stimulated Raman Scattering
TPDI	-	Two-Plasmon Decay Instability
UHI	-	Ultra High Intensity
WKB	-	Wentzel-Kramers-Brillouin

Chapter 1

Introduction

Laser-plasma interaction is a uniquely diverse area of physics in which the time-scales, densities, and energies involved vary over such a range that even quantum electrodynamics has become involved in recent study [2]. With such complexity it comes as no surprise that some of the physical phenomena involved are analytically insoluble. In these cases it is necessary to turn to numerics via computation to seek approximate solutions. Computational plasma physics is therefore a rich and active area of study, and multiple methods exist for plasma modelling such as large scale fluid magnetohydrodynamic codes [3] to full kinetic simulations using Fokker-Planck equations [4].

The process by which neutral material becomes plasma in the field of an intense laser is one such interesting area of physics for which analytical methods may only be applied for the simplest linear systems, and usually only for hydrogen. Ionisation occurs both due to the strong electric field of a laser, and also due to particle collisions. Locally the ionised particles then influence the electric field or cause further ionisation via collision, and it is easy to see how the situation can become very non-linear.

Despite the fact that ionisation occurs on atomic time-scales it has still been demonstrated to produce significant consequences in laser-plasma interactions over much longer time-scales [5, 6]. Even the short time-scale behaviour is important when viewed in the context of plasma mirror, which depend on a fast sharp switch-on time [7]. It is also anticipated that ionisation will prove to be a significant consideration in the field of inertial confinement fusion (ICF) [8].

Particle-in-cell (PIC) codes are a very intuitive set of kinetic simulations for which charges are moved in a discretised spatial grid under the influence of their self-consistent electromagnetic field [9]. PIC is possibly the most widely applicable plasma simulation method, having been used to model the small scale laser-plasma interactions [10] and also much larger scale phenomena such as magnetic reconnection [11]. For such flexibility there is a price to pay; PIC is very computationally expensive compared to an MHD code using approximated transport coefficients. In the 60s this might have been reason enough to overlook PIC for anything beyond one-dimensional electrostatics but in recent decades computing has advanced to a point that relatively complex 2D simulations are viable on a standard desktop computer. PIC is in essence an old idea which is becoming more relevant over time.

This project concerns itself with the Extendable PIC Open Collaboration (EPOCH), a PIC code originally developed at the University of Warwick. Based on a pre-existing PIC algorithm, Hartmut Ruhl's PSC code [12], EPOCH is an established relativistic fully electromagnetic PIC code developed within the UK community and is available freely to all UK based academics. EPOCH comes in 1D, 2D and 3D versions operating on multiple processors for high end computing applications and is designed specifically to be readily extensible to include new physics. This makes it an ideal candidate for the inclusion and exploration of ionisation effects.

We will first seek to motivate the study of ionisation via computation in the context of one of the more exciting problems in laser-plasma physics; fusion power by laser confinement and ignition. The fundamental laser-plasma interactions will be explored in this context and theory of ionisation in an intense laser field will be outlined. Finally particle-in-cell codes will be described in depth including the specific method for resolving Maxwell's equations on a discretised grid; the finite-difference-time-domain. The following four chapters will go on to describe the implementation of ionisation in EPOCH, validating the ionisation module, ionisation effects in the parametric filamentation instability, and enhancement of electron acceleration.

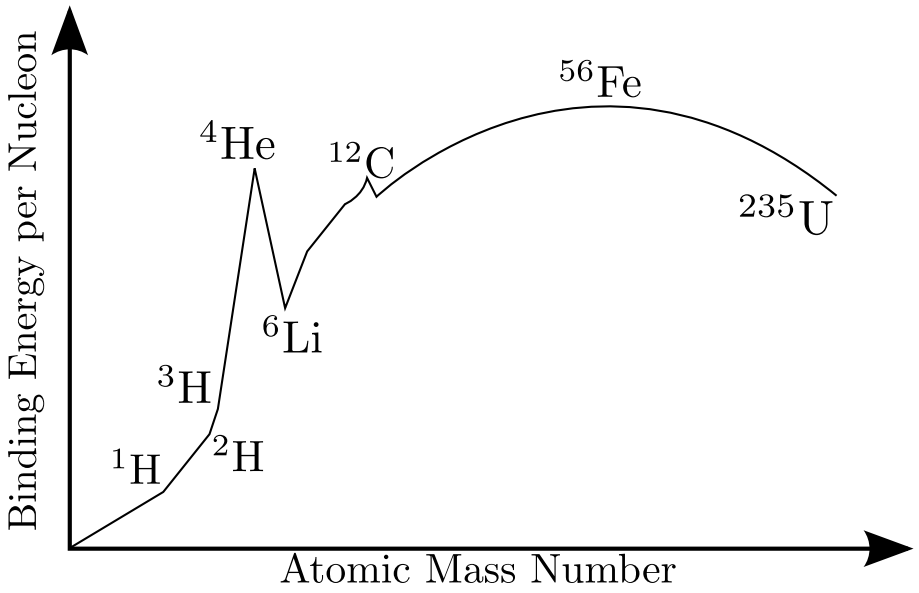

Figure 1.1: Sketch showing binding energy per nucleon against atomic mass number (arbitrary units).

1.1 Fusion

Fusion power represents a major goal for science in today's social and economic climate, in which our dependence on fossil fuels is increasing whilst our supplies are dwindling. Energy is released from fusion reactions when two nuclei collide and combine into a heavier element with a greater binding energy per nucleon. In fact our own Sun is primarily fuelled by the fusion of hydrogen isotopes. In fusion the mass of the products is smaller than the the rest mass of the reactants and the amount of energy released in this reaction can be found from this *mass defect* using the famous equation in physics; $E = mc^2$. This mass defect was first noted in the 1920s by Aston and the observation that this was how the Sun burned followed shortly thereafter by Eddington.

A demonstration of nuclear fusion followed somewhat explosively in 1951 with the use of fusion to enhance the fission reaction in a hydrogen bomb. However it has proven a far greater challenge to science to produce nuclear fusion in a controlled fashion that would be more applicable to a continuous power generation scheme. The difficultly arises from the activation energy required for nuclear fusion; since the nuclei must collide they must be moving fast enough to overcome Coulombic repulsion. This

is one of the reasons that research has focussed almost exclusively upon fusing two isotopes of hydrogen, since a hydrogen nucleus has the lowest charge of any element and therefore smallest Coulomb barrier to overcome. Another reason is that the fusion reactions between hydrogen isotopes produce helium which has an anomalously large binding energy per nucleon as demonstrated in Fig. 1.1, therefore the energy released per reaction is amongst the highest.

A critical point to realise is that the difficulty of controlled fusion is actually only an *indirect* consequence of the activation energy for the fusion reaction. It can be shown that the kinetic energy of the nuclei at which the reaction rate is maximised is ~ 100keV; current designs intend fusion reactors to operate at ~ 10keV but even heated up to these conditions the hydrogen isotopes will be in a hot plasma state [13]. This fact alone has driven much research in the field of plasma physics because plasmas have highly complex dynamics that make them difficult to contain. In the Sun the plasma *confinement* is achieved through gravity but on Earth we must settle for other methods; attempts to confine a plasma via application of magnetic fields started as early as 1938 before demonstration of the fusion bomb.

To continue exploring the containment of a fusion plasma it is important to discuss what we mean by confinement. Whilst it would be ideal if we could confine a fusion plasma indefinitely it can be acceptable for the plasma to be confined until we have gotten more energy out of the reactions than we spent heating up the reactants. However in general the goal is for the fusion process to generate enough heat that the plasma heating is primarily driven by the fusion reactions themselves, a condition known as *ignition*. To derive these conditions we explore them in the context of a deuterium-tritium fusion reaction. This has the greatest achievable reaction rate of all the isotopes of hydrogen, whilst deuterium itself is naturally abundant and tritium is readily produced in situ. The reaction can be given as,

$$^{2}_{1}\mathrm{D} + ^{3}_{1}\mathrm{T} \rightarrow ^{4}_{2}\mathrm{He} + ^{1}_{0}\mathrm{n} + 17.6\mathrm{MeV} \tag{1.1}$$

The energy released in the reaction is divided between the neutron particle (14.06MeV) and the alpha particle (3.52MeV) [13]. The reaction rate per unit vol-

ume of the D-T reaction can be written as $n_{\mathsf{D}} n_{\mathsf{T}} \langle \sigma v \rangle$ where n_{D} and n_{T} are the number density of deuterium and tritium respectively, σ is the cross section for D-T fusion, and v is the mean velocity of the nuclei. For this reaction we assume that deuterium and tritium are therefore mixed in equal densities. We also assume quasi-neutrality such that $n_D + n_T = n_e = n$. From this we can write the total power produced in fusion within volume V,

$$P_{\mathsf{fusion}} = \frac{1}{4} n^2 \langle \sigma v \rangle_{\mathsf{DT}} E_{\mathsf{fus}} V \tag{1.2}$$

To consider the power required to heat the plasma P_{heat} we introduce the time taken τ for the plasma to lose energy W; we can then write the net change in energy as,

$$\frac{\partial W}{\partial t} = -\frac{W}{\tau} + P_{\mathsf{heat}} \tag{1.3}$$

This time τ is known as the *energy confinement time* and loosely describes a number of physical processes by which the plasma loses energy. We wish to find the heating power for the break-even condition such that the heating balances the energy loss from the plasma. Particles in the plasma have energy $^3/_2 T$ where we use the plasma physics convention $T \to k_b T$ with k_b the Boltzmann constant. Therefore the energy in the volume of the plasma we have that for constant temperature and density,

$$\int W dV = \int \left(\frac{3}{2} n_D T_D + \frac{3}{2} n_T T_T + \frac{3}{2} n_e T_e \right) dV = 3nT \int dV = 3nTV \tag{1.4}$$

For steady state we require that $^{\partial W}/_{\partial t} = 0$,

$$nT = \frac{1}{3V} P_{\mathsf{heat}} \tau \tag{1.5}$$

Substituting Eq. (1.2) into Eq. (1.5),

$$\frac{P_{\text{fusion}}}{P_{\text{heat}}} = \frac{n \langle \sigma\nu \rangle_{\text{DT}} E_{\text{fus}} \tau}{12T} \tag{1.6}$$

Over the typical temperature range of for fusion of D-T the cross section for the reaction given by Eq. (1.1), around $8 - 25$keV, the cross-section can be fitted by $\langle \sigma v \rangle_{\text{DT}} \approx 1.1 \times 10^{-24} T^2 \text{m}^3\text{s}^{-1}$ [14].

$$\frac{P_{\text{fusion}}}{P_{\text{heat}}} = 1.6 \times 10^{-20} nT\tau \tag{1.7}$$

The factor of $nT\tau$ gets referred to as the *triple product* [13] and is an important metric for determining the requirements of a fusion power scheme. Using Eq. (1.7) we can find the *break-even* condition $P_{\text{fusion}} = P_{\text{heat}}$; the point at which the energy used to heat the plasma is balanced by the energy produced by the fusion reactions resulting in no net loss (or gain) of energy [8]. The ignition condition can also be found; for this we first assume that only alpha particles heat the plasma whilst neutrons provide the energy output through some means [13]. This is because the alpha particles have a very short mean free path within the plasma compared to the neutrons and are much less likely to escape. Reviewing the kinetic energies of each particle following a D-T fusion we see that the alpha particles carry approximately a fifth of the energy, therefore $P_{\text{fusion}} > 5P_{\text{heat}}$ for ignition.

1.1.1 Inertial Confinement

Temperature is largely dictated by the requirements of the fusion reactions. Schemes for fusion tend to vary only the plasma densities used and the energy confinement time for the method. However there are vast differences in the governing physics when deriving fusion power from gas density compared to solid density. There are two schemes which attract the most research into the confinement of plasma; ICF, and magnetic confinement fusion (MCF). The former operates with very high densities and short energy confinement time, whereas the latter uses relatively low densities but a long energy confinement time.

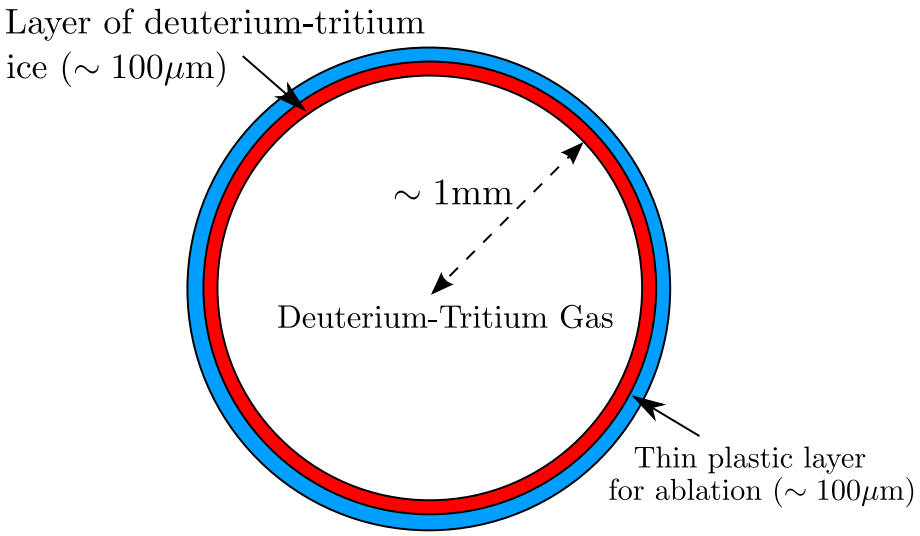

Figure 1.2: Basic sketch illustrating the general deuterium-tritium target design concept [8].

MCF seeks to shape the plasma through applied magnetic fields such that it is effectively confined indefinitely if the fields can be sustained. Conversely ICF seeks to create plasma so dense such that all the fusion reactions occur in a very short time frame [15]. In this way a net energy output is produced before the plasma can overcome its own inertia and fly apart [8]. In MCF numerous instabilities can destroy confinement but in ICF the time-scale is smaller than that of most of these instabilities. However this scheme suffers its own issues, as the density required is several hundred times solid density of deuterium and tritium [8]. Achieving these densities therefore requires compression of the fuel which in current schemes involves implosion of a deuterium-tritium target of the form shown in Fig. 1.2. This is achieved via high powered lasers imploding the target [8]. For this reason, ICF is possibly the most prolific laser-plasma interaction application, with major experiments still occurring at the National Ignition Facility (NIF) in California, US with ignition expected by 2013 [16].

The typical process for ICF is as follows; driver energy is applied through some means to the plastic surface of the deuterium-tritium target. The plastic surface heats, vaporises and blows off the target in a process known as *ablation* [8]. Conservation of momentum implies that the fuel is driven to the centre of the target which serves to both compress and heat the fuel to the conditions required for fusion. The fusion

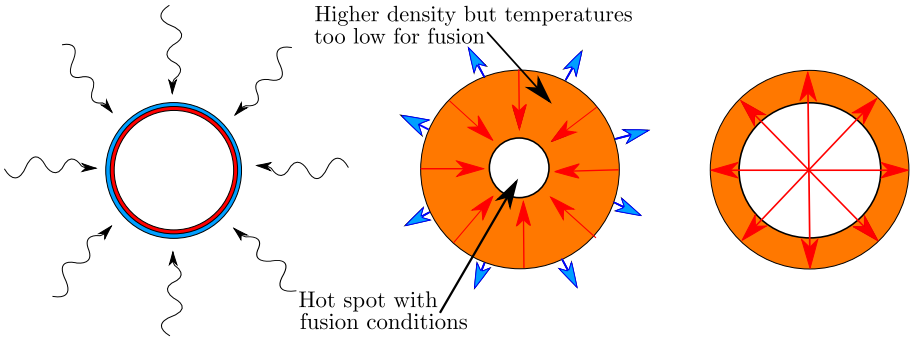

Figure 1.3: Laser compresses the deuterium-tritium target, resulting in a hot spot of fuel undergoing fusion. The hot spot expands with a thermonuclear burn front. [8]

reactions oppose the compression and eventually cause the fuel to explode outwards; the time it takes for this to occur is the *disassembly time* and so this will be a function of the target radius.

The compressed sphere freely expands at the sound speed $C_S = \sqrt{4T/(m_\mathrm{D}+m_\mathrm{T})}$ where m_D and m_T are the mass of the deuterium and tritium ions respectively. The energy confinement time is taken to be the time it takes for the volume of the sphere to double such that $\tau \approx R/4C_S$ [8]. There can be no "breaking-even" in such a scheme as there is no external heating; the heat required to drive the fusion must be produced by the reactions themselves. In other words, ignition is required in the ICF scheme. Due to the role of radius in confinement and fuel mass in the speed of expansion it is typical to re-express the criteria for ignition in terms of the radius and the fuel density $\rho = nm$ as this yields the actual compressed fuel density requirement. From Eq. (1.7) and the ignition requirement,

$$\rho R > 1.25 \times 10^{21} \frac{C_S m}{T} \tag{1.8}$$

An estimate for ignition and efficient burning of the D-T fuel is given by [8],

$$\rho R \approx 0.3 \mathrm{gcm}^{-2} \tag{1.9}$$

The compression and ignition of the D-T fuel are two distinct stages in ICF and there are multiple schemes which separate them. It would be simplest to be able

to simultaneously compress and heat all of the fuel to the required fusion conditions, indeed this method is known as *volume ignition* and was initially sought in the 1970s [8]. However it is energetically more expensive to heat rather than compress fuel and also to compress hot rather than cold fuel. As such the driver energy requirements were estimated at ∼60MJ [17] which is unfeasible with today's laser technology; the most powerful laser currently being used in the development of ICF produces 1.8MJ [8]. As such common schemes use the *hot-spot concept* whereby the fuel is compressed such that fusion conditions are reached in the centre only, then a thermonuclear burn front propagates out to the rest of the fuel as shown in Fig. 1.3. This scheme is far more efficient than volume ignition as it avoids unnecessary heating of the fuel, and is in fact estimated to only require ∼1-2MJ driver energy [8].

1.1.2 Target Design and Indirect Drive at the National Ignition Facility

The energy requirements for hot-spot ignition whilst much smaller than that of volume ignition still present a significant challenge to present laser technology. The laser at the national ignition facility runs at a driver energy of 1.8MJ [18] and so in principle should achieve ignition, but the target must be illuminated uniformly which is difficult to achieve without a very large number of lasers. Partial illumination of the target results in uneven implosion which can result in the loss of symmetry and drive instabilities leading to energy or fuel loss. One such mechanism is the Rayleigh-Taylor instability [19] which can be observed when a heavier liquid sits upon a lighter liquid; the heavier penetrates into the lighter in a spike resulting in mixing. This can be initiated by the unsymmetrical target implosion and in the case of ICF this would result in the ablation material mixing with the deuterium and tritium, reducing the amount of fusion material compressed into the core.

Even with the 192 laser banks available to shine onto the target at NIF [18], breaks in symmetry are a concern. For this reason NIF's primary focus is upon the *indirect drive* scheme illustrated in Fig. 1.4, so called due to the laser being directed upon a gold *hohlraum*. This is essentially a hollow cylinder with windows at either end to allow laser light entrance. The gold efficiently absorbs and re-emits the laser energy providing even illumination and eliminating many symmetry issues. This scheme

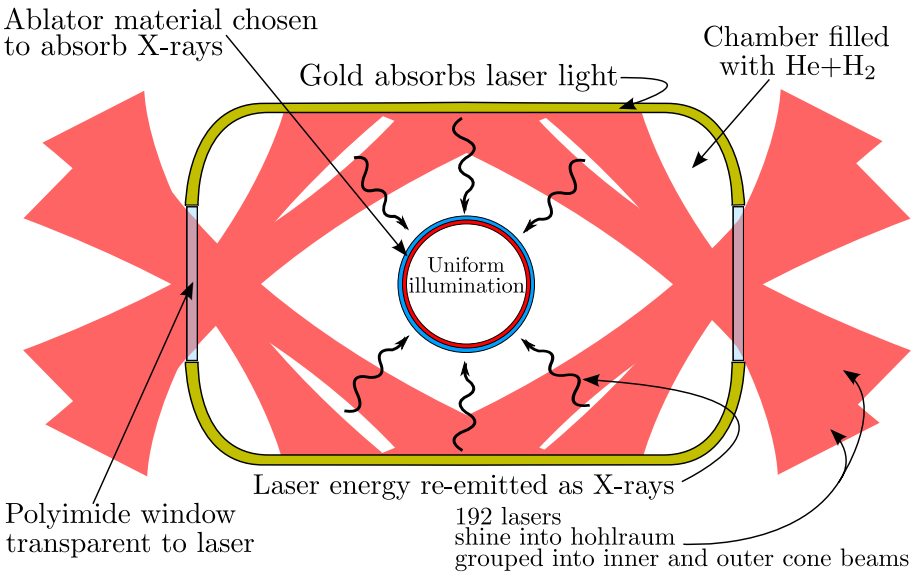

Figure 1.4: The indirect drive scheme proposed at NIF; the laser light is focussed upon the inside of a gold hohlraum with a deuterium tritium target contained in the centre [18]. The gold absorbs and re-emits the laser energy uniformly in the form of X-rays which provides a more even illumination of the target surface.

comes with its own drawbacks; to absorb the X-rays the target ablator must be carefully considers with current designs either using beryllium or otherwise doping with similar substances. This makes the ablating layer heavier which exacerbates any Rayleigh-Taylor instabilities. Whilst these are significantly reduced by the improved symmetry but makes the target highly sensitive to manufacturing defects; any deviation from a perfect spherical shape must be $< 0.1\%$ [8].

1.1.3 Fast Ignition

Another approach being taken to ICF design is to further reduce driver energy using a concept known as *fast ignition*. The goal is to separate compression and heating such that the driver energy requirements are reduced even further, though this does serve to increase the complexity of the scheme. The model concept for this is to use a conventional laser to compress the fuel and then use a secondary laser to directly ignite the core; this is illustrated in Fig. 1.5. The primary issue in this scheme is how to pulse the laser through the corona to the dense fuel in the centre. Two primary methods exist; hole boring and laser cone guiding [8]. The former attempts to fire the laser directly

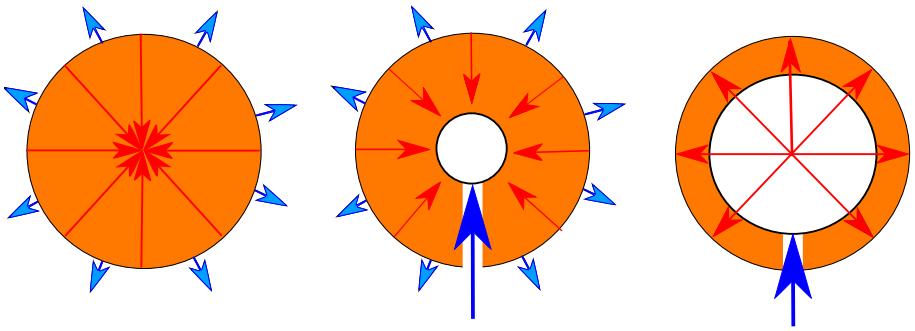

Figure 1.5: Laser compresses the deuterium-tritium target without hot spot formation. Laser pulse bores to the fuel core to heat the core directly to form hotspot. The fuel then ignites as before though with significantly lower energy input. [8]

into the core in a high intensity pulse, penetrating the corona. Experiments have been performed to this end and though the pulsing laser showed increased neutron yield, it was not clear if this was from fusion in the core or away from it at the critical surface where the laser energy was deposited [20]. Laser cone guiding bypasses hole-boring issues by placing the deuterium-tritium target on the tip of a hollow gold cone such that the tip touches the core. The laser compression is still done conventionally but then the ignition pulse is fired into the back of the cone, this ionises the gold such that fast electrons are produced near the core of target [21].

1.2 Laser-Plasma Interactions

The potential for fusion by laser ignition as a new energy source provides a strong motivator for research into the interaction of laser light with plasma. It also provides a useful context in which to describe the physical processes by which the laser light is absorbed as shown in Fig. 1.6. In this section we seek to illustrate some important instabilities arising from non-linear coupling of laser energy to the plasma and to outline the process of ionisation in the field of an intense laser as a primer to this project. The impact of the instabilities in laser-plasma interactions upon ICF ranges from universally detrimental to potentially exploitable in certain designs. In chapter 5 we will explore a fundamental and detrimental instability in which the plasma couples the laser to a backwards travelling EM wave (stimulated Raman scattering) which serves to cause loss of symmetry and drive further instabilities [1]; this in particular is an issue for direct drive. At the end of §.1.2.1 we will also briefly explore the effect of crossed-beam energy transfer [22] in which the energy of crossed laser beams becomes unstably coupled via a plasma wave (stimulated Brillouin scattering) which can break symmetry in hohlraum illumination. This would seem to be an issue isolated to indirect drive but studies by Igumenshchev *et al.* [23] demonstrate its relevance to direct drive. Crossed-beam energy transfer is an interesting case where research has turned to exploiting the instability rather than mitigating it, as the energy transfer can be used to fine tune the symmetry of the laser beams entering the hohlraum [24, 25]. To explore laser-plasma interactions we need to know what waves propagate in a plasma and how they interact with each other, and so first we shall briefly review the *two-fluid* description of a plasma from which these waves can be derived.

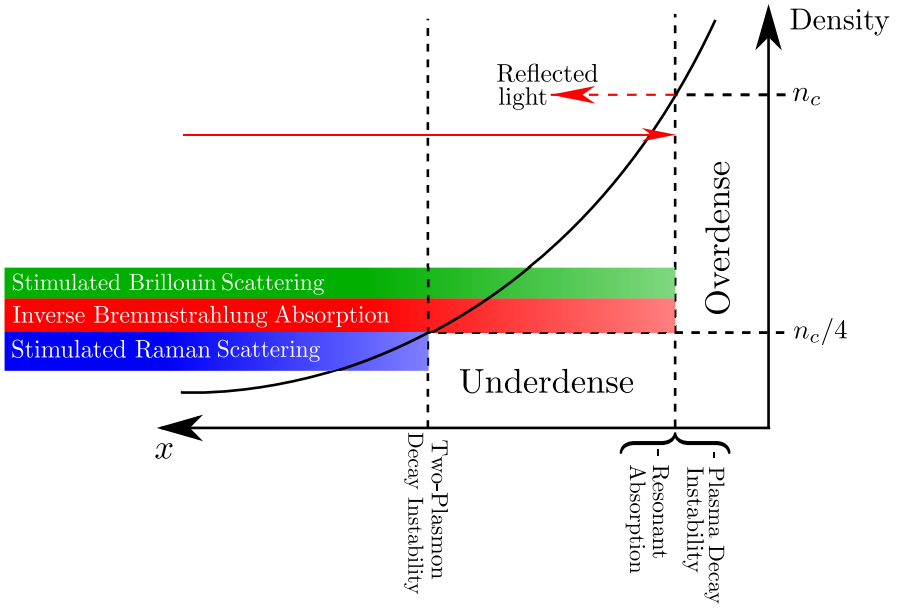

Figure 1.6: The means by which laser energy couples to the plasma is dependent on the density of the plasma. When the laser is incident upon the fusion target it will encounter a density ramp and experience different absorption processes at different densities. Most occur between the quarter critical and critical surface; the processes and the density they occur at are illustrated above. [8]

First we define the *phase space distribution function* $f(\mathbf{x}, \mathbf{v}, t)$ which provides the number density of particles which are at position $\mathbf{x}$ and moving at velocity $\mathbf{v}$ at time t. We can find macroscopic quantities for the plasma (density, mean velocity, pressure, heat flow, etc.) by integrating the distribution function over the phase space, for example the density at $\mathbf{x}$ and time t is found simply by integrating $f(\mathbf{x}, \mathbf{v}, t)$ over the velocity. This macroscopic quantities are called *moments* of the distribution function. The first three moments are given by [26],

$$\begin{aligned} n &= \int f(\mathbf{x}, \mathbf{v}, t)\, d\mathbf{v} \\ \mathbf{u} &= \frac{\int \mathbf{v} f(\mathbf{x}, \mathbf{v}, t)\, d\mathbf{v}}{n} \\ \underline{\underline{\mathbf{P}}} &= m \int (\mathbf{v} - \mathbf{u})(\mathbf{v} - \mathbf{u}) f(\mathbf{x}, \mathbf{v}, t)\, d\mathbf{v} \end{aligned} \tag{1.10}$$

Particles with positive v_{i} ($\mathbf{v} = (v_x, v_y, v_z)$) in the phase space always move positively in x_{i}, similarly we define the acceleration $\mathbf{a}(\mathbf{x}, \mathbf{v}, t)$ which gives the motion in $\mathbf{v}$. Assuming continuity in the phase space such that particles are neither created or destroyed then the considering the flow of particles into and out of a volume of the phase space, we can find the *Vlasov equation* which describes the time evolution of a collisionless plasma [27]. This is given below for the relativistic case where $\gamma = \sqrt{1 + \mathbf{v}^2/c^2}$ [28],

$$\frac{\partial f}{\partial t} + \frac{\partial}{\partial \mathbf{x}} \cdot \left(\frac{\mathbf{v}}{\gamma} f \right) + \frac{\partial}{\partial \mathbf{v}} \cdot \left(\frac{\mathbf{a}}{\gamma} f \right) = 0 \tag{1.11}$$

Particle motion is driven by the electromagnetic fields in the plasma, so acceleration $\mathbf{a}$ is given by the relativistic Lorentz force $\mathbf{a} = {}^{q}/_{m} (\mathbf{E} + {}^{\mathbf{v}}/_{\gamma} \times \mathbf{B})$. Using this and the fact that $\mathbf{v}$ is independent of $\mathbf{x}$ and $(\mathbf{v} \times \mathbf{B})_{\mathrm{i}}$ is independent of v_{i} we can rewrite the Vlasov equation as [27],

$$\frac{\partial f}{\partial t} + \frac{\mathbf{v}}{\gamma} \cdot \frac{\partial f}{\partial \mathbf{x}} + \frac{q}{m} \left(\mathbf{E} + \frac{\mathbf{v}}{\gamma} \times \mathbf{B} \right) \cdot \frac{\partial f}{\partial \mathbf{v}} = 0 \tag{1.12}$$

For a plasma containing multiple species there will be a separate distribution function $f_i(\mathbf{x}, \mathbf{v}, t)$ for each species i and therefore one Vlasov equation per species required for a full system of equation. By taking moments of the Vlasov equation instead of the distribution function we find that the change in density depends on the mean velocity, and the change in velocity depends on the pressure. In fact, infinite higher order moments can be found and each will have the next higher order moment as a term [26]. Using this fact it is possible to build up a set of relationships between the macroscopic quantities shown in Eq. (1.10). However it is necessary to include an approximation for one of the higher order terms so as to have a tractable system of equations. In this case it is typical to enforce either an isothermal or adiabatic equation of state for the pressure term so as to neglect heat flow [8].

In the adiabatic case we neglect the heat flow by assuming it is much slower than the process under consideration, in which case the second moment of the Vlasov equation reduces to $p = Cn^{(2+N)/N}$ where C is some constant and N is the number

of degrees of freedom. To consider the isothermal case where we instead assume that the heat flow occurs quickly compared to the physical process of interest, this also requires inclusion of collisions in the Vlasov equation. In this case the temperature can be considered constant in the plasma; under this assumption the second moment of the Vlasov equation instead reduces to the ideal gas approximation $p = nk_bT$ [26]. The zeroth and first moments follow without any further assumption and the use of the isothermal or adiabatic pressure reduces $\underline{\underline{\mathbf{P}}}$ to a scalar in the velocity moment. The following equations include Maxwell's equations and completes the *two-fluid* model for the non-relativistic case where subscript i denotes ions of atomic number Z and e denotes electrons [26],

$$\begin{aligned}
&\frac{\partial n_\mathrm{i}}{\partial t} + \frac{\partial}{\partial \mathbf{x}} \cdot (n_\mathrm{i}\mathbf{u}_\mathrm{i}) = 0 && \frac{\partial n_e}{\partial t} + \frac{\partial}{\partial \mathbf{x}} \cdot (n_e\mathbf{u}_e) = 0 \\
&n_\mathrm{i}m_\mathrm{i}\left(\frac{\partial \mathbf{u}_\mathrm{i}}{\partial t} + \mathbf{u}_\mathrm{i} \cdot \frac{\partial \mathbf{u}_\mathrm{i}}{\partial \mathbf{x}}\right) = && n_e m_e\left(\frac{\partial \mathbf{u}_e}{\partial t} + \mathbf{u}_e \cdot \frac{\partial \mathbf{u}_e}{\partial \mathbf{x}}\right) = \\
&\quad n_\mathrm{i}Ze\left(\mathbf{E} + \mathbf{u}_\mathrm{i} \times \mathbf{B}\right) - \frac{\partial p_\mathrm{i}}{\partial \mathbf{x}} && \quad - n_e e\left(\mathbf{E} + \mathbf{u}_e \times \mathbf{B}\right) - \frac{\partial p_e}{\partial \mathbf{x}} \\
&\nabla \times \mathbf{E} = -\frac{\partial \mathbf{B}}{\partial t} && \nabla \times \mathbf{B} = \mu_0\mathbf{J} + \mu_0\epsilon_0\frac{\partial \mathbf{E}}{\partial t} \\
&\nabla \cdot \mathbf{E} = \frac{\rho}{\epsilon_0} && \nabla \cdot \mathbf{B} = 0
\end{aligned} \tag{1.13}$$

This constitutes a complete description of the evolution of a plasma where $\rho = n_\mathrm{i}Ze - n_e e$ and $\mathbf{J} = n_\mathrm{i}Ze\mathbf{u}_\mathrm{i} - n_e e\mathbf{u}_e$. Note that the form of scalar pressure p depends upon whether the adiabatic or isothermal assumption applies. Many dispersion relations for different waves supported by the plasma follow from these three combined sets of equations. Here we focus on three fundamental plasma waves; electromagnetic waves from the self-consistent Maxwell's equations in a plasma, low frequency ion acoustic waves from the fluid description of the ions and higher frequency electron plasma waves from the fluid description of the electrons.

For considering the high frequency electron motion we treat the ions as stationary as their motion will vary slowly compared to the electrons. We also assume an unmagnetised plasma such that rotation in the Lorentz force is eliminated. This allows us to proceed with a simple one-dimensional analysis to find the electron plasma waves [29]. Also note that these assumptions imply that the electron plasma wave is purely

electrostatic. Assuming small perturbations in the electron position, we make use of a technique called *linearisation* to approximate the motion. We can always write a function $f(x_1, x_2, x_3, \dots)$ as a sum of some constant $f_0 = f\left(x_1^{(0)}, x_2^{(0)}, x_3^{(0)}, \dots\right)$ and a perturbation $\tilde{f}(x_1, x_2, x_3, \dots) = f - f_0$. We apply this to the 1D fluid equations for the electrons whilst picking the isothermal pressure and the equilibrium electron density n_{0e} as the constant value for the pressure and density respectively. The perturbed physical parameters are then $n_e = n_{0e} + \tilde{n}_e$, $u_e = \tilde{u}_e$, $p_e = n_{0e}k_bT_e + \tilde{p}$, and $E = \tilde{E}$. We then *linearise* the equation by noting that if the perturbations are small then the product of any perturbations can be neglected; this produces linear equations,

$$\frac{\partial \tilde{n}_e}{\partial t} + n_{0e}\frac{\partial \tilde{u}_e}{\partial x} = 0 \qquad n_{0e}m_e\frac{\partial \tilde{u}_e}{\partial t} = -n_{0e}e\tilde{E} - \frac{\partial \tilde{p}_e}{\partial x} \tag{1.14}$$

Eliminate $\tilde{u}_e$ by differentiating the density-velocity relation and the velocity-pressure relation with respect to t and x respectively, and also substitute $\tilde{E}$ with Gauss' law noting that $n_{0e} = Zn_{0\mathrm{i}}$ for quasi-neutrality giving $\rho = -e\tilde{n}_e$,

$$\begin{gathered}\frac{\partial^2 \tilde{n}}{\partial t^2} + n_{0e}\frac{\partial \tilde{u}_e}{\partial x \partial t} = 0 \qquad n_{0e}m_e\frac{\partial \tilde{u}_e}{\partial x \partial t} = -n_{0e}e\frac{\partial \tilde{E}}{\partial x} - \frac{\partial^2 \tilde{p}_e}{\partial x^2} \qquad \frac{\partial \tilde{E}}{\partial x} = -\frac{e\tilde{n}_e}{\epsilon_0} \\ \Rightarrow \frac{\partial^2 \tilde{n}}{\partial t^2} + \frac{n_{0e}e^2}{\epsilon_0 m_e}\tilde{n}_e = \frac{1}{m_e}\frac{\partial^2 \tilde{p}_e}{\partial x^2}\end{gathered} \tag{1.15}$$

We now seek to eliminate the pressure term. For the high frequency electron plasma waves we assume that $\omega/k \gg v_e$ where $v_e = \sqrt{k_bT_e/m_e}$ is the electron thermal velocity with T_e the temperature of the electrons [26]. Therefore we use the 1D adiabatic pressure $p_e = Cn_e^3$,

$$\begin{gathered}\frac{\partial}{\partial x}\left(\frac{n_{0e}k_bT_e + \tilde{p}_e}{n_{0e} + \tilde{n}_e}\right) = 0 \Rightarrow 3\left(n_{0e}k_bT_e + \tilde{p}_e\right)\frac{\partial \tilde{n}_e}{\partial x} = \left(n_0 e + \tilde{n}_e\right)\frac{\partial \tilde{p}_e}{\partial x} \\ \text{Linearising, } \frac{\partial \tilde{p}_e}{\partial x} = 3k_bT_e\frac{\partial \tilde{n}_e}{\partial x} \Rightarrow \frac{\partial^2 \tilde{p}_e}{\partial x^2} = 3k_bT_e\frac{\partial^2 \tilde{n}_e}{\partial x^2}\end{gathered} \tag{1.16}$$

Finally we eliminate $\tilde{p}_e$ using the above and apply a plane wave solution such that $\tilde{n} = A\exp(ikx - i\omega t)$ where A is a constant and $i = \sqrt{-1}$ to arrive at the dispersion relation,

$$\frac{\partial^2 \tilde{n}_e}{\partial t^2} = 3\frac{k_b T_e}{m_e}\frac{\partial^2 \tilde{n}_e}{\partial x^2} - \frac{n_{0e}e^2}{\epsilon_0 m_e}\tilde{n}_e \Rightarrow \omega^2 = \frac{n_{0e}e^2}{\epsilon_0 m_e} + 3\frac{k_b T_e}{m_e}k^2 \tag{1.17}$$

Rewriting the above result in terms of the electron thermal velocity and the electron plasma frequency $\omega_{\mathsf{pe}} = \sqrt{n_e e^2/m_e\epsilon_0}$ we find the common form for the dispersion relation of electron plasma waves [8],

$$\omega_{\mathsf{EP}}^2 = \omega_{\mathsf{pe}}^2 + 3k^2 v_e^2 \tag{1.18}$$

The method to find the lower frequency ion density oscillations is similar to that for electron plasma waves Eq. (1.14). Once again we use an unmagnetised plasma and 1D analysis, so this too is an electrostatic wave. The response of the electrons to any change in the system will be fast compared to the ion oscillations, so we can begin by neglecting the electron inertia ($m_e \approx 0$) and note that in this case $\omega/k \ll v_e$ such that an isothermal equation of state $p_e = n_e k_b T_e$ applies for the electron pressure. This reduces the linearised velocity moment of Eq. (1.14) to,

$$\tilde{E} = -\frac{k_b T_e}{n_{0e}e}\frac{\partial \tilde{n}_e}{\partial x} \tag{1.19}$$

For the ion thermal velocity v_{i} we have that $\omega/k \gg v_{\mathsf{i}}$ and so the pressure is found as in Eq. (1.18). We use the results for the electric field and the ion pressure and linearise the ion fluid equations as before to arrive at the dispersion relation [26],

$$\begin{gathered}\frac{\partial^2 \tilde{n}_{\mathsf{i}}}{\partial t^2} + \frac{Zen_{0\mathsf{i}}}{m_{\mathsf{i}}}\frac{\partial \tilde{E}}{\partial x} = \frac{1}{m_{\mathsf{i}}}\frac{\partial^2 \tilde{p}_{\mathsf{i}}}{\partial x^2} \Rightarrow \frac{\partial^2 \tilde{n}_{\mathsf{i}}}{\partial t^2} - \frac{k_b T_e}{m_{\mathsf{i}}}\frac{\partial^2 \tilde{n}_e}{\partial x^2} = 3\frac{k_b T_{\mathsf{i}}}{m_{\mathsf{i}}}\frac{\partial^2 \tilde{n}_{\mathsf{i}}}{\partial x^2} \\ \tilde{n}_e \approx Z\tilde{n}_{\mathsf{i}} \Rightarrow \frac{\partial^2 \tilde{n}_{\mathsf{i}}}{\partial t^2} = \frac{Zk_b T_e + 3k_b T_i}{m_i}\frac{\partial^2 \tilde{n}_{\mathsf{i}}}{\partial x^2}\end{gathered} \tag{1.20}$$

Applying the plane wave solution once more, we rewrite the dispersion relation for ion acoustic waves in terms of the *ion-sound* velocity $v_s = \sqrt{\left(Zk_bT_e + 3k_bT_\mathrm{i}\right)/m_\mathrm{i}}$,

$$\omega_{\mathsf{IAW}} = \pm k v_s \tag{1.21}$$

The dispersion relation for electromagnetic waves in the plasma starts with the same assumptions as for Langmuir waves as it is assumed $\omega \geq \omega_{\mathsf{pe}}$, however we must consider three dimensions. Under the perturbations used previously plus $\mathbf{B} = \tilde{\mathbf{B}}$ we have that the current density is $\tilde{\mathbf{J}} = n_{0\mathrm{i}} e \tilde{\mathbf{u}}_\mathrm{i} - \left(n_{0e} + \tilde{\mathbf{n}}_e\right) e \tilde{\mathbf{u}}_e$ but immobile ions gives $\tilde{\mathbf{u}}_\mathrm{i} \approx 0$ and products of perturbations are small, therefore $\tilde{\mathbf{J}} = -n_{0e} e \tilde{\mathbf{u}}_e$. We also approximate the plasma as being cold allowing us to neglect pressure perturbation, which reduces the velocity moment of the Vlasov equation to simply,

$$\frac{\partial \tilde{\mathbf{u}}_e}{\partial t} = -\frac{e}{m_e}\left(\tilde{\mathbf{E}} + \tilde{\mathbf{u}}_e \times \tilde{\mathbf{B}}\right) = -\frac{e}{m_e}\tilde{\mathbf{E}} \tag{1.22}$$

Eliminating the current density from Ampere's law and taking our plane wave solution for the electromagnetic wave we get,

$$\frac{\partial \tilde{\mathbf{J}}}{\partial t} = \frac{n_{0e}e^2}{m_e}\tilde{\mathbf{E}} \Rightarrow \tilde{\mathbf{J}} = -\frac{n_{0e}e^2}{i\omega m_e}\tilde{\mathbf{E}} \tag{1.23}$$

Using this and the curl of Faraday's law to eliminate $\tilde{\mathbf{B}}$ from Ampere's law, we assume a plasma of uniform density such that $\nabla\left(\nabla \cdot \tilde{\mathbf{E}}\right) = 0$ to find the dispersion relation for an electromagnetic wave in the plasma [26],

$$\begin{aligned}
&\nabla \times \tilde{\mathbf{E}} = -\frac{\partial \tilde{\mathbf{B}}}{\partial t} = i\omega \tilde{\mathbf{B}} \Rightarrow \nabla\left(\nabla \cdot \tilde{\mathbf{E}}\right) - \nabla^2 \tilde{\mathbf{E}} = i\omega \nabla \times \tilde{\mathbf{B}} \\
&\frac{1}{i\omega}\nabla\left(\nabla \cdot \tilde{\mathbf{E}}\right) - \nabla^2 \tilde{\mathbf{E}} = \mu_0 \tilde{\mathbf{J}} + \mu_0 \epsilon_0 \frac{\partial \tilde{\mathbf{E}}}{\partial t} = \left(-\frac{\mu_0 n_{0e} e^2}{i\omega m_e} - \mu_0 \epsilon_0 i\omega\right)\tilde{\mathbf{E}} \\
&\Rightarrow c^2 \nabla^2 \tilde{\mathbf{E}} - c^2 \nabla\left(\nabla \cdot \tilde{\mathbf{E}}\right) + \left(\omega^2 - \omega_{\mathsf{pe}}^2\right)\tilde{\mathbf{E}} = 0 \Rightarrow \left(\omega^2 - \omega_{\mathsf{pe}}^2 - k^2 c^2\right)\tilde{\mathbf{E}} = 0 \\
&\Rightarrow \omega^2 = \omega_{\mathsf{pe}}^2 + k^2 c^2
\end{aligned} \tag{1.24}$$

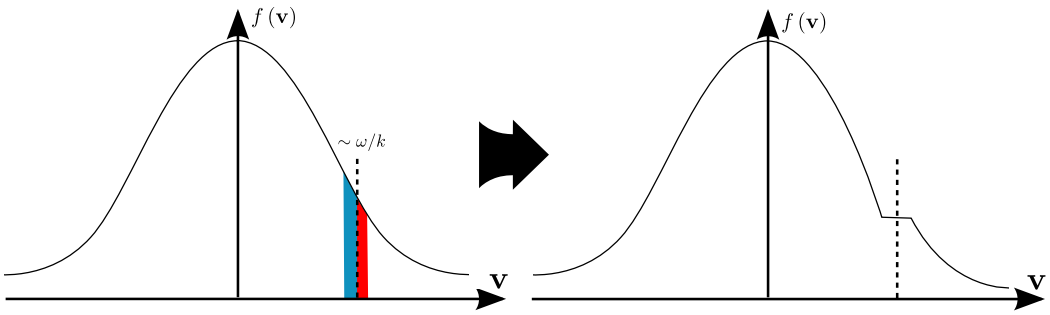

Figure 1.7: The energy exchange between the particles and the electrostatic wave has the effect of flattening the particle velocity distribution near the phase velocity w/k of the wave. If this is at a downward slope in the distribution then the net effect is to increase the energy of the particles. This exaggerated illustration demonstrates the effect of *Landau damping*.

Note that the EM plasma waves are the only waves capable of leaving the plasma. Langmuir and ion acoustic waves therefore remain in the plasma and eventually lose their energy to damping mechanisms. Two examples of electrostatic wave damping are collisional and Landau damping [26]. Collisional damping occurs due to electron-ion collisions and therefore damps an electron plasma wave by thermalising the electron oscillations. This is also a direct mechanism for the plasma to absorb laser energy; when under an applied electric field the electrons will oscillate and if they then collide the energy is thermalised. In this case the collisional damping is called inverse Bremmstrahlung, so named because a photon is absorbed during scattering [8].

Landau damping does not rely on collision but instead resonance with the electrostatic wave meaning that only particles with $v \approx \omega/k$ are influenced. Qualitatively, particles resonant with the electrostatic wave will exchange energy with it more effectively. If a particle is moving slightly faster than the resonant velocity and slows towards it then it loses energy to the electrostatic wave. Conversely if a particle is moving slower and approaches resonance it will gain energy. It is important to note that particles are not drawn towards the resonant velocity, but as they oscillate in the plasma they will periodically approach it. Therefore if there are more particles accelerating up towards the resonant velocity than decelerating down to it during their oscillation in the plasma then on average the particles will be gaining energy. As such the overall effect of Landau damping is entirely due to the shape of the distribution function of the particle

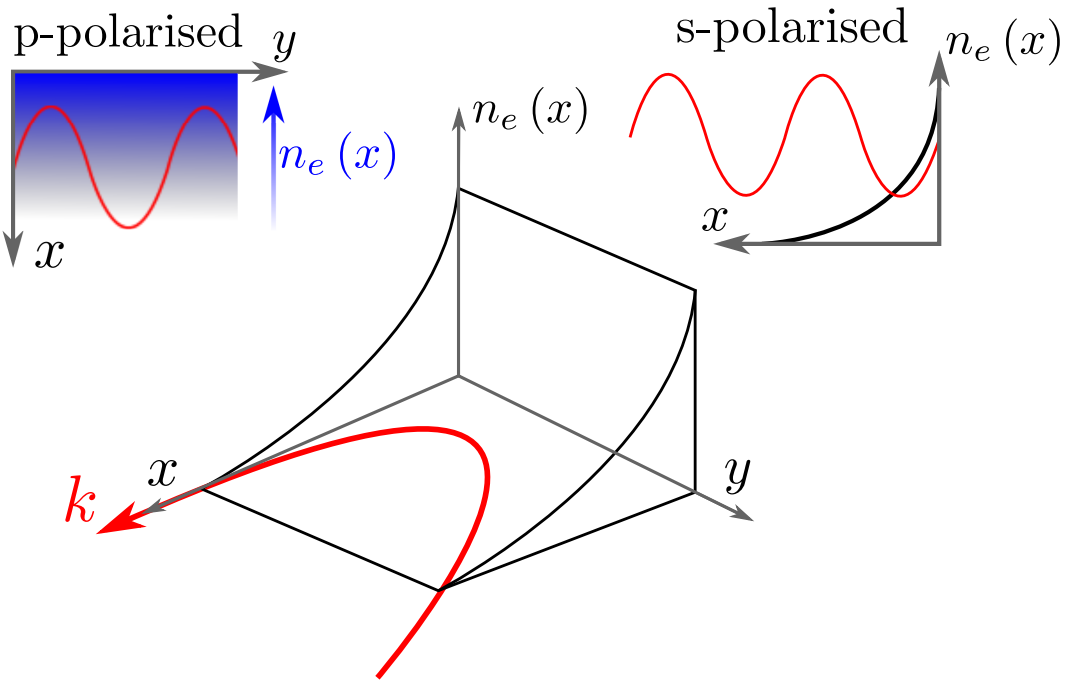

Figure 1.8: An EM wave propagates obliquely into a density ramp, its direction of propagation indicated by wave vector $\mathbf{k}$. When the wave is *s-polarised* then the electric field always points in a direction for which the plasma density is constant. However when the wave is *p-polarised*, the electric field has a component in the direction of the density gradient.

velocities and the result is a flattening of the distribution near the phase velocity of the electrostatic wave; this is illustrated in Fig. 1.7.

We now know some of the key waves that propagate in a plasma and means by which the electrostatic waves can transfer energy to the plasma. Now we briefly discuss some ways in which the electromagnetic wave couples into the electron motion to seed the electrostatic waves. Resonant absorption is one such mechanism, and is a consequence of electric field polarisation with respect to a plasma density ramp rising to critical (Fig. 1.6) and as such is of particular relevance to ICF. When the electric field vector is in the direction of the density gradient or *p-polarised* as shown in Fig. 1.8, we have that the component $\nabla\left(\nabla\cdot\tilde{\mathbf{E}}\right)\neq 0$. From our formulation of the electron plasma wave in Eq. (1.15) we can see how this can excite the electrostatic wave.

The point of strongest absorption is at the critical surface where the EM wave is resonant with the EP wave ($\omega_{\mathsf{EM}}=\omega pe$), and Kruer shows that the absorbed energy

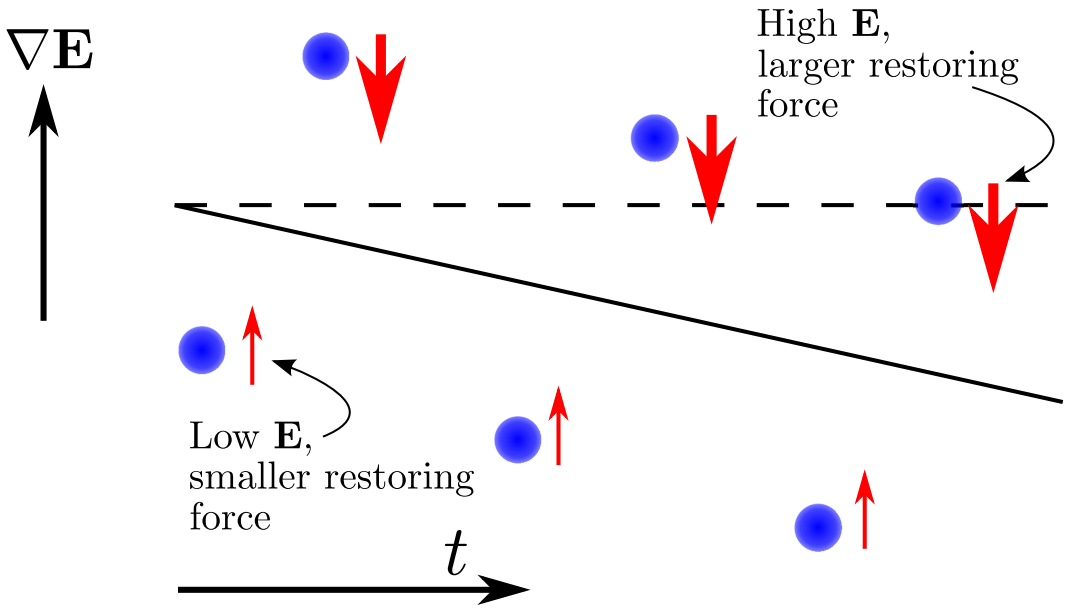

Figure 1.9: Illustration of the effect of ponderomotive force. A charge (blue) is accelerated through the region of higher $\mathbf{E}$ into the area of low $\mathbf{E}$ where the restoring force (red arrow) is lower. The charge is accelerated faster in the high $\mathbf{E}$ region than it is decelerated in the low $\mathbf{E}$ region. This moves the centre of oscillation (solid black) away from the original position (dashed black).

flux for resonant absorption is $\epsilon_{\text{abs}} \approx {}^{\omega L E_d^2}/_8$ [26] where L is the linear length of the density ramp, and E_d is the component of the electric field driving the electron oscillation along the density gradient. Kruer also shows that the strongest absorption is 0.5 at an oblique incident angle of the laser of $\theta_{\text{max}} \approx \arcsin\left[0.8\left({}^{c}/_{\omega L}\right)^{1/3}\right]$ [26]. It is important to note that the region over which resonant absorption occurs is very small and since the electric field strength varies along the density ramp the plasma experiences the *ponderomotive force* which serves to compress this resonant region. This results in high energy electrons near the shock in ICF which is detrimental to the early compression [8]. Motion due to ponderomotive force is best understood as the net movement of the centre point of oscillation for electrons in an EP wave as described in Fig. 1.9. This effect is readily derived for an electron in a non-uniform oscillating electric field in x, $E\left(x,t\right) = E\left(x\right)\sin\left(\omega t\right)$. For the simplest case in the absence of magnetic fields the Lorentz force gives that the motion of an electron in this field will be,

$$m_e \frac{du_e}{dt} = -eE\left(x\right)\sin\left(\omega t\right) \tag{1.25}$$

Now model the motion of the electrons with a net drift velocity u_{0e} that varies slowly and the fast oscillations $\tilde{u}_e$ such that the particle position can be divided into the centre of oscillation x_{0e} and the small perturbation $\tilde{x}_e$ due to oscillation. This allows us to Taylor expand $E(x)$,

$$\begin{aligned} m_e \frac{d}{dt}\left(u_{0e}+\tilde{u}_e\right) &= e\left[E\left(x_{0e}\right)+\left(x-x_{0e}\right)\frac{dE\left(x_{0e}\right)}{dx}+\ldots\right]\sin\left(\omega t\right) \\ &\approx e\left[E\left(x_{0e}\right)+\tilde{x}_e\frac{dE\left(x_{0e}\right)}{dx}\right]\sin\left(\omega t\right) \end{aligned} \tag{1.26}$$

We have defined u_{0e} to refer to the slowly varying drift, and assumed $\tilde{x}_e$ is small. Therefore we take x_{0e} to be a constant over the small oscillations and $E \gg \tilde{x}_e{}^{dE}/_{dx}$,

$$\begin{aligned} m_e\frac{d\tilde{u}_e}{dt} = eE\left(x_{0e}\right)\sin\left(\omega t\right) &\Rightarrow \tilde{x}_e = -\frac{e}{m_e\omega^2}E\left(x_{0e}\right)\sin\left(\omega t\right) \\ \Rightarrow m_e\frac{du_{0e}}{dt} &= -\frac{e^2}{m_e\omega^2}E\left(x_{0e}\right)\frac{dE\left(x_{0e}\right)}{dx}\sin^2\left(\omega t\right) \end{aligned} \tag{1.27}$$

We now time average over the a single period in the electric field oscillation to find the force associated with the change in drift velocity,

$$\begin{aligned} m_e\left\langle\frac{du_e}{dt}\right\rangle = \frac{m_e\omega}{2\pi}\int_0^{\frac{2\pi}{\omega}} -\frac{e^2}{m_e\omega^2}E\left(x_{0e}\right)\frac{dE\left(x_{0e}\right)}{dx}\sin^2\left(\omega t\right)dt \\ \Rightarrow F_{\text{drift}} = -\frac{e^2}{4m_e\omega^2}\frac{d}{dx}E^2\left(x\right) \end{aligned} \tag{1.28}$$

This force is the ponderomotive force, which Kruer gives for a plasma in 3-dimensions as [26],

$$\mathbf{F}_p = -\frac{e^2}{4m_e\omega^2}\nabla\mathbf{E}^2 \tag{1.29}$$

1.2.1 Parametric Instabilities

Parametric instabilities are a set of mechanisms by which laser energy is absorbed by the plasma but differs from resonant absorption in that they tend to drive unstable growth of multiple plasma waves at various frequencies. The name comes from parametric oscillators, a form of damped harmonic oscillation in which the parameters (e.g. damping, frequency, forcing) can vary in time. For plasma waves given by oscillators x_1 and x_2 and a laser input *pump* E we can model a 1D parametric instability by use of the general form of a parametric oscillator and a force term $F(t) \propto x_2 E$ for x_1 and $\propto x_1 E$ for x_2 to represent the coupling between the three waves. For constants C representing the strength of this coupling and γ the damping coefficient [30],

$$\frac{d^2 x_1}{dt^2} + \gamma_1 \frac{dx_1}{dt} + \omega_1^2 x_1 = C_1 x_2 E \tag{1.30}$$

$$\frac{d^2 x_2}{dt^2} + \gamma_2 \frac{dx_2}{dt} + \omega_2^2 x_2 = C_2 x_1 E \tag{1.31}$$

Where damping and forcing is neglected the terms ω_1 and ω_2 are the frequency for the simple harmonic motion of x_1 and x_2 respectively. If we take a general form for the laser pump as $E = E_0 \cos(\omega_0 t)$ we can find the frequencies at which this coupling can occur through Fourier transform of Eq. (1.30) and Eq. (1.31). We use the notation $\hat{x}(\omega) = {}^1/_{2\pi} \int x(t) \exp(i\omega t)\, dt$ and that for linear equations under Fourier transform ${}^d/_{dt} \to i\omega$,

$$\begin{aligned}
\left(\omega_1 + i\gamma_1\omega - \omega^2\right) \hat{x}_1(\omega) &= \frac{C_1 E_0}{2\pi} \int x_2 \cos(\omega_0 t) \exp(i\omega t)\, dt \\
&= \frac{C_1 E_0}{4\pi} \left(\int x_2 \exp\left[i(\omega + \omega_0)t\right] dt + \int x_2 \exp\left[i(\omega - \omega_0)t\right] dt \right) \\
&= \frac{C_1 E_0}{2} \left[\hat{x}_2(\omega + \omega_0) + \hat{x}_2(\omega - \omega_0)\right]
\end{aligned} \tag{1.32}$$

From this we can see that $\hat{x}_1(\omega)$ is coupled to oscillations $\hat{x}_2(\omega \pm \omega_0)$ through the pumping laser. We can use Eq. (1.31) to find relations for the frequency modes

$\omega + \omega_0$ and $\omega - \omega_0$ in x_2. For the latter we multiply Eq. (1.31) through by $\exp(i\omega_0 t)$ prior to Fourier transform to produce the frequency shift,

$$\left(\omega_2 + i\gamma_2(\omega + \omega_0) - (\omega + \omega_0)^2\right)\hat{x}_2(\omega + \omega_0) = \frac{C_2 E_0}{2\pi}\int x_1 \cos(\omega_0 t)\exp(i\omega t)\exp(i\omega_0 t)\,dt$$
$$= \frac{C_2 E_0}{2\pi}\left(\int x_1 \exp[i\omega_0 t]\exp[i(\omega + \omega_0)t]\,dt + \int x_1 \exp[-i\omega_0 t]\exp[i(\omega + \omega_0)t]\,dt\right)$$
$$= \frac{C_2 E_0}{2}\left[\hat{x}_1(\omega + 2\omega_0) + \hat{x}_1(\omega)\right]$$
$$\text{Similarly, } \left(\omega_2 + i\gamma_2(\omega - \omega_0) - (\omega - \omega_0)^2\right)\hat{x}_2(\omega - \omega_0) = \frac{C_2 E_0}{2}\left[\hat{x}_1(\omega) + \hat{x}_1(\omega - 2\omega_0)\right] \tag{1.33}$$

Now it can be seen that the oscillation $\hat{x}_2(\omega - \omega_0)$ feeds back to the oscillation $\hat{x}_2(\omega)$. We can find a similar relation for $\hat{x}_2(\omega + \omega_0)$ by multiplying Eq. (1.31) through by $\exp(-i\omega_0 t)$. We explore the case where damping and non-resonant terms $\hat{x}_1(\omega \pm 2\omega_0)$ are negligible such that the system of equations can be written,

$$\begin{pmatrix} \omega^2 - \omega_1^2 & \frac{C_1 E_0}{2} & \frac{C_1 E_0}{2} \\ \frac{C_2 E_0}{2} & (\omega - \omega_0)^2 - \omega_2^2 & 0 \\ \frac{C_2 E_0}{2} & 0 & (\omega + \omega_0)^2 - \omega_2^2 \end{pmatrix}\begin{pmatrix} \hat{x}_1(\omega) \\ \hat{x}_2(\omega - \omega_0) \\ \hat{x}_2(\omega + \omega_0) \end{pmatrix} = 0 \tag{1.34}$$

For a non-trivial solution of Eq. (1.34) the determinant must be zero. When oscillator $\hat{x}_1$ grows slowly we have that $\omega \approx \omega_1$ in which case $\omega_0^2 = (\omega_2 - \omega_1)(\omega_1 + \omega_2)$ for zero determinant. The $(\omega_2 - \omega_1)$ comes from the $\hat{x}_2(\omega_1 - \omega_0)$ term whilst $(\omega_2 + \omega_1)$ comes from the $\hat{x}_2(\omega_1 + \omega_0)$. The parametric instabilities explored here involve the laser decaying into two of the three plasma waves derived in Eq. (1.18), Eq. (1.21) and Eq. (1.24). Therefore higher frequency pump ω_0 decays into lower frequency plasma waves ω_1 and ω_2; this allows us to neglect the $\hat{x}_2(\omega_1 + \omega_0)$ term as non-resonant, in which case we find the frequencies at which this feedback occurs as,

$$\omega_0 = \omega_1 + \omega_2 \tag{1.35}$$

This is called the *frequency matching condition* and a similar equation can be found for the wavevector, which together describe the energy and momentum conservation for the decay [30],

$$\mathbf{k}_0 = \mathbf{k}_1 + \mathbf{k}_2 \tag{1.36}$$

There are four types of decays from the incident laser into the three plasma waves derived in this section [8]. These are given below where EM is an electromagnetic wave, IA is an ion-acoustic wave, and EP is an electron plasma wave. Not all of these decays can occur in 1D, but for those that can we can plot the dispersion relations for the three plasma waves together for useful visual method to determine where these frequency matching conditions will be met; this is demonstrated in Fig. 1.10.

- Plasma decay instability, EM $\rightarrow$ IA+EP
- Two-plasmon decay instability, EM $\rightarrow$ EP+EP
- Stimulated Brillouin scattering, EM $\rightarrow$ EM+IA
- Stimulated Raman scattering, EM $\rightarrow$ EM+EP

As shown in the derivation of Eq. (1.34), these mechanisms are unstable because the three-way coupling of waves instigates a feedback effect. In the case of stimulated Raman scattering if there is a density gradient in the direction of laser propagation then an EP wave will be initiated by the laser field. The electron motion in the presence of an electric field gives rise to a current density, and this is associated with a scattered EM wave. This new EM wave interferes with the incident laser field which can cause a gradient in the electric field. As we have seen derived in Eq. (1.28), this gradient gives rise to a ponderomotive force which can serve to drive the electron plasma wave. Under proper frequency and wavenumber matching conditions this feedback mechanism can undergo unstable growth.

The strongest mode of SRS is where the new EM wave is backscattered [26]; that is to say it propagates backwards along the propagation of the incident laser. In the context of ICF, SRS backscatter tends to cause the head of the laser to break up into filaments, which serves to reduce the energy reaching the core of the target [31];

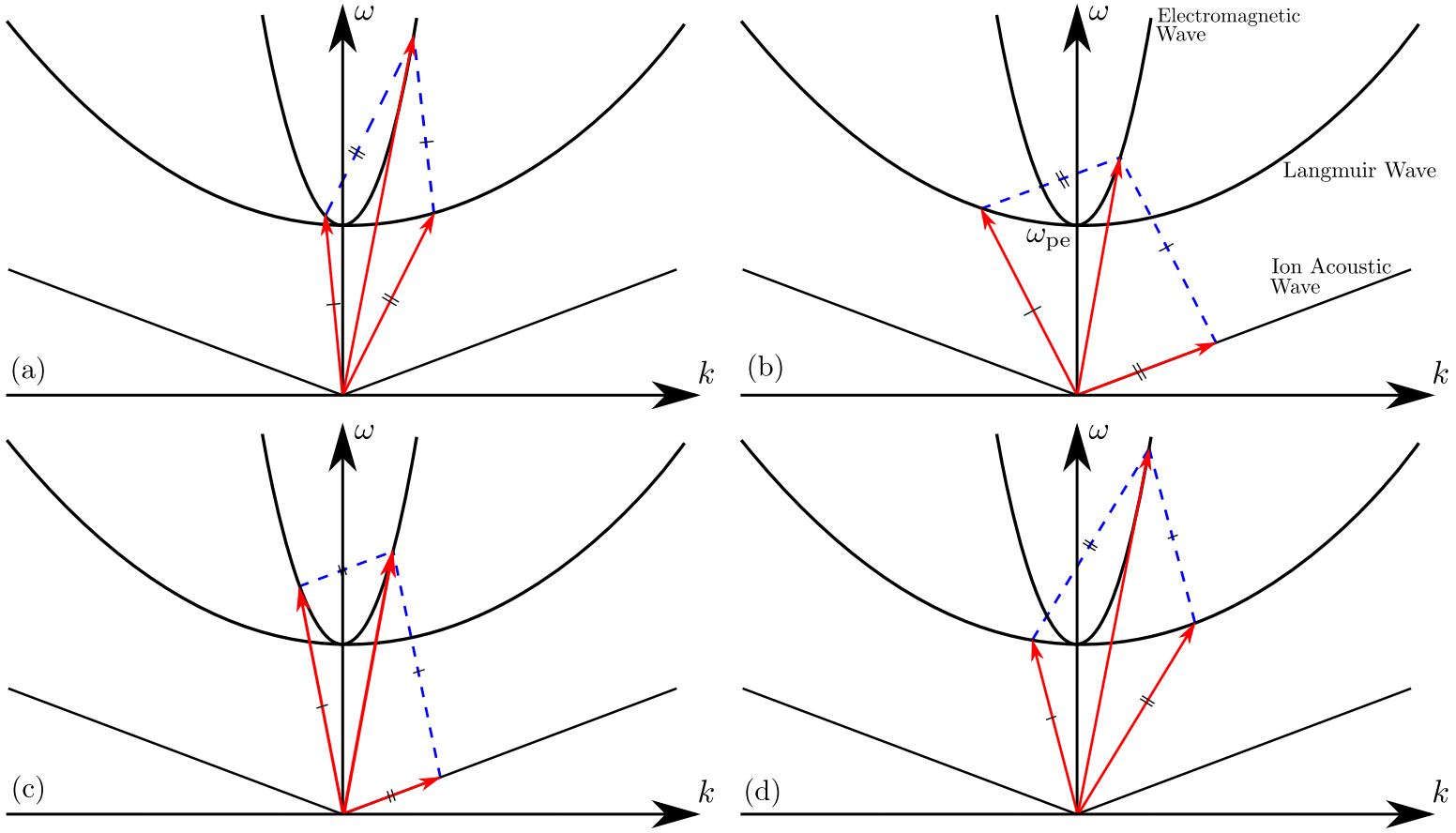

Figure 1.10: Sketch of the three important plasma waves arising from analysis of the two-fluid model. By drawing a parallelogram such that all the corners touch one of the three dispersion curves it is possible to find frequencies at which one of the four parametric instabilities will occur. Shown are (a) stimulated Raman scattering, (b) parametric decay instability, (c) stimulated Brillouin scattering and (d) two-plasmon decay instability.

this is explored in greater detail in Chapter 4. In other directions, random scattering of light also has negative effects upon the symmetry in all ICF scheme; as much as 25% of the laser energy has been observed to be scattered this way [18]. In general all of the parametric instabilities presented here are found to be detrimental to the ICF scheme [8]. As shown in Fig. 1.6 the instabilities occur at different points in the density ramp; this is dictated by the frequency matching conditions. In the case of SRS, we know that the EP wave occurs at the plasma frequency, and for the scattered EM wave to exist in the plasma we require that $\omega_{\mathsf{EM}} > \omega_{pe}$. From the matching conditions,

$$\omega_0 \approx \omega_{\mathsf{EM}} + \omega_{EP} \Rightarrow \omega_0 \gtrsim 2\omega_{pe} \Rightarrow n_{SRS} \lesssim \frac{n_c}{4} \tag{1.37}$$

The strongest point of Raman-scattering is seen at $n_c/4$; the EP wave can be observed by an increase of hot electrons and in hohlraum experiments it was found that 50% of incident light energy could be driven into these hot electrons [18]. It should be noted that the simple analysis used in Eq. (1.34) excludes damping, but any EP and IA waves could be damped to the point that the instability is effectively switched off. By including damping we can find the threshold intensity that the incident laser must exceed for the instabilities to be present. This also allows us to calculate the growth rate of the instabilities, and it is found that that all of the parametric instabilities presented here exhibit a $\gamma \sim \sqrt{I\lambda^2}$ scaling [8, 26, 30]. Stimulated Brillouin scattering (SBS) couples the incident laser field into both an EM and IA wave and is analogous to SRS for lower frequency IA waves. Since in general $\omega_{\mathsf{IA}} \ll \omega_{\mathsf{EM}}$ the frequency matching condition gives,

$$\omega_0 \approx \omega_{\mathsf{EM}} \gtrsim \omega_{pe} \Rightarrow n_{SBS} \lesssim n_c \tag{1.38}$$

Since SBS can occur right up to the critical surface, the ion acoustic waves will have the effect of pulling ions out of the fusion fuel in an ICF context [8]. However the ion acoustic wave tends to be strongly damped unless $T_e \gg T_{\mathsf{i}}$ [26] and so the threshold intensity for the instability tends to be relatively high. The plasma decay instability (PDI) begins similarly to SBS; the incident laser field interacts with an ion

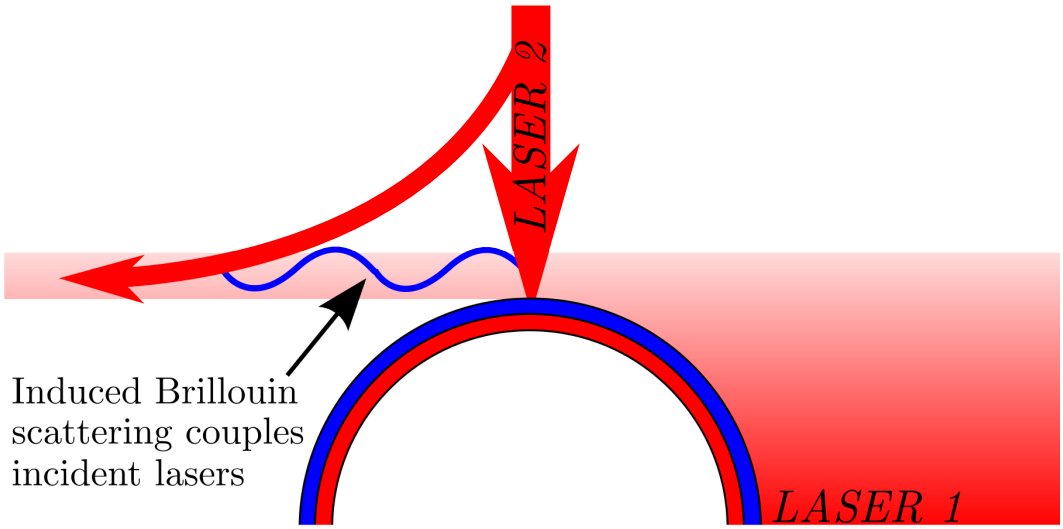

Figure 1.11: The fringe of the transverse intensity profile of a laser spot misses the ICF deuterium tritium target and crosses the path of a second incident laser. Energy from the second beam couples to the fringe of the first via an ion acoustic wave (induced Brillouin scattering) resulting in energy being channelled into the fringe and away from the target [23].

density fluctuation but instead this drives an EP wave. As with SRS the electric field across a density gradient results in a ponderomotive force which may be enhanced by the EP wave. In the case that the ion density fluctuation is caused by an IA wave we can see how the feedback mechanism between the three waves builds up at the correct frequencies. As with SBS we also note that $\omega_{\mathsf{IA}} \ll \omega_{\mathsf{EP}}$ therefore $\omega_0 \approx \omega_{EP}$ from the frequency matching condition and therefore this instability occurs only at the critical surface. This time we expect that the decay will not only extract fuel from a laser fusion target but also potentially drive hot electrons into the fuel via the electron plasma wave thereby damaging compression.

SBS is also the cause of one of the more useful consequences of parametric instability, namely crossed-beam energy transfer [22, 24, 25]. As the name implies this occurs when two incident laser beams cross within a plasma, a situation seen in the hohlraum for indirect drive ICF. Understanding that SBS couples the incident laser to a scattered EM and IA wave we can consider crossed-beam energy transfer as being a special case of SBS where the scattered EM wave is another incident laser; this is *induced* Brillouin scattering [22]. Since frequency matching conditions must be met the

two beams must differ in frequency; an IA wave couples these crossed-beams together and in much the same way that energy can be transferred from an incident laser into a scattered EM wave, energy can be transferred between the two beams. This can be detrimental to the indirect drive scheme as it can cause asymmetry in the illumination of the hohlraum, however it can also be harnessed to aid symmetry through tuning of the frequencies to either increase or decrease this energy transfer [24]. Crossed-beam energy transfer is also relevant to direct drive schemes; when multiple beams shine on the target, if a beam is wide enough for the fringes to miss the target but cut across another beam then energy can be coupled out of the beam hitting the target and into the beam missing the target resulting in energy loss as illustrated in Fig. 1.11 [23].

The two-plasmon (EP wave) decay instability (TPDI) also occurs due to electron density fluctuation as with SRS. However instead of decaying into an EM wave associated with the current density from the EP wave crossing the electron density gradient, two EP waves are seeded in such a way that the current densities from each wave cancel. In effect there is no net current density and so no new EM wave is produced, but two separate EP waves are driven. As with SRS frequency matching conditions indicate that $\omega_0 \approx 2\omega_{pe}$ therefore TPDI only occurs when $n \approx {}^{n_{\rm cr}}/_4$ and the tendency is for TPDI to cause bursts of hot electrons.

TPDI is a good example of how parametric instabilities also interact with each other as well as the laser; if there are other sources of EP waves then TPDI may couple them to the laser, producing more EP waves and more potential couplings such that a cascade of TPDI can occur. The hot electrons produced from EP wave damping at the quarter critical surface is extremely destructive to direct drive ICF schemes. There are many other unexpected combinations of parametric instabilities, and actually predicting what effect these may have in experiment can be particularly difficult. For instance, one might expect that SBS would cause intense reflection at the critical surface preventing energy absorption close to the fusion fuel, however it is found that SBS only occurs very briefly [32] and therefore has almost no impact on compression or heating. Both SRS and SBS switch-on and off rapidly due to the product waves growing to reach threshold intensities for any other instability, and so analysing any linear instability in isolation is of limited usefulness. Exploring the net effect parametric instabilities in general requires

experiment or numerical analysis; direct numerical solution of the Vlasov equation have been shown to provide a detailed view of the distribution functions allowing for modelling the parametric instabilities without noise even with a low particle count [33]. This is even computationally undemanding in 1D but is expensive in 2D due to requiring 2D space and 2D velocity resulting in a 4D computational grid, it also requires manual initial perturbation to produce useful results. For larger simulations particle-in-cell simulations also excel at reproducing parametric instabilities with significantly reduced computational cost at the expense of increased noise [9].

1.2.2 Ionisation in the Field of an Intense Laser

Although plasmas are ionised material, the process of ionisation is not typically a primary consideration in plasma phenomena. This is often justified, as the process of ionisation is often on a smaller timescale than is relevant to plasma waves and instabilities which are the focus of many plasma studies. However there are some cases where ionisation is key, for instance when the distribution of electrons produced by ionisation is important and cannot be assumed or the timescales are small such as those relevant to femtosecond laser pulses. The process by which neutral material transitions to the plasma state can therefore be an integral part of laser-plasma interactions, and also challenging to model correctly.

The mechanism of ionisation in the laser field differs depending on the temperature, density and level of ionisation within the plasma and also the intensity of the incident laser field. We might initially describe the ionisation process as photons absorbed by a bound electron within an atom via the photoelectric effect. However if the electric field is strong enough we can expect the energy levels within the atom to be shifted via the Stark effect [34] which would affect the photon energy required for ionisation. The difficulty in modelling this is increased when considering that the field is time-varying. In addition to this it is initially unclear how the photoelectric effect applies when considering the energy of a photon in a typical laser; the National Ignition Facility operates their laser at $\sim 0.35\mu$m with polymer targets and achieve full ionisation [18]. The first ionisation level of carbon has a binding energy of 11.26eV, but a single photon of a 0.35μm laser has energy $E = \hbar\omega = 3.55$eV. Finally, when the neutral material has

undergone ionisation, the electrons added to the system may cause further ionisation through Coulomb collision with bound electrons. This simple qualitative analysis suggests the process by which neutral material becomes plasma to be a highly complex and non-linear process.

The mechanisms by which the electromagnetic field directly causes ionisation are described as *field* ionisation. In 1965, Keldysh derived formulae describing field ionisation for a hydrogen atom in the low frequency regime where photon energy is beneath the binding energy or *ionisation energy* of the electron [35]. Under Keldysh theory the ionisation rate of direct transition from ground state to a free state is given by,

$$W = \sqrt{\frac{2\epsilon}{\hbar}}\omega \left(\frac{\gamma}{\sqrt{1+\gamma^2}} \right)^{3/2} S\left(\gamma, \frac{\tilde{\epsilon}}{\hbar\omega}\right) \exp\left(-\frac{2\tilde{\epsilon}}{\hbar\omega} \left[\sinh^{-1}\gamma - \gamma \frac{\sqrt{1+\gamma^2}}{1+2\gamma^2} \right] \right)$$

For

$$S\left(\gamma, x\right) = \sum_{n=0}^{\infty} \exp\left(-2\left[\lfloor x+1 \rfloor - x + n\right] \left[\sinh^{-1}\gamma - \frac{\gamma}{\sqrt{1+\gamma^2}} \right] \right) \times \Phi\left(\sqrt{\frac{2\gamma}{\sqrt{1+\gamma^2}} \left[\lfloor x+1 \rfloor - x + n\right]} \right)$$

And

$$\Phi\left(z\right) = \int_0 \exp\left(y^2 - z^2\right) dy$$

(1.39)

Where ϵ is the ionisation energy, ω is the electric field frequency and $\tilde{\epsilon} = \epsilon\left(1 + \gamma^2/2\right)$ is the effective ionisation potential where $\gamma = \omega\sqrt{2m_e\epsilon}/eE$ is the Keldysh adiabaticity parameter [36]. In Eq. (1.39) x is a dummy variable whilst $\lfloor x \rfloor$ is used to indicate the integer part of x (e.g. $\lfloor 1.5 \rfloor = 1$) and within the Keldysh parameter we have that m_e is the electron mass, e is the electron charge and E is the electric field strength. All of the equations provided in this section are given in Hartree atomic units.

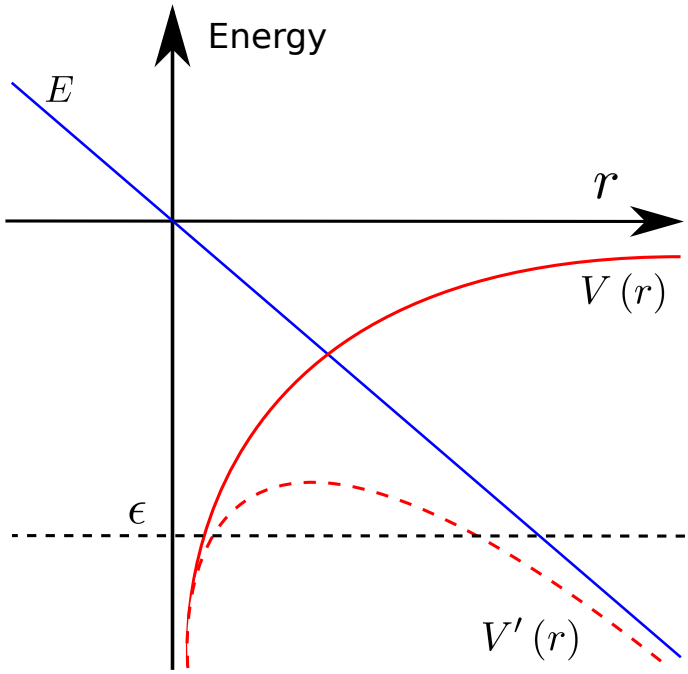

Figure 1.12: Laser field E deforming the Coulomb potential $V(r)$ of a hydrogen atom, forming a barrier $V'(r)$ through which the bound electron with ionisation energy ϵ can tunnel in the classical approximation.

Probably the most important aspect of the work presented in [35] is the Keldysh parameter γ as it demonstrates field ionisation to consist of two distinct regimes. When $\gamma \ll 1$ Keldysh shows that $S\left(\gamma, \tilde{\epsilon}/\hbar\omega\right) \approx \sqrt{3\pi}/4\gamma^2$ [35] and the ionisation probability becomes,

$$W = \frac{\sqrt{6\pi}\epsilon}{4\hbar}\left(\frac{eE\hbar}{m_e^{1/2}I_0^{3/2}}\right)^{1/2}\exp\left(-\frac{4\sqrt{2m_e}I_0^{3/2}}{3e\hbar E}\left[1-\frac{m_e\omega^2\epsilon}{5e^2E^2}\right]\right) \tag{1.40}$$

Since $\gamma \ll 1$ we have that $m_e\omega^2\epsilon \ll 5e^2E^2$ therefore the term in ω can be neglected, in which case we find $W \sim \exp\left(-1/E\right)$ which scales as the rate for ionisation by quantum tunnelling [37]. Tunnelling ionisation considers the deformation of the atomic Coulomb potential by the imposed electric field. To understand this it is helpful to model the situation classically. If we consider hydrogen with a $1/r$ atomic potential then it is not immediately obvious how tunnelling is relevant as the potential does not have a barrier of finite width through which the electron can tunnel. However every half-

cycle of the laser the imposed electric field can deform the original $1/r$ atomic potential such that a suitable barrier is formed. Providing the cycle is long enough the electron can tunnel free as illustrated in Fig. 1.12. When $\gamma \gg 1$ Eq. (1.39) reduces to,

$$\begin{aligned} W =& \sqrt{\frac{2\epsilon}{\hbar}}\omega \exp\left(-\frac{2\tilde{\epsilon}}{\hbar\omega}\left[\ln(2\gamma) - \frac{1}{2}\right]\right) \sum_{n=0}^{\infty} \Phi\left(\sqrt{2\lfloor \frac{\tilde{\epsilon}}{\hbar\omega} + 1\rfloor - \frac{2\tilde{\epsilon}}{\hbar\omega} + 2n}\right) \\ & \times \exp\left(-2\left[\lfloor \frac{\tilde{\epsilon}}{\hbar\omega} + 1\rfloor - \frac{\tilde{\epsilon}}{\hbar\omega} + n\right]\left[\ln(2\gamma) - 1\right]\right) \end{aligned} \tag{1.41}$$

Both terms in $S(\gamma, x)$ tend to zero as $n \to \infty$ and the maximum is found at $n = 0$ [35], so neglecting other terms we find that,

$$W = \sqrt{\frac{2\epsilon}{\hbar}}\omega \left(\frac{e^2E^2}{8m_e\omega^2\epsilon}\right)^{\lfloor \frac{\tilde{\epsilon}}{\hbar\omega}+1\rfloor} \exp\left(2\lfloor \frac{\tilde{\epsilon}}{\hbar\omega} + 1\rfloor - \frac{\tilde{\epsilon}}{\hbar\omega}\right) \Phi\left(\sqrt{2\lfloor \frac{\tilde{\epsilon}}{\hbar\omega} + 1\rfloor - \frac{2\tilde{\epsilon}}{\hbar\omega}}\right) \tag{1.42}$$

The scaling is now $W \sim E^{2\lfloor \tilde{\epsilon}/\hbar\omega+1\rfloor}$, where the term $\lfloor \tilde{\epsilon}/\hbar\omega + 1\rfloor$ is the minimum number of photons of energy $\hbar\omega$ required to ionise an electron with effective ionisation energy $\tilde{\epsilon}$. This scaling is in fact characteristic of *multiphoton* absorption [34]. This phenomena enables ionisation when $\hbar\omega < \tilde{\epsilon}$. The phrase *multiphoton* is slightly misleading in that it is not entirely accurate to say multiple photons are absorbed simultaneously. Multiphoton ionisation occurs when an electron absorbs a photon that does not have enough energy to cause ionisation or excitation to a higher energy state. Rather than immediately re-emitting the photon, the electron can exist in a virtual energy state. These energy states exist due to quantum uncertainty and the time that the electron can exist in this virtual state is given by $\Delta t \gtrsim \hbar/\Delta E$. If further photons are absorbed before the virtual state decays, then it is possible for the electron to have absorbed enough energy for ionisation.

The probability of absorption in Eq. (1.42) shows that there will be resonance effects when $\frac{\tilde{\epsilon}}{\hbar\omega} \approx \lfloor \frac{\tilde{\epsilon}}{\hbar\omega}+1\rfloor$ of the form shown in Fig. 1.13. The Keldysh parameter broadly separates the concepts of multiphoton and tunnelling ionisation as complimentary but competing effects and this notion has persisted into more recent research [34, 38, 39].

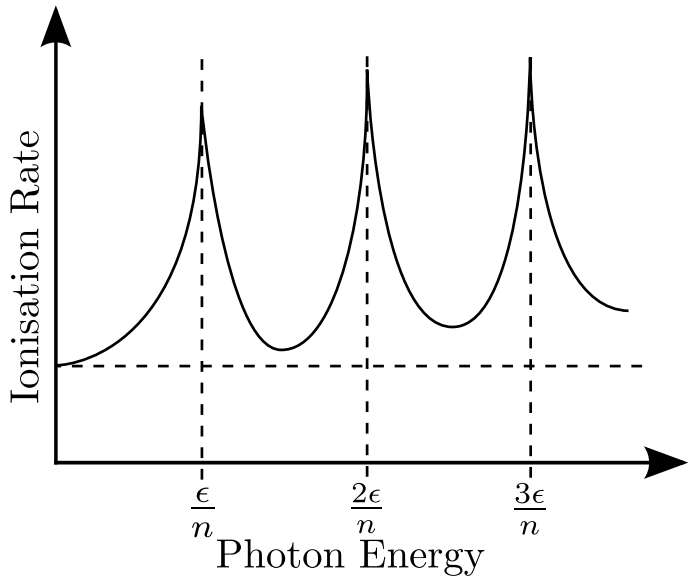

Figure 1.13: Sketch demonstrating multiphoton resonance effects for an electron with ionisation energy ϵ; for $n \in \mathbb{N}$ the above shows how the ionisation rate exhibits a sharp increase near regions where the ionisation energy is approximately equal the total energy of an integer number of the incident photons.

When looking at the peak intensities for lasers such as that used in NIF (10^{15}Wcm^{-2}) we can see that in general γ will be very low (0.05 for hydrogen) and will be within the tunnelling regime, but it is still important to consider both regimes. During the rise of the laser pulse intensity or in the fringes of the laser spot the intensity will drop off and for hydrogen we have that $\gamma > 1$ for $< 10^{12}$Wcm^{-2}. Alternatively the ionisation energy of the material may be high; in ionisation of C^{4+} we have that $\gamma > 1$ for $< 10^{14}$Wcm^{-2}. A helpful physical interpretation of the Keldysh parameter emerges as the comparison of the quiver energy of the electron to the energy of an incident photon when noting that the time-averaged quiver energy is $U_P = e^2E^2/4m_e\omega^2$ and using this to rewrite γ as [36],

$$\gamma = \sqrt{\frac{\epsilon}{2U_P}} \tag{1.43}$$

We expect both bound and free electrons to oscillate in the electric field and under a classical description of the bound state of the electron we can imagine that the lowering in the binding energy illustrated in Fig. 1.12 as being due to the electron oscillating away from the nucleus. When the oscillation becomes particularly large

the ionisation energy will vary greatly over a laser period. In the case where $U_P \gg \epsilon$ the multiphoton description of ionisation becomes inappropriate because the number of photons required for ionisation will vary greatly in time and it is unlikely resonance effects will be observed, as the duration over which the photons may be resonant with the electron binding energy will be relatively short. The quantum mechanical situation is clearly far more complicated but this simple classical interpretation provides a physical context for the importance of the Keldysh parameter which appears prominently throughout literature pertaining to ionisation in the field of an intense laser.

1.3 Particle-in-Cell Codes

PIC codes are a very intuitive method of plasma simulation where the basic scheme is to move the electrons and ions within a discrete spatial grid upon which are calculated electromagnetic fields that are *self-consistent* with the particle motion. These fields are used to calculate the force acting on the particles which determines their motion. This forms a simple cycle which is at the core of every PIC code; particle motion determines field which determines subsequent particle motion. Over a single time step this cycle can be neatly summarised by Fig. 1.14 [9]. It is important to note that whilst the fields are only known at points upon the grid, the particles move continuously throughout the domain. The fields are calculated using Maxwell's equations and for this the position and velocities of the particles must be translated into a charge and current density at the grid points. The particle motion is determined by the Lorentz force and with the fields calculated at the grid points there must also be a means for translating this back into forces acting upon the particles at their positions. The concept of weighting physical parameters such as electric field and charge back and to between particle and grid is discussed in §1.3.3.

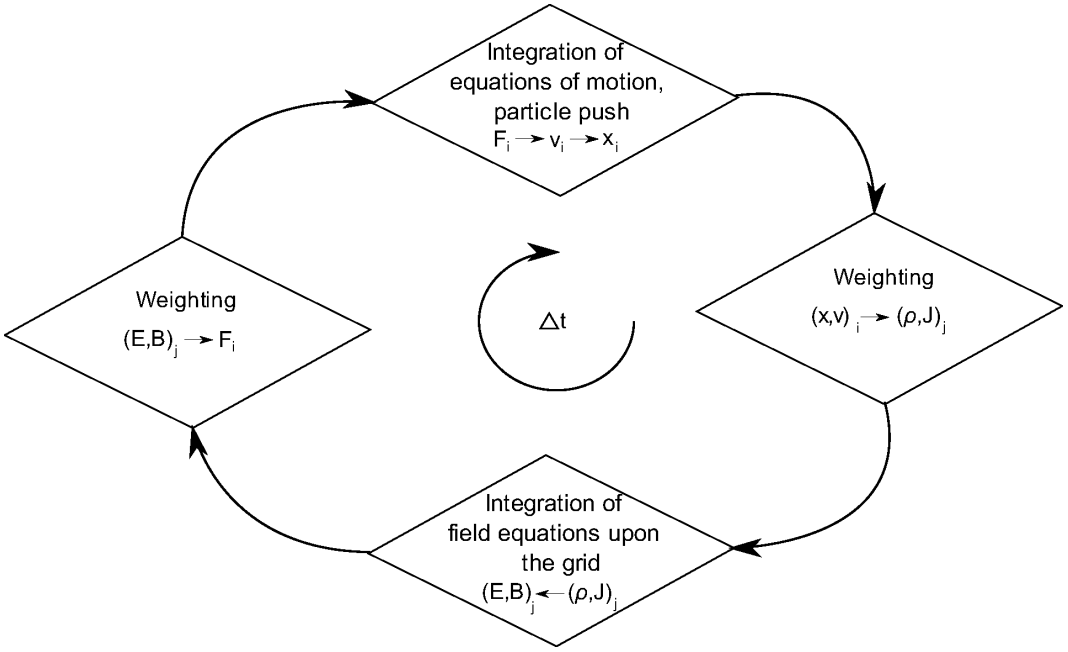

Figure 1.14: Generalised PIC code time-step cycle, particle indices i and grid indices j. [9]

The equations for the field updates and the particle motion are handled numerically using *finite differencing*, a simple but powerful method for solving continuous differential equations upon discretised spatial and temporal grids using a Taylor expansion. For the first differential of a function $f(x)$ on a discrete spatial grid in x with cell size Δx we could find the *central differencing* scheme as follows.

$$\begin{aligned} f(x+\Delta x) = f_{i+1} &= f_i + \Delta x \frac{df_i}{dx} + \frac{\Delta x^2}{2!}\frac{d^2 f_i}{dx^2} + \frac{\Delta x^3}{3!}\frac{d^3 f_i}{dx^3}\cdots \\ f(x-\Delta x) = f_{i-1} &= f_i + \Delta x \frac{df_i}{dx} + \frac{\Delta x^2}{2!}\frac{d^2 f_i}{dx^2} + \frac{\Delta x^3}{3!}\frac{d^3 f_i}{dx^3}\cdots \\ \Rightarrow \qquad \frac{df_i}{dx} &= \frac{f_{i+1} - f_{i-1}}{2\Delta x} - \frac{\Delta x^2}{3!}\frac{d^3 f_i}{dx^3} + \cdots \end{aligned} \tag{1.44}$$

Terms in Δx^2 and higher are neglected, therefore the error in this method scales as the grid spacing squared which means that the method is *second order*. The rest of this section shall concern itself with detailing the PIC steps laid out in Fig. 1.14 from the perspective of a 3D relativistic electromagnetic PIC code of the form described in

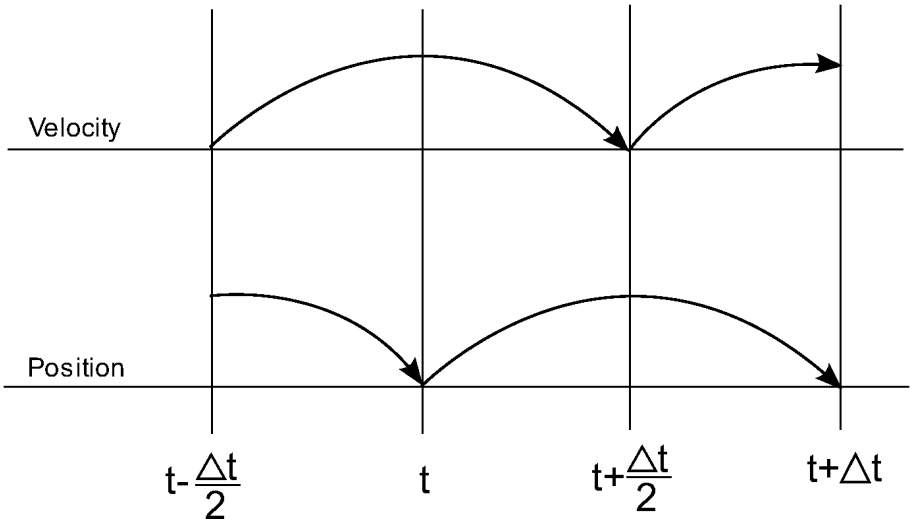

Figure 1.15: Leapfrog method, allowing for alternating updates of x and v via central differencing. [9]

Birdsall and Langdon's Plasma Physics via Computer Simulation [9] using second order central differencing schemes in the approximation of differential equations.

1.3.1 Particle Pusher

The basic particle pushing scheme integrates the equations of motion [9],

$$m\frac{d\mathbf{v}}{dt} = \mathbf{F} \qquad \frac{d\mathbf{x}}{dt} = \mathbf{v} \tag{1.45}$$

This is done via a finite differencing scheme called the *leapfrog* method [9] in which both position and velocity are calculated every Δt but out of step by $\Delta t/2$ as shown in Fig. 1.15. The equations to solve become,

$$m\frac{\mathbf{v}_{t+\frac{\Delta t}{2}} - \mathbf{v}_{t-\frac{\Delta t}{2}}}{\Delta t} = \mathbf{F}_t \qquad \frac{\mathbf{x}_{t+\Delta t} - \mathbf{x}_t}{\Delta t} = \mathbf{v}_{t+\frac{\Delta t}{2}} \tag{1.46}$$

Though it isn't immediately clear these are in fact second order central differencing schemes as laid out in Eq. (1.44) despite the lack of a factor 2 in the denominator. This is because the equation is time centred with timestep $\Delta t/2$. For the accelerating force we use the Lorentz force equation [9],

$$\mathbf{F} = m\frac{d\mathbf{v}}{dt} = q\left(\mathbf{E} + \mathbf{v} \times \mathbf{B}\right) \tag{1.47}$$

To be relativistic we require inclusion of $\gamma = \frac{1}{\sqrt{1-\left(\frac{v}{c}\right)^2}}$. However high velocities may cause this to tend quickly to maximum size in computer memory when variables of type double are used in numerical simulation. To prevent such an overflow error, we instead define $\mathbf{u} = \gamma\mathbf{v}$ such that $m\mathbf{v} = m_0\mathbf{u}$ and $\gamma = \sqrt{1 + \frac{u^2}{c^2}}$ which will be a comfortably bounded value in memory [9]. Now we use $\mathbf{u}$ instead of $\mathbf{v}$ to obtain,

$$\frac{d\mathbf{u}}{dt} = \frac{q}{m_0}\left(\mathbf{E} + \frac{\mathbf{u}}{\gamma} \times \mathbf{B}\right) \tag{1.48}$$

For a central difference scheme to solve the above, we centre the magnetic term by averaging $v_{t+\frac{\Delta}{2}}$ and $v_{t-\frac{\Delta}{2}}$ [40],

$$\frac{\mathbf{u}_{t+\frac{\Delta t}{2}} - \mathbf{u}_{t-\frac{\Delta t}{2}}}{\Delta t} = \frac{q}{m_0}\left(\mathbf{E}_t + \frac{\mathbf{u}_{t+\frac{\Delta t}{2}} + \mathbf{u}_{t-\frac{\Delta t}{2}}}{2\gamma_t} \times \mathbf{B}_t\right) \tag{1.49}$$

Though this can be solved directly it is easier to decompose the particle push into three steps through use of *Boris rotation* [41]. This scheme separates electric and magnetic forces via the substitution [9],

$$\begin{aligned} \mathbf{u}_{t-\frac{\Delta t}{2}} =& \mathbf{u}^- - \frac{q\mathbf{E}_t\Delta t}{2m_0} \qquad \mathbf{u}_{t+\frac{\Delta t}{2}} = \mathbf{u}^+ + \frac{q\mathbf{E}_t\Delta t}{2m_0} \\ \Rightarrow& \frac{\mathbf{u}^+ - \mathbf{u}^-}{\Delta t} = \frac{q}{2\gamma_t m}\left(\mathbf{u}^+ + \mathbf{u}^-\right) \times \mathbf{B}_t \end{aligned} \tag{1.50}$$

If we dot product Eq. (1.50) with $(\mathbf{u}^+ + \mathbf{u}^-)$ we find $|\mathbf{u}^+| = |\mathbf{u}^-|$ which implies that the magnitude of the vector is unaffected by the above operation, therefore there is no change in energy. As such this must be the rotating action of the magnetic field

[9]. If we let $\alpha = \frac{q\Delta t}{2\gamma_t m}\mathbf{B}_t$ and consider the components of Eq. (1.50),

$$
\begin{aligned}
u_x^+ - u_x^- &= \alpha_z\left(u_y^+ + u_y^-\right) - \alpha_y\left(u_z^+ + u_z^-\right) \\
u_y^+ - u_y^- &= \alpha_x\left(u_z^+ + u_z^-\right) - \alpha_z\left(u_x^+ + u_x^-\right) \\
u_z^+ - u_z^- &= \alpha_y\left(u_x^+ + u_x^-\right) - \alpha_x\left(u_y^+ + u_y^-\right)
\end{aligned}
$$

$$
\begin{bmatrix} 1 & -\alpha_z & \alpha_y \\ \alpha_z & 1 & -\alpha_x \\ -\alpha_y & \alpha_x & 1 \end{bmatrix}
\begin{pmatrix} u_x^+ \\ u_y^+ \\ u_z^+ \end{pmatrix} =
\begin{bmatrix} 0 & \alpha_z & -\alpha_y \\ -\alpha_z & 0 & \alpha_x \\ \alpha_y & -\alpha_x & 0 \end{bmatrix}
\begin{pmatrix} u_x^- \\ u_y^- \\ u_z^- \end{pmatrix} \tag{1.51}
$$

$$
\Rightarrow \mathbf{u}^+ = \mathbf{A}\mathbf{u}^-
$$

$$
\text{where } \mathbf{A} = \frac{1}{1+\alpha_x^2+\alpha_y^2+\alpha_z^2}
\begin{bmatrix} -\alpha_z^2-\alpha_y^2 & \alpha_z+\alpha_y\alpha_x & \alpha_z\alpha_x-\alpha_y \\ \alpha_y\alpha_x-\alpha_z & -\alpha_x^2-\alpha_z^2 & \alpha_x+\alpha_z\alpha_y \\ \alpha_z\alpha_x+\alpha_y & \alpha_z\alpha_y-\alpha_x & -\alpha_x^2-\alpha_y^2 \end{bmatrix}
$$

From this we can now outline the three step Boris rotation scheme for getting from $\mathbf{u}_{t-\frac{\Delta t}{2}}$ to $\mathbf{u}_{t+\frac{\Delta t}{2}}$ as [9],

1. Half-step electric field acceleration $\mathbf{u}^- = \mathbf{u}_{t-\frac{\Delta t}{2}} + \frac{q}{2m}\mathbf{E}_t\Delta t$
2. Full magnetic field rotation $\mathbf{u}^+ = \mathbf{A}\mathbf{u}^-$
3. Second half-step electric field acceleration $\mathbf{u}_{t+\frac{\Delta t}{2}} = \mathbf{u}^+ + \frac{q}{2m}\mathbf{E}_t\Delta t$

For position update we simply solve $\frac{\mathbf{u}}{\gamma} = \frac{d\mathbf{x}}{dt}$ in much the same way as Eq. (1.45),

$$
\frac{\mathbf{x}_{t+\Delta t} - \mathbf{x}_t}{\Delta t} = \frac{\mathbf{u}_{t+\frac{\Delta t}{2}}}{\gamma_t} \tag{1.52}
$$

1.3.2 Field Solver

The PIC scheme solves the Maxwell's equations shown in Eq. (1.13) at discrete points upon the grid. Once again we make use of a second-order time-centred finite differencing scheme giving the equations to solve over the timesteps as,

$$\begin{aligned} \frac{\mathbf{B}_{t+\frac{\Delta t}{2}} - \mathbf{B}_{t-\frac{\Delta t}{2}}}{\Delta t} &= -\nabla \times \mathbf{E}_t \\ \frac{\mathbf{E}_{t+\Delta t} - \mathbf{E}_t}{\Delta t} &= \frac{1}{\epsilon_0 \mu_0} \nabla \times \mathbf{B}_{t+\frac{\Delta t}{2}} - \frac{1}{\epsilon_0} \mathbf{J}_{t+\frac{\Delta t}{2}} \end{aligned} \tag{1.53}$$

This scheme poses some problems, namely that we require $\mathbf{B}_t$ but only have $\mathbf{B}$ at half time-steps. We must also know how to find the current density. For the former we utilise a similar method to Boris rotation demonstrated in §1.3.1 where the update is divided into two steps,

1. Half magnetic field update $\mathbf{B}_t = \mathbf{B}_{t-\frac{\Delta t}{2}} - \frac{\Delta t}{2} \nabla \times \mathbf{E}_t$
2. Particle push described in §1.3.1
3. Second half magnetic field update $\mathbf{B}_{t+\frac{\Delta t}{2}} = \mathbf{B}_t - \frac{\Delta t}{2} \nabla \times \mathbf{E}_t$

The current density is found using the position and velocities of the particles moving continuously within the domain; this connects the particle motion component of a PIC code to the field updates and makes the fields calculated on the grid *self-consistent* with the charges in the domain. The current density is calculated directly from the definition $\mathbf{J} = nq\mathbf{v}$. For this, we take a summation of the particle velocities and charges weighted on the distance from the grid point as [9],

$$\mathbf{J}_{\mathrm{j},t+\frac{\Delta t}{2}} = \sum_{\mathrm{i}} q_{\mathrm{i}} \mathbf{v}_{\mathrm{i},t+\frac{\Delta t}{2}} \frac{S\left(\mathbf{X}_{\mathrm{j}} - \mathbf{x}_{\mathrm{i},t}\right) + S\left(\mathbf{X}_{\mathrm{j}} - \mathbf{x}_{\mathrm{i},t+\Delta t}\right)}{2} \tag{1.54}$$

Where $\mathbf{J}_{\mathrm{j},t+\frac{\Delta t}{2}}$ is the current density at grid point j, and therefore $\mathbf{X}_{\mathrm{j}}$ is the position of the grid point. The function S is a *weighting* function which in this case decides what fraction of current density a particle contributes based on its position. Weighting functions are further explained in §1.3.3. Surprisingly the $\mathbf{E}$ and $\mathbf{B}$ field

updates constitute a full handling of Maxwell's equations upon the grid even though only Ampère's and Faradays laws are used directly. This is because Gauss' law and the $\nabla \cdot \mathbf{B} = 0$ condition are implicitly handled at every time step by careful selection of initial conditions. Provided they are satisfied at $t = 0$ they are satisfied for all subsequent timesteps which can be shown by taking the dot product of Ampère's and Faradays laws [9],

$$\begin{aligned} &\text{From Faraday's law } \frac{\partial}{\partial t}\nabla \cdot \mathbf{B} = \nabla \cdot (\nabla \times \mathbf{E}) = 0 \\ &\text{and from Ampère's law,} \\ &\nabla \cdot (\nabla \times \mathbf{B}) = 0 = \mu_0 \nabla \cdot \mathbf{J} - \epsilon_0 \mu_0 \frac{\partial}{\partial t} \nabla \cdot \mathbf{E} \\ &\text{Gauss' law } \nabla \cdot \mathbf{E} = \frac{\rho}{\epsilon_0} \Rightarrow \frac{\partial \rho}{\partial t} + \nabla \cdot \mathbf{J} = 0 \end{aligned} \tag{1.55}$$

This last equation is a continuity equation which states that charge must be conserved throughout the simulation for Gauss' law to continue to be satisfied [9]. The PIC scheme is inherently charge conserving as the location of particles in the simulation is always known. However as it transpires the continuity equation is not satisfied in time as small discrepancies between $\mathbf{J}$ and ρ arise due to error introduced by the grid and weighting. More specifically, Eq. (1.54) has no means to cope with a charge leaving the cell and entering a neighbouring cell. Both situations result in a non-conservative $\nabla \cdot \mathbf{J}$ and the cumulative use of uncorrected current density produces an $\mathbf{E}$ that no longer satisfies Gauss' law. Whilst it is possible to solve a Poisson's equation on the grid to enforce a charge conservative value for $\mathbf{E}$ this is an implicit solve that in general involves inversion of a large matrix which is highly computationally expensive. The majority of PIC codes instead include an explicit current density correction each timestep to ensure the continuity equation is satisfied; this is discussed in more detail in Chapter 2.

1.3.3 Interpolating Between Grid and Particles

As previously mentioned the fields are localised to discrete grid points whereas particles travel continuously in the domain. When calculating the charge for a field it is possible to simply assign particle charge to the nearest grid point. However as a particle moves

through the domain the point at which the charge is assigned changes and this will result in a discrete jump in charge density across grid points. This will make for a noisy solution but this can be smoothed by weighting the particle charge between more neighbouring grid points. In the case of charge density $\rho_{\mathrm{j}} \equiv \rho(\mathbf{X}_{\mathrm{j}})$ for charge density at grid point j we get [9],

$$\rho_{\mathrm{j}} = \sum_{\mathrm{i}} q_{\mathrm{i}} S(\mathbf{X}_{\mathrm{j}} - \mathbf{x}_{\mathrm{i}}) \tag{1.56}$$

The fields acting on the particle are interpolated back in exactly the same way. For instance to calculate the electric field acting on particle i, $\mathbf{E}_{\mathrm{i}}$ [9],

$$\mathbf{E}_{\mathrm{i}} = \sum_{\mathrm{j}} \mathbf{E}_{\mathrm{j}} S(\mathbf{X}_{\mathrm{j}} - \mathbf{x}_{\mathrm{i}}) \tag{1.57}$$

The weighting function $S(X)$ depends upon the *shape* function used for the particles. Often these terms are used interchangeably, however the shape function refers to the effective shape of the particle within the domain; a superparticle is not a point in the simulation but instead a region of finite size that moves (but does not rotate) within the domain. The weighting function defines the fraction applied to physical properties weighted from particle to grid and visa versa. By convoluting the particle shape function with a *tophat* function centred at the grid point we find the weighting function. To find the first order triangle weighting function a tophat shape function is convoluted with a tophat function over the cell. The distinction between shape and weight functions is important because a shape function will appear to be an order below the weighting function it produces. For a 1D system, Fig. 1.16 demonstrates three common weight functions, and illustrates how the triangle weighting function is found under this convolution method [9].

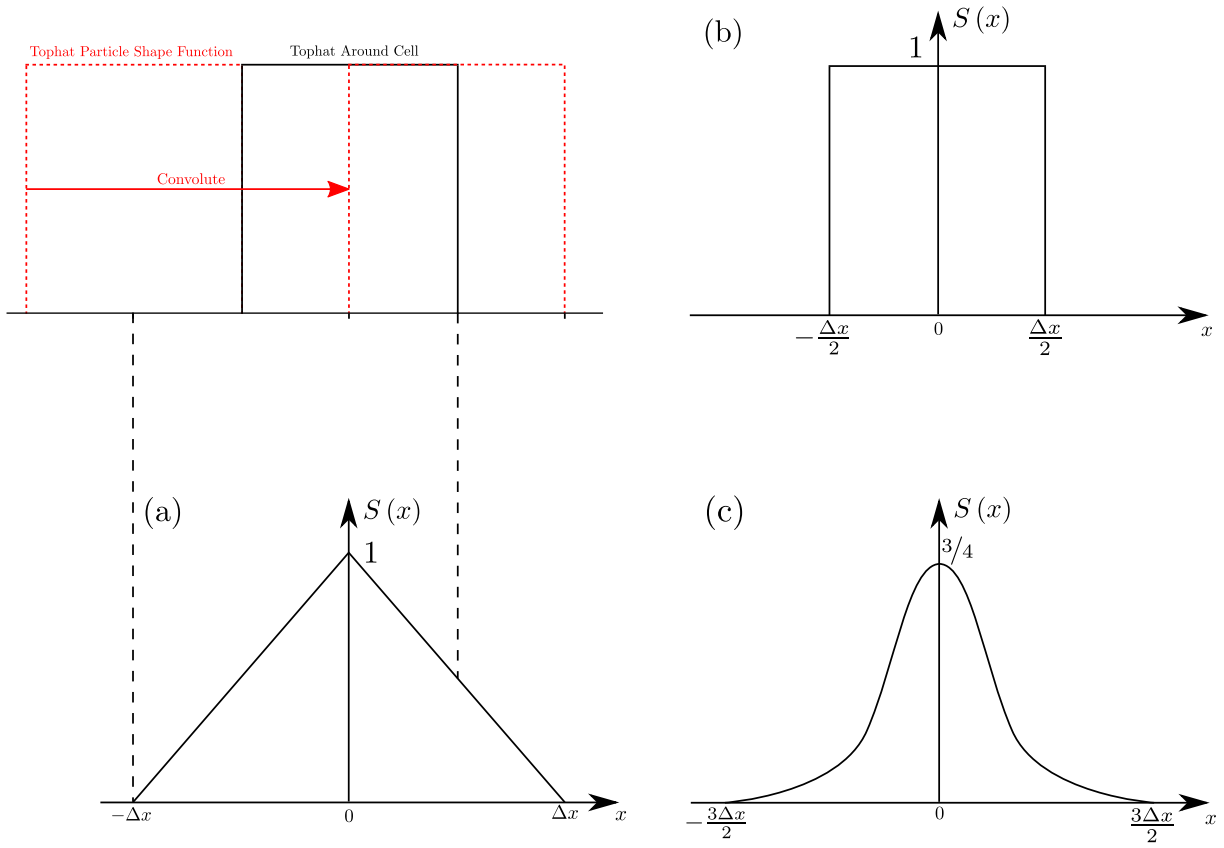

Figure 1.16: The value of weight function $S(x)$ is found by convoluting the shape function of a particle centred around its position, with a tophat function centred around the grid point to which the particle property is being weighted. Three different weighting functions are shown; (a) first order, where the particle shape function is a tophat and the resultant weight function is a triangle as shown above, (b) zero order, a special case where the particle shape function is again a tophat except it is convoluted with a delta function at the grid point; this is equivalent to weighting the whole particle property to whichever grid point the shape function touches, this is also known as *nearest grid point* weighting, (c) second order, found by using the triangle as a shape function. Note how the convolution method produces a weighting function an order higher than the shape function used. [9]

Using a shape function for particles on the grid is effectively the same as describing them as a cloud moving through the domain although these clouds have no internal degrees of freedom. This has a few implications; firstly it demonstrates how the PIC scheme is inherently charge conserving despite particle weighting in that as long as these clouds do not leave the grid then the amount of charge contained in the domain is a constant that is unaffected by use of weight functions. These clouds are also vaguely analogous to the quantum mechanical description of particle position by wavefunction; this isn't entirely unwarranted as usually a single particle in PIC describes the net behaviour of many particles. This is allowed under the scheme because of the q/m_0 term in Eq. (1.48); although the charge and mass of this *superparticle* varies with the number of particles it represents, the ratio remains constant.

1.3.4 Finite Difference Time Domain

Up to this point we have only defined how variables of the fields are handled in time. Now we discuss the spatial grid upon which the fields will be defined; this will require its own finite differencing scheme. It is possible to draw a simple square grid and specify the field values to share the same nodes as shown in Fig. 1.17. For this we define field value $\mathbf{F}^{\mathsf{n}} = \left((F_x)^{\mathsf{n}}_{\mathsf{i,j,k}}, (F_y)^{\mathsf{n}}_{\mathsf{i,j,k}}, (F_z)^{\mathsf{n}}_{\mathsf{i,j,k}} \right)$ for components $F^{\mathsf{n}}_{\mathsf{i,j,k}} = F\left(\mathsf{i}\Delta x, \mathsf{j}\Delta y, \mathsf{k}\Delta z, \mathsf{n}\Delta t\right)$. In this case the central differencing scheme for the $\mathbf{B}$-field update of Eq. (1.53) would be,

$$\begin{aligned}
\frac{\mathbf{B}^{\mathsf{n}+\frac{1}{2}} - \mathbf{B}^{\mathsf{n}-\frac{1}{2}}}{\Delta t} = & \\
& \left(\frac{(E_y)^{\mathsf{n}}_{\mathsf{i,j,k+1}} - (E_y)^{\mathsf{n}}_{\mathsf{i,j,k-1}}}{2\Delta z} - \frac{(E_z)^{\mathsf{n}}_{\mathsf{i,j+1,k}} - (E_z)^{\mathsf{n}}_{\mathsf{i,j-1,k}}}{2\Delta y} \right) \hat{\mathbf{x}} \\
& + \left(\frac{(E_z)^{\mathsf{n}}_{\mathsf{i+1,j,k}} - (E_z)^{\mathsf{n}}_{\mathsf{i-1,j,k}}}{2\Delta x} - \frac{(E_x)^{\mathsf{n}}_{\mathsf{i,j,k+1}} - (E_x)^{\mathsf{n}}_{\mathsf{i,j,k-1}}}{2\Delta z} \right) \hat{\mathbf{y}} \\
& + \left(\frac{(E_x)^{\mathsf{n}}_{\mathsf{i,j+1,k}} - (E_x)^{\mathsf{n}}_{\mathsf{i,j-1,k}}}{2\Delta y} - \frac{(E_y)^{\mathsf{n}}_{\mathsf{i+1,j,k}} - (E_y)^{\mathsf{n}}_{\mathsf{i-1,j,k}}}{2\Delta x} \right) \hat{\mathbf{z}}
\end{aligned} \tag{1.58}$$

The curl expands identically for the $\mathbf{E}$-field update. The scheme as outlined here is numerically unstable for the second order central difference scheme above, and will suffer from the *checker board* instability. This occurs as there is no equation connecting

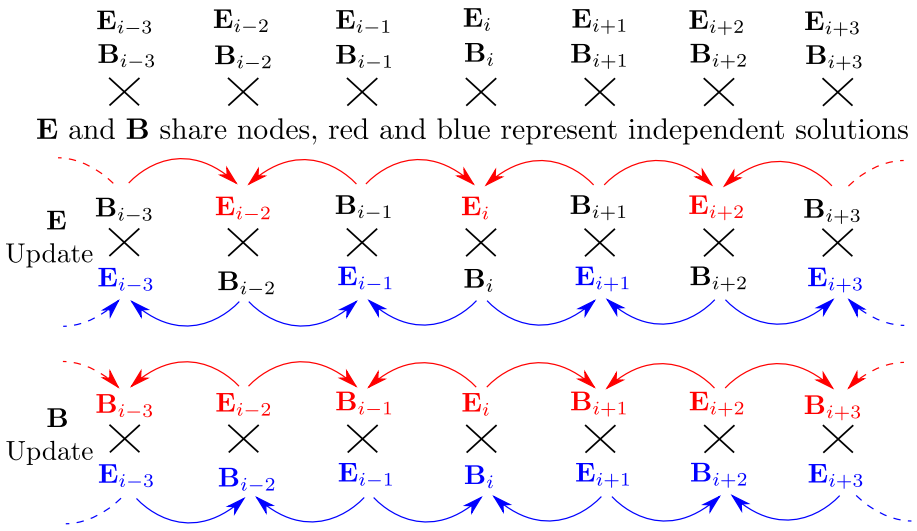

Figure 1.17: $\mathbf{E}-$field values update in 1D using neighbouring $\mathbf{B}-$field values, $\mathbf{B}-$field values update using neighbouring $\mathbf{E}-$field values. $\mathbf{E}-$ and $\mathbf{B}-$field values at the same point never directly interact, and two solutions can diverge.

$\mathbf{E}_{i,j,k}$ to $\mathbf{B}_{i,j,k}$; $\mathbf{E}$ is only updated by neighbouring values of $\mathbf{B}$ and visa versa. The result is that two different solutions in the field values will begin to diverge. Fig. 1.17 more clearly illustrates this instability. One way to avoid this issue is to use a higher order central difference scheme, but it is also possible to eliminate the issue by rearranging the field values upon the grid in such a way that $\mathbf{E}$ and $\mathbf{B}$ do not share nodes and so "see" each other during the spatial field update. A popular method for arranging the grid is known as the *Yee grid* developed by K. S. Yee [42], which is part of a broader category of computational electrodynamics methods known as *finite difference time domain* [43] or FDTD.

The Yee grid staggers the position of grid values such that they appear as in Fig. 1.18; under this grid the field update given in Eq. (1.58) now appears as,

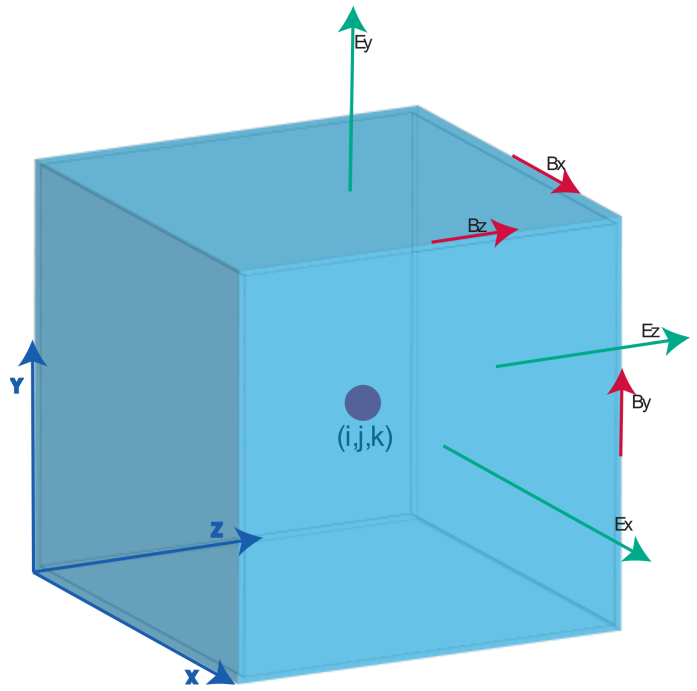

Figure 1.18: Yee grid staggering of field values for a finite difference time domain scheme [42] (image courtesy of C. Brady at the University of Warwick)

$$
\begin{aligned}
&\frac{\mathbf{B}^{n+\frac{1}{2}} - \mathbf{B}^{n-\frac{1}{2}}}{\Delta t} = \\
&\left(\frac{(E_y)^n_{i+1/2,j,k+1/2} - (E_y)^n_{i+1/2,j,k-1/2}}{\Delta z} - \frac{(E_z)^n_{i+1/2,j+1/2,k} - (E_z)^n_{i+1/2,j-1/2,k}}{\Delta y} \right) \hat{\mathbf{x}} \\
&+ \left(\frac{(E_z)^n_{i+1/2,j+1/2,k} - (E_z)^n_{i-1/2,j+1/2,k}}{\Delta x} - \frac{(E_x)^n_{i,j+1/2,k+1/2} - (E_x)^n_{i,j+1/2,k-1/2}}{\Delta z} \right) \hat{\mathbf{y}} \\
&+ \left(\frac{(E_x)^n_{i,j+1/2,k+1/2} - (E_x)^n_{i,j-1/2,k+1/2}}{\Delta y} - \frac{(E_y)^n_{i+1/2,j,k+1/2} - (E_y)^n_{i-1/2,j,k+1/2}}{\Delta x} \right) \hat{\mathbf{z}}
\end{aligned}
\tag{1.59}
$$

Under this scheme the field values within the same cell are linked with each other via the differenced Maxwell's equations which prevents the checkerboard instability. It might appear at first glance at Eq. (1.59) that these are first order finite differencing schemes in space due to missing the factor 2 in the denominator seen in Eq. (1.58). However recall that the $\mathbf{E}$-field values are now half-stepped either side of the $\mathbf{B}$-field values, so the distance between field values used in spatial update is Δ instead of 2Δ.

In addition to the Yee grid being a very elegant and stable method of handling the curls in Maxwell's equations, it is also easily demonstrated that this field staggering does not cause any violation of Gauss' law or the magnetic monopoles condition [43]. For the latter we show that $\frac{\partial}{\partial t}(\nabla.\mathbf{B}) = 0$ as given in Eq. (1.55),

$$\begin{aligned}\frac{\partial}{\partial t}(\nabla.\mathbf{B}) \approx \frac{\partial}{\partial t}\Bigg(&\frac{(B_x)^{\mathsf{n}}_{\mathsf{i}+1/2,\mathsf{j},\mathsf{k}} - (B_x)^{\mathsf{n}}_{\mathsf{i}-1/2,\mathsf{j},\mathsf{k}}}{\Delta x} \\ &+ \frac{(B_y)^{\mathsf{n}}_{\mathsf{i},\mathsf{j}+1/2,\mathsf{k}} - (B_y)^{\mathsf{n}}_{\mathsf{i},\mathsf{j}-1/2,\mathsf{k}}}{\Delta y} \\ &+ \frac{(B_z)^{\mathsf{n}}_{\mathsf{i},\mathsf{j},\mathsf{k}+1/2} - (B_z)^{\mathsf{n}}_{\mathsf{i},\mathsf{j},\mathsf{k}-1/2}}{\Delta z}\Bigg)\end{aligned} \tag{1.60}$$

Using the time differencing from Eq. (1.59) for each B component this expands to,

$$\begin{aligned}&\frac{\partial}{\partial t}(\nabla.\mathbf{B}) \approx \\ &\frac{(E_y)^{\mathsf{n}}_{\mathsf{i}+1/2,\mathsf{j},\mathsf{k}+1/2} - (E_y)^{\mathsf{n}}_{\mathsf{i}+1/2,\mathsf{j},\mathsf{k}-1/2} - (E_y)^{\mathsf{n}}_{\mathsf{i}-1/2,\mathsf{j},\mathsf{k}+1/2} + (E_y)^{\mathsf{n}}_{\mathsf{i}-1/2,\mathsf{j},\mathsf{k}-1/2}}{\Delta x \Delta z} \\ &+\frac{(E_z)^{\mathsf{n}}_{\mathsf{i}-1/2,\mathsf{j}+1/2,\mathsf{k}} - (E_z)^{\mathsf{n}}_{\mathsf{i}-1/2,\mathsf{j}-1/2,\mathsf{k}} - (E_z)^{\mathsf{n}}_{\mathsf{i}+1/2,\mathsf{j}+1/2,\mathsf{k}} + (E_z)^{\mathsf{n}}_{\mathsf{i}+1/2,\mathsf{j}-1/2,\mathsf{k}}}{\Delta x \Delta y} \\ &+\frac{(E_z)^{\mathsf{n}}_{\mathsf{i}+1/2,\mathsf{j}+1/2,\mathsf{k}} - (E_z)^{\mathsf{n}}_{\mathsf{i}-1/2,\mathsf{j}+1/2,\mathsf{k}} - (E_z)^{\mathsf{n}}_{\mathsf{i}+1/2,\mathsf{j}-1/2,\mathsf{k}} + (E_z)^{\mathsf{n}}_{\mathsf{i}-1/2,\mathsf{j}-1/2,\mathsf{k}}}{\Delta x \Delta y} \\ &+\frac{(E_x)^{\mathsf{n}}_{\mathsf{i},\mathsf{j}-1/2,\mathsf{k}+1/2} - (E_x)^{\mathsf{n}}_{\mathsf{i},\mathsf{j}-1/2,\mathsf{k}-1/2} - (E_x)^{\mathsf{n}}_{\mathsf{i},\mathsf{j}+1/2,\mathsf{k}+1/2} + (E_x)^{\mathsf{n}}_{\mathsf{i},\mathsf{j}+1/2,\mathsf{k}-1/2}}{\Delta y \Delta z} \\ &+\frac{(E_x)^{\mathsf{n}}_{\mathsf{i},\mathsf{j}+1/2,\mathsf{k}+1/2} - (E_x)^{\mathsf{n}}_{\mathsf{i},\mathsf{j}-1/2,\mathsf{k}+1/2} - (E_x)^{\mathsf{n}}_{\mathsf{i},\mathsf{j}+1/2,\mathsf{k}-1/2} + (E_x)^{\mathsf{n}}_{\mathsf{i},\mathsf{j}-1/2,\mathsf{k}-1/2}}{\Delta y \Delta z} \\ &+\frac{(E_y)^{\mathsf{n}}_{\mathsf{i}+1/2,\mathsf{j},\mathsf{k}-1/2} - (E_y)^{\mathsf{n}}_{\mathsf{i}-1/2,\mathsf{j},\mathsf{k}-1/2} - (E_y)^{\mathsf{n}}_{\mathsf{i}+1/2,\mathsf{j},\mathsf{k}+1/2} + (E_y)^{\mathsf{n}}_{\mathsf{i}-1/2,\mathsf{j},\mathsf{k}+1/2}}{\Delta x \Delta z}\end{aligned} \tag{1.61}$$

All terms above cancel, which implies that the magnetic monopoles condition is satisfied under the Yee grid scheme providing that it is satisfied at $t = 0$, consistent with Eq. (1.55).

1.3.5 Numerical Stability

The PIC scheme described in this section is an explicit scheme and so is expected to be conditionally stable. To analyse the stability of the method we seek to find the Courant-Friedrichs-Lewy or CFL condition [44] which imposes a limit on a diagnostic value known as the *Courant* number. The Courant number is dimensionless and relates the time step and grid spacing by $C = u\Delta t/\Delta x$ where u is some local flow velocity; in explicit schemes this will have a maximum value above which the scheme becomes numerically unstable.

To analyse the numerical stability of the field solver outlined in §1.3.2, Taflove [43] suggests to look at the dispersion relation derived under the discretised grid. For this we use a plane wave in a vacuum solution of the form $\mathbf{F} = \mathbf{F}_0 \exp(i\omega t - i\mathbf{k}.\mathbf{x})$ where $\tilde{\mathbf{k}}$ is the numerical wavevector [43]. Using this solution and eliminating $\mathbf{B}$ in the two Maxwell's equations yields the dispersion relation; for this we use Ampere's law in the absence of mobile charge on the Yee Grid,

$$\begin{aligned}
\frac{\mathbf{E}^{\mathsf{n}+1} - \mathbf{E}^{\mathsf{n}}}{\Delta t} = \\
\frac{1}{\mu_0 \epsilon_0} \Bigg[& \left(\frac{(B_z)^{\mathsf{n}+1/2}_{\mathsf{i},\mathsf{j}+1,\mathsf{k}+1/2} - (B_z)^{\mathsf{n}+1/2}_{\mathsf{i},\mathsf{j},\mathsf{k}+1/2}}{\Delta y} - \frac{(B_y)^{\mathsf{n}+1/2}_{\mathsf{i},\mathsf{j}+1/2,\mathsf{k}+1} - (B_y)^{\mathsf{n}+1/2}_{\mathsf{i},\mathsf{j}+1/2,\mathsf{k}}}{\Delta z} \right) \hat{\mathbf{x}} \\
& + \left(\frac{(B_x)^{\mathsf{n}+1/2}_{\mathsf{i}+1/2,\mathsf{j},\mathsf{k}+1} - (B_x)^{\mathsf{n}+1/2}_{\mathsf{i}+1/2,\mathsf{j},\mathsf{k}}}{\Delta z} - \frac{(B_z)^{\mathsf{n}+1/2}_{\mathsf{i}+1,\mathsf{j},\mathsf{k}+1/2} - (B_z)^{\mathsf{n}+1/2}_{\mathsf{i},\mathsf{j},\mathsf{k}+1/2}}{\Delta x} \right) \hat{\mathbf{y}} \\
& + \left(\frac{(B_y)^{\mathsf{n}+1/2}_{\mathsf{i}+1,\mathsf{j}+1/2,\mathsf{k}} - (B_y)^{\mathsf{n}+1/2}_{\mathsf{i},\mathsf{j}+1/2,\mathsf{k}}}{\Delta x} - \frac{(B_x)^{\mathsf{n}+1/2}_{\mathsf{i}+1/2,\mathsf{j}+1,\mathsf{k}} - (B_x)^{\mathsf{n}+1/2}_{\mathsf{i}+1/2,\mathsf{j},\mathsf{k}}}{\Delta y} \right) \hat{\mathbf{z}} \Bigg]
\end{aligned} \tag{1.62}$$

On the grid we have $\mathbf{F}|_{\mathsf{i,j,k}} = \mathbf{F}_0 \exp\left(i\tilde{\omega}\mathsf{n}\Delta t - i\tilde{k}_x i\Delta x - i\tilde{k}_y j\Delta y - i\tilde{k}_z k\Delta z\right)$. Considering the y-component and z-components of $\mathbf{B}$ from Eq. (1.59) for substitution into Eq. (1.62) we find,

$$\begin{aligned} B_{y0} = & \frac{E_{z0}\Delta t \exp\left(i\tilde{\omega}\mathsf{n}\Delta t - i\tilde{k}_y\left(\mathsf{j}+1/2\right)\Delta y - i\tilde{k}_z k\Delta z\right)}{\Delta x \exp\left(-i\tilde{k}_x i\Delta x - i\tilde{k}_y\left(\mathsf{j}+1/2\right)\Delta y - i\tilde{k}_z k\Delta z\right)} \\ & \times \frac{\exp\left(-i\tilde{k}_x\left(\mathsf{i}+1/2\right)\Delta x\right) - \exp\left(-i\tilde{k}_x\left(\mathsf{i}-1/2\right)\Delta x\right)}{\exp\left(i\tilde{\omega}\left(\mathsf{n}+1/2\right)\Delta t\right) - \exp\left(i\tilde{\omega}\left(\mathsf{n}-1/2\right)\Delta t\right)} \\ & - \frac{E_{x0}\Delta t \exp\left(i\tilde{\omega}\mathsf{n}\Delta t - i\tilde{k}_x i\Delta x - i\tilde{k}_y\left(\mathsf{j}+1/2\right)\Delta y\right)}{\Delta z \exp\left(-i\tilde{k}_x i\Delta x - i\tilde{k}_y\left(\mathsf{j}+1/2\right)\Delta y - i\tilde{k}_z k\Delta z\right)} \\ & \times \frac{\exp\left(-i\tilde{k}_z\left(\mathsf{k}+1/2\right)\Delta z\right) - \exp\left(-i\tilde{k}_z\left(\mathsf{k}-1/2\right)\Delta z\right)}{\exp\left(i\tilde{\omega}\left(\mathsf{n}+1/2\right)\Delta t\right) - \exp\left(i\tilde{\omega}\left(\mathsf{n}-1/2\right)\Delta t\right)} \\ = & \frac{\Delta t}{\sin\left(\tilde{\omega}\Delta t/2\right)}\left[\frac{E_{x0}}{\Delta z}\sin\left(\tilde{k}_z\Delta z/2\right) - \frac{E_{z0}}{\Delta x}\sin\left(\tilde{k}_x\Delta x/2\right)\right] \end{aligned} \tag{1.63}$$

Similarly,

$$B_{z0} = \frac{\Delta t}{\sin\left(\tilde{\omega}\Delta t/2\right)}\left[\frac{E_{y0}}{\Delta x}\sin\left(\tilde{k}_x\Delta x/2\right) - \frac{E_{x0}}{\Delta y}\sin\left(\tilde{k}_y\Delta y/2\right)\right] \tag{1.64}$$

We expand the x-component of $\mathbf{E}$ in Eq. (1.62) as above with expansion and cancelling of exponential powers then substitution of Euler's equation for sine, then substitute for B_{y0} and B_{z0},

$$\begin{aligned} E_{x0} = & \frac{\Delta t}{\mu_0\epsilon_0 \sin\left(\tilde{\omega}\Delta t/2\right)}\left[\frac{B_{y0}}{\Delta z}\sin\left(\tilde{k}_z\Delta z/2\right) - \frac{B_{z0}}{\Delta y}\sin\left(\tilde{k}_y\Delta y/2\right)\right] \\ = & \frac{\Delta t^2}{\mu_0\epsilon_0 \sin^2\left(\tilde{\omega}\Delta t/2\right)}\left[\frac{E_{x0}}{\Delta y^2}\sin^2\left(\tilde{k}_y\Delta y/2\right) - \frac{E_{y0}}{\Delta x\Delta y}\sin\left(\tilde{k}_x\Delta x/2\right)\sin\left(\tilde{k}_y\Delta y/2\right)\right. \\ & \left. + \frac{E_{x0}}{\Delta z^2}\sin^2\left(\tilde{k}_z\Delta z/2\right) - \frac{E_{z0}}{\Delta x\Delta z}\sin\left(\tilde{k}_x\Delta x/2\right)\sin\left(\tilde{k}_z\Delta z/2\right)\right] \end{aligned} \tag{1.65}$$

We now note that in the absence of mobile charge the fields are divergence-free, therefore finding $\nabla.\mathbf{E} = 0$ on the Yee grid as in Eq. (1.60), substituting the discretised plane wave solution, and using Euler's equation we find,

$$\begin{aligned}\nabla.\mathbf{E} &\approx \frac{E_{x0}}{\Delta x}\sin\left(\tilde{k}_x{}^{\Delta x}/_2\right) + \frac{E_{y0}}{\Delta y}\sin\left(\tilde{k}_y{}^{\Delta y}/_2\right) + \frac{E_{z0}}{\Delta z}\sin\left(\tilde{k}_z{}^{\Delta z}/_2\right) = 0 \\ \Rightarrow &- \frac{E_y 0}{\Delta x \Delta y}\sin\left(\tilde{k}_x{}^{\Delta x}/_2\right)\sin\left(\tilde{k}_y{}^{\Delta y}/_2\right) - \frac{E_{z0}}{\Delta x \Delta z}\sin\left(\tilde{k}_x{}^{\Delta x}/_2\right)\sin\left(\tilde{k}_z{}^{\Delta z}/_2\right) \\ &= \frac{E_{x0}}{\Delta x^2}\sin^2\left(\tilde{k}_x{}^{\Delta x}/_2\right)\end{aligned} \tag{1.66}$$

Substituting Eq. (1.66) into Eq. (1.65) and using $c = (\mu_0\epsilon_0)^{-1/2}$ gives us the 3D numerical dispersion relation on the Yee grid,

$$\begin{aligned}&\sin^2\left(\frac{\tilde{\omega}\Delta t}{2}\right) = \\ &\left(\frac{c\Delta t}{\Delta x}\right)^2\sin^2\left(\frac{\tilde{k}_x\Delta x}{2}\right) + \left(\frac{c\Delta t}{\Delta y}\right)^2\sin^2\left(\frac{\tilde{k}_y\Delta y}{2}\right) + \left(\frac{c\Delta t}{\Delta z}\right)^2\sin^2\left(\frac{\tilde{k}_z\Delta z}{2}\right)\end{aligned} \tag{1.67}$$

$\mathbf{F} = \mathbf{F}_0\exp\left(i\omega t - i\mathbf{k}.\mathbf{x}\right)$ will grow unstably when ω has an imaginary component. Following the procedure laid out in [43] Eq. (1.67) gives the form of an imaginary frequency as,

$$\begin{aligned}&\tilde{\omega} = \frac{\pi}{\Delta t} - i\frac{2}{\Delta t}\ln\left(\xi + \sqrt{\xi^2 - 1}\right) \text{ where,} \\ &\xi = c\Delta t\sqrt{\frac{1}{\Delta x^2}\sin^2\left(\frac{\tilde{k}_x\Delta x}{2}\right) + \frac{1}{\Delta y^2}\sin^2\left(\frac{\tilde{k}_y\Delta y}{2}\right) + \frac{1}{\Delta z^2}\sin^2\left(\frac{\tilde{k}_z\Delta z}{2}\right)} \\ &\Rightarrow \mathbf{F}|_{\mathrm{i,j,k}} = \mathbf{F}_0\left(\xi + \sqrt{\xi^2 - 1}\right)^{2n}\exp\left(i\pi\mathrm{n} - i\tilde{k}_x i\Delta x - i\tilde{k}_y j\Delta y - i\tilde{k}_z k\Delta z\right)\end{aligned} \tag{1.68}$$

The $\left(\xi + \sqrt{\xi^2 - 1}\right)^{2n}$ defines a growth rate for an instability which is real valued when $\xi > 1$. ξ is largest when $\sin^2\left(\tilde{k}_x{}^{\Delta x}/_2\right) = \sin^2\left(\tilde{k}_y{}^{\Delta y}/_2\right) = \sin^2\left(\tilde{k}_z{}^{\Delta z}/_2\right) = 1$, and so we can define our Courant number as $C = c\Delta t\sqrt{1/\Delta x^2 + 1/\Delta y^2 + 1/\Delta z^2}$. When $\xi < 1$ the frequency has no imaginary component and the instability does not occur. For a 3D grid where $\Delta x = \Delta y = \Delta z = \Delta$ we can now find a stable limit upon the

Courant number as $C_{\text{3D max}} = c\Delta t\sqrt{3/\Delta^2} = \sqrt{3}C$ [43]. Equivalently in 1D and 2D we find $C_{\text{1D max}} = C$ and $C_{\text{2D max}} = \sqrt{2}C$. We interpret these maxima as meaning that an electromagnetic wave should not be able to travel further than the *finite difference stencil* in a single timestep. The finite difference stencil is the space spanned by all the variables used in the update; in second order as shown here this is a single grid cell, in higher orders we expect the space spanned to be larger. This is easily understood as to travel further would mean that the wave does not interact with all of the domain it passes through; the spatial update would not have time to "see" the wave passing through it and the field values would update as though the wave had not been present.

As we have considered an electromagnetic wave in the absence of free charges we essentially have only an analysis of the stability properties of the grid. Adding superparticles to the simulation introduces new instabilities which must be taken into account. Analysing stability in this case requires that we include the motion of these charged superparticles on the grid. The method to find stability requirements proceeds as for the grid; find dispersion relations for the plasma and identify any potential for unstable growth. Finding the dispersion relations in this case is notably more complex, and strongly dependent on the weighting functions applied to the particles. We use results from Birdsall and Langdon [9] here to illustrate the two major instabilities. Birdsall and Langdon derive the numerical plasma dispersion relation for a single species in a neutralising background under a cold, drifting plasma approximation as,

$$\omega = \mathbf{k}\cdot\mathbf{v} \pm 2/\Delta t \arcsin\left(\omega_{pe}\Delta t/2\right) \tag{1.69}$$

This reveals the stability requirement for freely moving particles on the grid; when $\omega_{pe}\Delta t > 2$ the frequency becomes imaginary. This is simply a statement that the plasma frequency must be resolved upon the grid. In other words the time step should not be so large that the small scale oscillation of electrons cannot be captured. This can be shown to also hold true for a warm plasma [9]. As resolving for the frequency of a travelling wave on the Yee grid is already a requirement we take our stability requirements $\Delta t_p < 2/\omega_{pe}$ and $\Delta t_E < \sqrt{3}c\Delta t/\Delta$ giving $\Delta t < \min\left(\Delta t_{pe}, \Delta t_E\right)$.

Another stability consequence for the introduction of free charges in the grid can

be found when looking at a cold electron beam against a fixed ion background. Birdsall and Langdon [9] derive another 1D dispersion relation for a cold electron beam with velocity v_0 in a background of immobile neutralising ions. In this way they are able to identify a numerical instability that occurs when the oscillation of the electrons is in resonance with the frequency at which they cross the gridpoints. For context, Birdsall and Langdon note that when the Doppler-shifted frequency of the electron oscillations $\omega - kv_0$ is near the *grid-crossing* frequency $k_g v_0$ for grid wave number $k_g = {}^{2\pi}/_{\Delta x}$, the particles show resonances given by $w - kv_0 + pk_g v_0 = 0$ for $p \in \mathbb{Z}$. They find the resonances are largest near $p = 0$, so including this and one other $p \neq 0$ term then considering the dispersion relation near these resonances for $S(k_p)$ the wave number weighted to the particle position by shape function S they find [9],

$$\omega \approx kv_0 \pm \omega_p \frac{S(k_p)}{2k \sin({}^{k\Delta x}/_2)} \sqrt{\frac{\Delta x k_p \sin(k_p \Delta x)}{1 - ({}^{w_p}/_{pk_g v_0})^2}} \tag{1.70}$$

From Birdsall and Langdon's result we can see that the frequency becomes imaginary for $\omega_p > pk_g v_0$ which can be rewritten $\lambda_D < 2\pi p \Delta x$ for λ_D the Debye length for the plasma. This implies that the Debye length needs to be resolved to a degree on the grid. However unlike the other instabilities presented here, it is found not to arise often even when the grid spacing is significantly larger than a Debye length. The instability is found to be highly dependent on the interpolation used for shape function S, and when using third order splines in low densities the grid cell can span hundreds of Debye lengths without the instability occurring. In Birdsall and Langdon's results, nearest gridpoint weighting described in (b) of Fig. 1.16 is used and therefore indicates the worst case scenario. In addition the instability is found only to grow for a time and then to stabilise itself. This is because the particles rapidly heat under this instability, thus the Debye length increases to the point that it is resolved upon the grid. Due to this most simulations using PIC do not resolve the Debye length as the instability rarely manifests and when it does it is rarely catastrophic to the simulation. As a user of PIC codes it serves simply to be aware of the potential for self-heating under the instability so that the problem can be identified should it arise. At that point a higher order particle shape function or a finer grain grid may be used.

Chapter 2

Ionisation in EPOCH

Since a standard PIC code does not model individual photons, any model used must be able to rely solely on the instantaneous field values interpolated to the particle from the grid points. Due to the nature of the leapfrog scheme described in §1.3.2 the ionisation needs to be performed when the field values are available which may be at the half or full timestep depending on the scheme. In addition the code requires a means of dynamically adding particles to the simulation; with a very heavy element there is the potential for over a hundred electron and ion superparticles to be added to the domain per single neutral superparticle, so care should be taken to ensure the ionisation scheme cannot flood the simulation with particles. A complete ionisation model also includes ionisation by free electron impact as many laser-plasma interactions of interest occur at solid densities where the plasma may be highly collisional. In this chapter we introduce the Extendable PIC for Open Collaboration or EPOCH as the core PIC code for this study, and in this context the models for ionisation are given with a detailed description of the means for implementing them into the code. A condensed description of the field ionisation models and algorithm used has been previously published in Physics of Plasmas in June 2012 [1], whilst both the field and collisional ionisation model descriptions are currently in preparation for submission to the Journal of Computational Physics [45].

2.1 EPOCH

The Extensible PIC Open Collaboration or EPOCH [45] is a project originally developed by Chris Brady at the University of Warwick. EPOCH is now developed and maintained by Keith Bennett and a number of contributors from multiple institutions through the Collaborative Computational Plasma Physics (CCPP) group including various UK universities, UKAEA, Culham, RAL and AWE[1]. Written in Fortran, it includes parallelism via MPI [46] and is designed specifically to encourage extensions for additional physics and functionality. The core of the code is taken from PSC by Hartmut Ruhl [12] which bears many similarities to the standard PIC code described in §1.3. The principal differences lie in how Gauss' law is satisfied which is covered in §2.1.3 and also how the field updates which we will demonstrate is only a minor modification upon the finite difference time domain scheme described in §1.3.4. The electric and magnetic field updates are handled in a leapfrog fashion but the scheme implemented in EPOCH is altered such that both fields are known at half time steps [45]. This is required by the particle pushing scheme which uses time-centred grid values for second-order accuracy but it is also helpful for modules that use the fields at half time steps. The resulting field update algorithm appears as,

1. Half electric field update $\mathbf{E}_{t+\Delta t/2} = \mathbf{E}_t + {}^{\Delta t}/_{2}\left(c^2\nabla \times \mathbf{B}_t - \frac{\mathbf{J}_t}{\epsilon_0}\right)$
2. Half magnetic field update $\mathbf{B}_{t+\Delta t/2} = \mathbf{B}_t + {}^{\Delta t}/_{2}\left(\nabla \times \mathbf{E}_{t+\Delta t/2}\right)$
3. Particle pusher and current density updates
4. Second half magnetic field update $\mathbf{B}_{t+\Delta t} = \mathbf{B}_{t+\Delta t/2} + {}^{\Delta t}/_{2}\left(\nabla \times \mathbf{E}_{t+\Delta t/2}\right)$
5. Second half electric field update $\mathbf{E}_{t+\Delta t} = \mathbf{E}_{t+\Delta t/2} + {}^{\Delta t}/_{2}\left(c^2\nabla \times \mathbf{B}_{t+\Delta t} - \frac{\mathbf{J}_{t+\Delta t}}{\epsilon_0}\right)$

[1] Current source base maintained at http://www.ccpp.ac.uk/

At first glance it's not immediately obvious how this relates to the leapfrog scheme. However, consider the second electric field update for the $t - \Delta t \rightarrow t$ timestep such that $E_{t-\Delta t/2} \rightarrow E_t$ then continue with the first three updates in the next time step such that $E_t \rightarrow E_{t+\Delta t/2}$, $B_t \rightarrow B_{t+\Delta t/2}$, then $B_{t+\Delta t/2} \rightarrow B_{t+\Delta t}$. We can now see much more clearly that the half updates for E follow each other; the same is true for B. It is therefore valid to substitute the $E_{t-\Delta t/2} \rightarrow E_t$ update into the $E_t \rightarrow E_{t+\Delta t/2}$ update and the $B_t \rightarrow B_{t+\Delta t/2}$ into the $B_{t+\Delta t/2} \rightarrow B_{t+\Delta t}$ to obtain equivalent field updates, which we can immediately observe to be the leapfrog scheme outlined in §1.3.2,

$$\begin{aligned} \mathbf{E}_{t+\Delta t/2} &= \mathbf{E}_{t-\Delta t/2} + \Delta t \left(c^2 \nabla \times \mathbf{B}_t - \mathbf{J}_t \right) \\ \mathbf{B}_{t+\Delta t} &= \mathbf{B}_t + \Delta t \left(\nabla \times \mathbf{E}_{t+\Delta t/2} \right) \end{aligned} \tag{2.1}$$

Outside of the core PIC algorithm EPOCH includes a number of features including partial reconstruction of distribution functions, compatibility for IDL, VisIt, Matlab, python data analysis, and so on. In the remainder of this section we seek to highlight specific features of particular relevance to developing an ionisation module for EPOCH.

2.1.1 Input Deck

The input deck allows the user to set up a simulation without a direct modification to the source code. Offering an interface to running EPOCH allows users to work with a common executable which eases the strain of maintenance and reduces the prior knowledge of the code base required to run simulations. By enforcing a common interface this also ensures that if specific versions of the code are produced then no further knowledge of the differences should be required beyond knowing the additional options required in the deck, provided they are added by the code author. The deck is split into blocks that control different simulation parameters and have the general format,

```
begin:blockname
  content = 9
  multiple_variables = T

  #I am a comment
end:blockname
```

The deck also includes a maths parser allowing variables to be defined as functions of another. Not every category of block needs to be present in an input deck, and sensible defaults are used where possible. The available blocks are,

- control; global properties such as domain size, simulation time and load balancing
- boundaries; boundary conditions and attaching laser sources
- species; particle properties, one block per species
- constants; user-defined constants and functions
- output; frequency and content of output, including frequency of distribution function output
- dist_fn; content, range and resolution of reconstructed distribution functions
- laser; properties of the laser sources
- fields; applied fields at any point of the domain

Within the code the input deck is read in two passes to allow the blocks to be in any order. The first pass checks which blocks are present and ensures the essential blocks and content are available such as the control block and domain size. EPOCH allocates memory for the grid and particles and in the second pass the initial conditions are read in. In general the first pass may throw an error if important blocks aren't defined and the second will throw an error if conditions are invalid or there is a syntax error. When extending EPOCH and modifying the input deck it is important to consider what variables are required to set up memory correctly and ensure these are read in the first pass.

2.1.2 Particle Species and Lists

Since the number of particles in the simulation can be very large and change dynamically it is important to have a suitable data structure to cope with this. For this reason EPOCH makes use of linked lists, a data structure which functions as a variably sized array that can change dynamically without reallocating memory. An element of a linked list will have at minimum two variables; its value and a pointer to the next element in the list. It is clear from this that a linked list has higher memory overheads per element

than a normal array but has the advantage of making reorganising, removing or adding elements computationally inexpensive tasks. The list itself may simply contain a pointer to the first element of the list. Outlines for the derived types for EPOCH are as follows,

```
TYPE particle
  ! particle specific properties here e.g. position, momentum
  TYPE(particle), POINTER :: next, prev
END TYPE particle


TYPE particle_list
  TYPE(particle), POINTER :: head
  TYPE(particle), POINTER :: tail
  INTEGER(KIND=8) :: count
  INTEGER :: id_update
  ! Pointer is safe if the particles in it
  ! are all unambiguously linked
  LOGICAL :: safe
END TYPE particle_list


TYPE particle_species
  ! particle properties that aren't required on a
  ! per particle basis e.g. charge, mass
  TYPE(particle_species), POINTER :: next, prev
  TYPE(particle_list) :: attached_list
  ! Secondary list
END TYPE particle_species
```

The particle list knows how many elements it has and if its list contains only safely linked particles, in addition to knowing the start and end particle of the list. A particle species type holds the lists, as well as more global particle properties to reduce the amount of memory used per particle. The secondary list in the species is used to store particle lists on a per grid cell basis which is important for collisions when grouping particles by proximity is important.

2.1.3 Charge Conservation

Due to numerical error build up during PIC simulation, Gauss' law cannot be assumed to be satisfied for all time even when satisfied initially as discussed in §1.3.2. In EPOCH, this is tackled by calculating the change in charge density at every time step and solving

the additional equation $\frac{\partial \rho}{\partial t} = -\nabla \cdot \mathbf{J}$ to provide the current density to the field update [45]. This is the Villasenor and Buneman current correction scheme [47]. This scheme turns out to be a very intuitive one; when a portion of a particle shape function leaves a cell and enters another, the corresponding fraction of its charge is removed from the first cell and added to the second where the size of this fraction is defined by the shape function. This scheme conserves charge locally in every grid cell ensuring global charge conservation. As the field updates are second order central differenced we require the current densities to be updated to the same accuracy. For the second electric field update we need to perform the calculation,

$$-\nabla \cdot \mathbf{J}_{t+\Delta t} = \frac{\rho_{t+\Delta t/2} - \rho_{t+3\Delta t/2}}{\Delta t} \tag{2.2}$$

This presents a problem as $\rho_{t+3\Delta t/2}$ is based on the particle positions at $t + 3\Delta t/2$ which are unknown; a first order approximation is applied here by advancing the particle positions forward in time by $\Delta t/2$ using the momenta calculated at $t + \Delta t$. The particle positions at $t + \Delta t/2$ are known due to the three-step Boris rotation scheme outlined in §1.3.1.

2.1.4 Collisions

In PIC particles interact with each other through field values resolved upon the grid; interactions on scales smaller than the grid resolution are not resolved therefore Coulomb collision is essentially neglected. For laser-plasma interactions at lower densities this will be a reasonable assumption as the characteristic time for collision will be large compared to the simulation time-scales but at solid densities this is no longer valid and collisions become important. EPOCH includes a module for modelling collisions written by M.G. Ramsay and H. Schmitz based on an algorithm by Sentoku and Kemp [48] which provides an energy-conserving scheme for relativistically colliding superparticles of differing weights.

The collisions module requires that the particle lists be divided into the per cell secondary lists and within these cells the collisions are performed for every combination of binary collision between particle species. Under this model a collision frequency

between two superparticles is calculated based on the charge, densities, and the relative momentum for every collision. This collision frequency is then used to find an expected number of collisions over the timestep which is then used to define the variance of a Gaussian distribution from which the scattering angle is sampled. Large scattering angles are neglected as these should appear only in the tails of the distribution and in a simulation with limited particles per cell this lowers the quality of the phase space [48]. Once this scattering angle is found a relativistic elastic collision is performed between the two superparticles.

The collision frequency between superparticles α and β is given in Eq. (2.3) for relative velocity of the particles v_{rel}, Z and n the species charge and density respectively, $\log\left(1/\sigma_{\mathsf{min}}\right)$ the Coulomb logarithm for σ_{min} the smallest scattering angle that can still be considered a Coulomb collision and p_{rel} the relative momentum of the particles [48].

$$\nu_{\alpha\beta} = \frac{4\pi \left(Z_\alpha Z_\beta\right) \mathsf{min}\left(n_\alpha, n_\beta\right) \log\left(1/\sigma_{\mathsf{min}}\right)}{p_{\mathsf{rel}}^2 v_{\mathsf{rel}}} \tag{2.3}$$

The Coulomb logarithm is the integral of $1/b$ where b is the distance of closest approach during the binary collision so for example in the classical case σ_{min} is the scattering angle for which b is the Debye length [48]. In EPOCH it is possible to provide the Coulomb log in the input deck, otherwise EPOCH calculates it automatically as,

$$\sigma_{\mathsf{min}} = \log\left(4.13 \times 10^6 \left(\frac{e}{k_b}\right)^{3/2} \left(\frac{1}{Z_\alpha}\right)^2 \left|\frac{1}{Z_\beta}\right| \sqrt{\frac{T_\alpha^3}{n_\beta}}\right) \tag{2.4}$$

The collisions under this model remain perfectly energy conserving when colliding superparticles of different weights. This is achieved by adjusting the collision time based on the relative weights represented by the superparticles. Sentoku and Kemp explain this in terms of the probability of collision between two particles; for particle α and β of weight w_α and w_β respectively and N_α the number of α superparticles we have that the total number of collisions is $n_{\alpha\beta}$ [48],

$$\mathbb{P}\left(\alpha \text{ collides with } \beta\right) = \frac{w_\beta}{\mathsf{max}\left(w_\alpha, w_\beta\right)} \Rightarrow n_{\alpha\beta} = \sum_i^{N_\alpha} \frac{w_{\alpha i} w_{\beta i}}{\mathsf{max}\left(w_\alpha, w_\beta\right)} = \sum_i^{N_\alpha} \mathsf{min}\left(w_\alpha, w_\beta\right) \tag{2.5}$$

The adjusted collision time is given by $\Delta t_c = {}^{n_\alpha}/_{n_{\alpha\beta}}$; the scattering angle is now sampled from a Gaussian distribution with a variance of $\left\langle \tan^2 \left({}^{\sigma}/_{2}\right)\right\rangle = \nu_{\alpha\beta}\Delta t_c$ [48].

2.2 Ionisation Models

As presented in §1.2.2 there is no single method for modelling all potential routes to ionisation for any given atom. Within the atom itself ionisation depends upon the level of excitation for the electron to be released. Depending on the time-scale this is influenced by relaxation processes such as spontaneous emission [49]. Externally incident radiation may be absorbed such that an electron may simply be excited rather than ionised, or it may undergo stimulated emission from an incident photon and relax to a lower energy state [49]. Modelling field ionisation becomes more complex when considering the Stark effect [34] in which an applied electric field causes deformation of atomic energy levels. In a time-varying electric field such as that imposed by a laser we find that the product of excitation and relaxation processes leading up to ionisation can cause even ionisation by direct-photon absorption to be a non-linear process.

Considering collisions increases the complexity of a model for ionisation as any field ionised electrons can go on to be involved in Coulomb collisions with bound electrons which can result in further ionisation. However electron-electron impact does not necessarily result in ionisation or even excitation; it may result in de-excitation of the bound electron with photon emission. It may also result in de-excitation of the free electron which may lead to recombination. This can also occur if the incident electron undergoes spontaneous emission. Both effects will serve to reduce the ionisation level of a plasma, therefore any collisional ionisation model should ideally include all these effects.

A quick schematic summary for some of the processes relating to ionisation is given for A_G the neutral atom in the ground state, A_E the neutral atom in the excited state, A^+ the ionised atom, e a free electron and ϵ_{xy} energy to excite the atom from state x to state y,

$$\begin{array}{rcl} \rightarrow & & \leftarrow \\ \text{Excitation} & A_\mathsf{G} + \epsilon_\mathsf{GE} \leftrightarrow A_\mathsf{E} & \text{Relaxation} \\ \text{Field Ionisation} & A_\mathsf{G} + \epsilon_{\mathsf{G}+} \leftrightarrow A^+ + e & \text{Two-Body Recombination} \\ \text{Collisional Ionisation} & A_\mathsf{G} + e + \epsilon_{\mathsf{G}+} \leftrightarrow A^+ + e + e & \text{Three-Body Recombination} \end{array} \tag{2.6}$$

As can be seen from this brief analysis of the processes relevant to ionisation, any complete ionisation model for plasmas will either include all of the above effects and be highly complex or otherwise selectively neglect some such that it operates only over certain time-scales and energies. An examples of restrictions on the time-scale would be to choose it short enough such that recombination processes may be neglected, and an example for energy restriction might be to assume photon energies high enough that excitation is unimportant; this is the case when the photon energy is enough for direct ionisation.

As the purpose of this study is to include ionisation into a PIC code we can take advantage of knowing the conditions local to an ionising superparticle at each time step, which allows us to choose our assumptions conditionally. For collisional ionisation three-body recombination is shown to occur on similar time-scales in [50] and so if the plasma is collisional both should be included. However to decide how best to choose the assumptions for field ionisation and reduce the problem it is prudent to review likely applications; typical laser wavelengths in laboratory laser-plasma interactions tend to be of the order of $\sim 0.1\mu\text{m} - 1\mu\text{m}$ where the photon energy will be $\sim 1\text{eV} - 10\text{eV}$ therefore a single photon is unable to directly ionise even the most weakly bound electron in many elements. Therefore any direct photon ionisation model would be a poor estimate, and we must use the multiphoton and tunnelling field models outlined in §1.2.2.

In the multiphoton regime electron excitation is taken into account by assuming multiple photon absorptions leading to ionisation but in the tunnelling regime it is relatively unimportant compared to the sharp Stark shifting of energy levels as discussed

in §1.2.2. In the context of inertial confinement fusion, relevant intensities would be in the range $10^{14}\text{Wcm}^{-2} - 10^{16}\text{Wcm}^{-2}$; from the Keldysh parameter shown in Eq. (1.43) hydrogen would be ionising in the tunnelling regime but for example the inner shell of carbon would be ionising in the multiphoton regime. Many laser-plasma interactions are explored at higher peak intensities where tunnelling becomes a reasonable model for most bound electron states. However these pulses still have a rise time where the intensities will be lower and multiphoton models may be more applicable, therefore both models should be included and switched between using the Keldysh parameter. Here we present the models used for field and collisional ionisation.

2.2.1 Multiphoton Ionisation

§1.2.2 introduced field ionisation and the Keldysh parameter for comparing the relative effects of photon energy and laser intensity. It was shown that it amounted to a direct comparison of ionisation by multiple absorption of photons and ionisation by deformation of atomic energy levels lowering the ionisation energy. These are not competing but complimentary effects. A model for hydrogen-like particles was given in Eq. (1.42); it was shown that when $\gamma \gg 1$ the scaling of ionisation rate with incident laser field intensity I went as I^K where K is the number of photons absorbed and γ is the Keldysh parameter. This scaling is characteristic of multiphoton ionisation [34]. The Keldysh multiphoton ionisation rate shown in Eq. (1.42) is highly complex and only valid for hydrogen without further correction [35], so we instead make use of a multiphoton ionisation rate based on a cross-section for the absorption of multiple photons [34] where E is the self-consistent electric field strength at the particle given in atomic units.

$$W_{\text{Multi}} = \sigma^{(K)} \left(\frac{cE^2}{8\pi\omega} \right)^K \tag{2.7}$$

Here $\sigma^{(K)}$ is the generalised multiphoton cross-section which depends on the laser frequency and polarisation as well as the number of absorbed photons and the atom energy levels. Analytical expressions of cross-section are only available for hydrogen atoms. For complex atoms the cross-sections must be experimentally determined or otherwise approximated [34]. Ideally the cross-section would be experimentally de-

termined for each atom but as such data is limited we make use of a semi-empirical WKB approximation below by Ammosov *et al.* [34] given in Hartree atomic units for K-photon ionisation of a general hydrogen-like series of excited states known as *Rydberg* states which is a reasonable approximation of the excited states of many atoms [37]. Recall that the dependence on ionisation energy is included through the variable $K = \lfloor \epsilon/\hbar\omega + 1 \rfloor$,

$$\sigma_n^{(K)} = \frac{4.8\,(1.3)^{2K}\,E^{2K-2}}{cK!^2 n^5 \omega^{(\frac{10K-1}{3})}\sqrt{K}\,(2K-1)} \tag{2.8}$$

2.2.2 Tunnelling Ionisation

As in the multiphoton case Eq. (1.40) is only suitable for modelling the tunnelling ionisation rate in hydrogen atoms as it includes no corrections for different electron orbitals or excited states. Excited states were considered by Perelomov *et al.* [51] and this work was extended to produce the Ammosov, Delone, Krainov or ADK equation for ionisation rate which is suitable for complex ions of arbitrary principle, angular and magnetic quantum numbers [38]. All quantum numbers shown here are for a specific electron orbital. ADK theory has been shown to produce good agreement with experiment [52]. This ADK equation makes use of an effective principle quantum number for an electron orbital $n^* = \frac{Z}{\sqrt{2\epsilon}} = n - \delta_n$ where δ_n is the quantum defect. The quantum defect is a correction arising from the fact that outer shell electrons are not perfectly shielded from the nucleus as even outer orbitals will occasionally pass close enough to *feel* it. Hartree atomic units are used here again and therefore ϵ is given in terms of the Hartree energy which is approximately twice the ionisation energy of hydrogen. n_0^* is used to represent the effective principle quantum number for the electron when the atom is in the ground state.

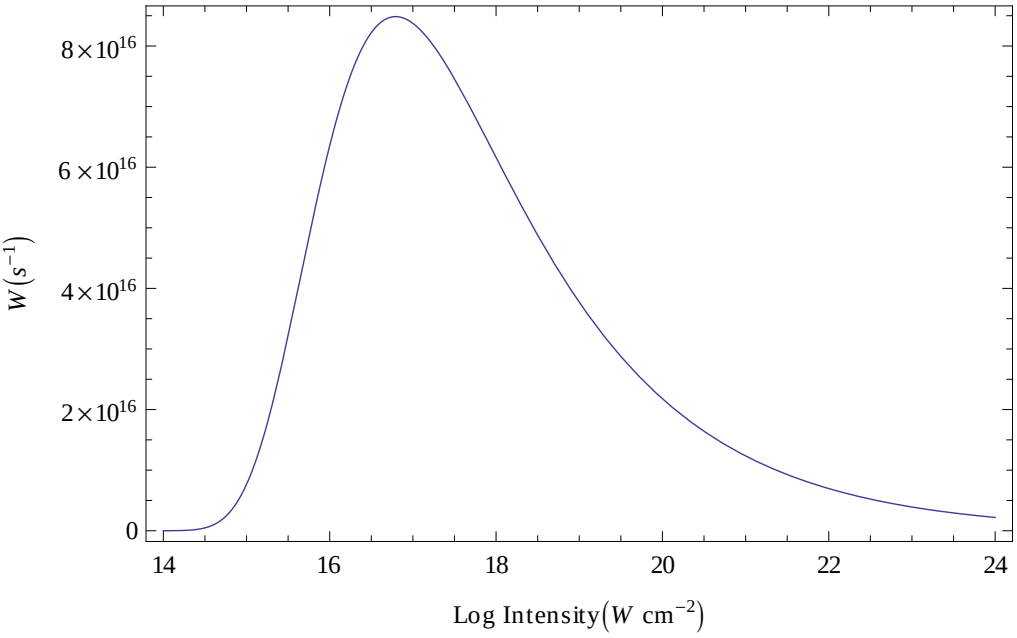

Figure 2.1: ADK ionisation rate for hydrogen entering the barrier-suppression regime demonstrating the unphysical rise and drop off of ionisation rate with increasing laser field strength; this region is considered an overestimate of the ionisation rate [34].

The ADK ionisation rate is given below for Z the charge of the ionised species, $l^* = n_0^* - 1$ the effective angular quantum number, m the magnetic quantum number and l the angular quantum number.

$$W_{\text{ADK}} = \frac{\epsilon 2^{2n^*}}{n^* \Gamma\left(n^* + l^* + 1\right) \Gamma\left(n^* - l^*\right)} \left(\frac{3E}{\pi \left(2\epsilon\right)^{3/2}}\right)^{1/2} \frac{(2l+1)(l+|m|)!}{2^{|m|}\left(|m|\right)!\left(l-|m|\right)!} \times \left(\frac{\left(2\epsilon\right)^{3/2}}{E}\right)^{2n^*-|m|-1} \exp\left(-\frac{2\left(2\epsilon\right)^{3/2}}{3E}\right) \tag{2.9}$$

As in the case of $\gamma \ll 1$ for the Keldysh model in the low frequency regime, the scaling of the ionisation rate goes with incident laser field intensity as $\exp\left(-\frac{1}{I^{1/2}}\right)$ and has no dependence on laser frequency which is characteristic of tunnelling ionisation as discussed in §1.2.2.

2.2.3 Barrier-Suppression Ionisation

There is a third regime beyond tunnelling when the energy of the laser field becomes greater than the binding energy of the electron such that it is possible for the electron to escape classically. This is known as the barrier-suppression ionisation or BSI regime. In this regime the ADK tunnelling rate Eq. (2.9) demonstrates an unphysical drop off in ionisation rate with increasing field intensity as demonstrated in Fig. 2.1; at this point ADK becomes a poor approximation of the ionisation rate. Posthumus *et al.* provide a purely classical formula for the ionisation rate for BSI with which to extend ADK equation into the regime [53] where they suggest to add their result to the ADK rate at a suitable threshold electric field E_c as shown in Eq. (2.10). This threshold is chosen to be where the laser field strength is equal to an approximation of the electrostatic field binding the electron from [34].

$$\begin{aligned} W_{\text{BSI}} &= \frac{(2\epsilon)^{3/2}\left(1-\frac{\epsilon^2}{4ZE}\right)}{4\pi Z} \\ W_{\text{total}} = W_{\text{BSI}} + W_{\text{ADK}}\left(E_c\right) \qquad & E_c = \frac{Z^3}{16n^{*4}} \end{aligned} \tag{2.10}$$

2.2.4 Electron Impact Ionisation

At solid densities particle collision becomes of greater significance and it becomes necessary to consider ionisation by electron impacting upon and exciting a bound electron. The probability of electron-electron impact can be defined via a cross-section. This cross-section is influenced by many factors such as the energy of both electrons, the charge state of the atom, the orbit of the bound electron and so on. It is not possible to obtain an analytical expression for the cross-section of every bound electron and it is typical to use experimental cross-sectional data. Such data is unavailable in most cases but useful approximations exist in the absence of empirical data. A general empirical or semi-empirical model for electron impact ionisation cross section doesn't exist; instead there are multiple models for specific cases for the element and orbital contains the ionising electron [54], the ionic charge and incident electron energies [55]. In this case we make use of the modified BELL (MBELL) equation [56] where the BELL equation (also known as the BELI equation) was developed from analytical fits of extensive empirical

data by Bell *et al.* [57]. BELL is for light ionic targets including s-, p-, and d-orbitals for $n \leq 3$, and MBELL includes modifications for an ionic target ($q > 1$) and relativistic electron energies. The form of the MBELL model is presented by A. K. F. Haque *et al.* [56] and is shown in Eq. (2.11) where nl indicates a particular suborbital (e.g. 1s, 2s, 2p, etc.) and N_{nl} is the number of electrons in the suborbital. The remaining terms are described below,

$$\sigma_{\text{MBELL}} = \sum_{nl} N_{nl} F_{\text{ion}} G_R \sigma_{\text{BELI}} \times 10^{-4} \tag{2.11}$$

- σ_{BELI} is the BELL model cross section presented to the incident electron by the nl suborbital. This is given below for ϵ the ionisation energy of the nl-orbit, ϵ_I the incident electron energy in the frame of the target ion, $U = \epsilon_I/\epsilon$ the reduced energy, and empirical parameters A and B_i shown in table 2.1 [56],

$$\sigma_{\text{BELI}} = \frac{1}{\epsilon_I \epsilon} \left[A \ln U + \sum_{i=1}^{7} B_i \left(1 - \frac{1}{U}\right)^i \right] \tag{2.12}$$

- G_R is a term to take into account relativistic effects called the Gryzinski relativistic factor [58]. For $J = 1/L = m_e c^2/\epsilon$ the where L is ionisation energy scaled to the electron rest mass energy, this is given by [56],

$$G_R = \left(\frac{1+2J}{U+2J}\right) \left(\frac{U+J}{1+J}\right)^2 \left[\frac{(1+U)(U+2J)(1+J)^2}{J^2(1+2J) + U(U+2J)(1+J)^2} \right]^1 .5 \tag{2.13}$$

- F_{ion} is a correction term to take into account the charge on the ion. This includes an unusual term $q = A_Z - N_U$ where A_Z is the atomic number and N_U is the number of electrons in suborbitals *up to* the nl orbit. q is therefore the effective charge seen by the incident electron as it penetrates the outer suborbitals of the atom to collide with the electron in the nl orbit. This is also demonstrated to be applicable for multiple positively charged ions [59]. The term includes empirical factors X and Y, where $Y = 1.27$ for s-shell, $Y = 0.542$ for p-shell, and $Y = 0.95$

for d-shell, whilst $X = 3$ for all s-, p-, and d-shells,

$$F_{\text{ion}} = 1 + X\left(\frac{q}{UA_Z}\right)^Y \tag{2.14}$$

The MBELL model is suitable for atomic number $q \leq 36$, beyond this all models are either relativistic or include ionic charge. For $q > 36$ we instead use the modified relativistic binary-encounter-Bethe model (MRBEB). This is based on the binary-encounter-dipole (BED) model which models collision as a combination of distant fast electron impact and dipole-induced collision (e.g. a nearby electron attracted towards the ion) [60]. A simplified version of this model called the binary-encounter-Bethe (BEB) model is presented in the same paper and Guerra *et al.* produced MRBEB to include relativistic effects but not ionic charge [61]. Ionic charge should be included for approximation of cross-section because the incident electron will be accelerated in the vicinity of the positive ion [55] but in work presented by Thomas and Garcia on inclusion of charge into the BEB model it is seen that the cross-sections remain order of magnitude correct even as $q \to \infty$ [62]. In absence of a more suitable alternative we approximate cross section for heavier ions where $q > 36$ using the MRBEB model. The MRBEB model is given below for a_0 the Bohr radius, α the fine structure constant, $K = \epsilon_I/m_e c^2$ is the incident electron energy scaled to the electron rest mass energy, q' and n' are the effective charge and the principle quantum number of next outermost electron respectively, and ϵ_H is the Hartree energy.

$$\begin{aligned}\sigma_{\text{MRBEB}} =& \frac{4\pi a_0^2 N_{nl}}{\left(\beta_K^2 + C\beta_L^2\right) 2L}\left[\frac{1}{2}\left(\ln\left(\frac{\beta_K^2}{1-\beta_K^2}\right) - \beta_K^2 - \ln\left(2K\right)\right)\left(1 - \frac{1}{U^2}\right) + 1\right. \\ &\left. - \frac{1}{U} - \frac{\ln U}{U+1}\frac{1+2K}{\left(1+K/2\right)^2} + \frac{K^2}{1+K/2}\frac{U-1}{2}\right] \\ \text{Where } \beta_K^2 &= 1 - \frac{1}{\left(1+K\right)^2},\ \beta_L^2 = 1 - \frac{1}{\left(1+L\right)^2} \\ \text{and } C &= \frac{2\epsilon_H}{\epsilon}\left(\frac{0.3q^2}{2n^2} + \frac{0.7q'^2}{2n'^2}\right)\end{aligned} \tag{2.15}$$

This cross sections presented here are in units of m^2 and can be used to define an ionisation rate as $W_{\text{Collision}} = n_e \sigma \langle v_e \rangle [s^{-1}]$ where $\langle v_e \rangle$ is the average electron velocity and n_e is the electron density both in SI units.

2.3 Implementation

Including ionisation in EPOCH required implementing all modes of ionisation in a way that fit into the existing PIC framework without breaking parallelism or otherwise causing unreasonable overhead. All equations listed in §2.2 ultimately provide instantaneous ionisation rates that can be calculated for each particle at each time step, and from this it is relatively quick to derive a simple statistical test that is suitable for use every time step. The ionisation rate is analogous to a radioactive decay rate insofar as $1/W$ defines a mean lifetime for a particle to remain unionised in the corresponding electric field. We approach the problem similarly; for N_0 initial particles we can write the remaining particles N as,

$$\frac{dN}{dt} = -WN \Rightarrow N(t) = N_0 \exp(-Wt) \tag{2.16}$$

From this we can infer that the ionised fraction after the time step Δt is given by $1 - \exp(-W\Delta t)$ which is the cumulative distribution function (CDF) of an exponential probability distribution with rate W. Therefore $1 - \exp(-W\Delta t)$ is the probability of a particle being ionised before time Δt. To determine whether a particle is ionised over the time step we sample the time of ionisation from the exponential distribution with rate W calculated at the particle and if this time is within the time step the particle is ionised. Whilst we cannot directly sample the exponential distribution we can follow the Monte Carlo method of inverse transformation [63] to obtain a sample of the ionisation time. If $F(x)$ is the CDF on x and F^{-1} is the inverse such that $F^{-1}(u) = \min\{x : F(x) \geq u\}$ where $u \in [0, 1]$, then the theorem governing inverse transformation sampling states that if U is a random variable uniformly distributed on $[0, 1]$ and $X = F^{-1}(U)$ then we have that X follows the CDF $F(x)$ [64].

In the case of $F(t) = 1 - \exp(-Wt)$ the inverse sample T is given by,

$$T = -\frac{1}{W}\log(1-U) \text{ where } T \sim \text{Exponential}(W) \text{ and } U \sim [0,1] \tag{2.17}$$

If the ionisation time $T \leq \Delta t$ then the particle ionises within the time step. This process is slightly modified in the code such that a uniform random number $U \sim [0,1]$ is sampled and compared to the probability from the CDF at Δt; if $U < 1 - \exp(-W\Delta t)$ the particle is ionised. This is valid since the inverse sampling test asserts that if $F^{-1}(U) \leq \Delta t$ then we ionise. Instead we ionise when $U \leq F(\Delta t)$ which is exactly equivalent since $F(t) \geq 0$, $\forall t \geq 0$. This method for using these ionisation rates is uniform, though the handling of the ionised particles varies depending on the model used, as the procedure for ensuring energy and momentum conservation varies in each case.

2.3.1 Input Deck

For heavy elements with many ionisation levels, the method of declaring each species manually in the input deck outlined in §2.1.1 becomes unnecessarily cumbersome. Once the electron species and the parent species are manually defined the mass and charge of the ionised species can be inferred. We refer to each species produced via ionisation a *subspecie* and a *child* of the *parent* species from which it is produced; the electron released during ionisation is called the *release* species. For each subspecies, whether it ionises and the ionisation energy at which it ionise both need to be manually specified. Both of these can be handled by simply specifying an array of ionisation energies on the parent; if the subspecies has an ionisation energy specified then it can be assumed to be an ionising subspecies. The ionisation module described in this chapter implements this procedure for automating subspecie definition in the input deck.

During the initial read of the input deck, properties upon which the the ionisation species will be dependent are read into arrays. This includes charge and mass but also ionisation energy, number of orbital electrons and the identity of the release species for each ionising subspecies. There is some difficulty in generating the subspecies during species generation from the input deck as it is not possible to control the order in which

the species are read. This can result in a situation where for example the parameters of the parent species are known but not the release species making it impossible to correctly generate the subspecies. To overcome this issue the essential parameters for subspecies generation are read during the first pass of the input deck before the species are set up in memory. During the second pass, these parameters can then be used to correctly set up the species in an arbitrary order.

The actual algorithm for the process of subspecies generation is as follows; at the end of the first pass for each parent species defined in the input deck a number of subspecies are created. This number is equal to the size of the ionisation energy array set in the input deck for the parent species. Each subspecie is set up with charge and mass equal to that of the parent species along with the energy at which it will ionise and the corresponding release species. During the next pass whenever a species is read in from the input deck the code tests if it is a release species for any subspecies; if it is its mass and charge are subtracted from all child species. After all the release species are read in this results in the correct charge and mass for each subspecie; to demonstrate this consider a simulation for ionising carbon where in the input deck the release species for C, C^{+}, C^{2+}, and C^{3+} has been given by electron1 and for C^{4+} and C^{5+} electron2 is used. If electron2 is read first then the charge of all the carbon subspecies will be updated as,

	C	C^{+}	C^{2+}	C^{3+}	C^{4+}	C^{5+}	C^{6+}
initial	0	0	0	0	0	0	0
C^{4+} subspecie charge update	0	0	0	0	0	$+1$	$+1$
C^{5+} subspecie charge update	0	0	0	0	0	$+1$	$+2$

Then eventually electron1 is read and the charges are updated again,

	C	C^+	C^{2+}	C^{3+}	C^{4+}	C^{5+}	C^{6+}
initial	0	0	0	0	0	+1	+2
C subspecie charge update	0	+1	+1	+1	+1	+2	+3
C^+ subspecie charge update	0	+1	+2	+2	+2	+3	+4
C^{2+} subspecie charge update	0	+1	+2	+3	+4	+4	+5
C^{3+} subspecie charge update	0	+1	+2	+3	+4	+5	+6

In addition during the first pass an algorithm for finding the principle and angular quantum numbers of the outermost electron is applied when each ionisation species is created. This assumes ground state population of atomic orbitals; 1s, 2s, 2p, 3s, 3p, 4s, 3d, 4p, 5s, 4d, etc. The algorithm is shown below where n_electrons is the total number of orbital electrons, n is the principle quantum number, and l is the angular quantum number,

```
DO WHILE(n_electrons .GT. i)
  n = n + 1
  DO l = (n-1)/2, 0, -1
    i = i + 4*l + 2
    IF(n_electrons .LE. i) EXIT
  ENDDO
ENDDO
```

For collisional ionisation an extra Boolean variable is stored for the species to identify if it is an electron. This is required to tell whether a collision will result in electron impact ionisation. Other than this there is no additional setup required for collisional ionisation. The ionisation module includes the following additional fields in the input deck,

- **CONTROL BLOCK** - Boolean fields *field_ionisation*, *use_multiphoton*, *use_bsi*. The first turns on field ionisation routines; false by default. *use_multiphoton* and *use_bsi* only take effect when field ionisation is active and are set to true by default; the tunnelling ionisation model is always used.
- **COLLISION BLOCK** - Boolean field *collisional_ionisation* to activate collisional ionisation model; false by default

- **SPECIES BLOCK** - lists *ionisation_energies* and *electron*. Ionisation energies are given in joules and must be specified to the innermost electron for the n and l to be calculated correctly. If the user wishes to only explore the first few ionisation levels it is recommended to include extremely high ionisation energies for the remaining levels; the additional species have a negligible effect on computation time. The electron must be specified as either a list naming the electron species for every ionisation level, alternatively a single electron species may be specified to act as the ejected electron at all ionisation level. Specifying electrons as a list is primarily used for tracking electrons ejected from specific energy levels, as individual species are easily viewed in the available visualisation tools for EPOCH.

2.3.2 Field Ionisation

The equations used for calculating the field ionisation rates are fairly cumbersome and involve many computational operations. To reduce the impact of this everything that can be calculated on a per-species basis is stored in arrays at the start of the simulation, rather than being calculated for each particle at each time step. The multiphoton cross-section is calculated for $K = \lfloor \epsilon/\omega + 1 \rfloor$ the threshold number of photons for ionisation; ionisation by absorption of photons above this amount is neglected. In addition to this the lasers attached to simulation boundaries are checked; if there is no laser or if there are lasers with differing frequencies then the multiphoton model is deactivated and the user is notified.

Modelling of multiphoton ionisation would ideally incorporate photon interaction but since PIC codes model the laser as an electromagnetic wave propagating across grid points we only have access to the instantaneous laser intensity at the particle. It is possible to model photons as a species in EPOCH as demonstrated in the recent extension to include the effects of quantum electrodynamics [2] but this application allowed for a hybrid modelling of the laser such that only photons relevant to the QED interactions are simulated. Modelling the laser for the purposes of multiphoton ionisation would require the electric field to be entirely modelled as photons so as to track the energies of the photons from different lasers. This would be very computationally expensive in terms of number of superparticles in the simulation, therefore in the case

of multiple lasers multiphoton ionisation is inactive and the ionisation processes are modelled as purely tunnelling. To summarise, when using multiple lasers the ionisation may be underestimated at low field intensities ($< 10^{14}$Wcm^{-2} for hydrogen but varying for other elements and orbitals) and resonance effects cannot be modelled.

It is important to note that the code does not distinguish between electrons in an orbital i.e. the magnetic quantum number is not taken into consideration, however the ADK equation given in Eq. (2.9) requires the magnetic quantum number m. However, the ADK ionisation rate tends to be much lower for $m \neq 0$ [38]. As such, the ionisation rate obtained from Eq. (2.9) is averaged over all possible values of m. It is typical to simply take $m = 0$ [65] but when there are many possible values of m we have that $W_{\text{ADK},m=0} \gg W_{\text{ADK},m\neq 0}$ and so taking $m = 0$ for all ionising electrons artificially inflates the ionisation rate. The ADK formula used for the tunnelling model in EPOCH is found by averaging over m and assuming the electron to be in the ground state such that $n_0^* = n^*$. K_n in the following equation is the modified Bessel function of the second kind,

$$\begin{aligned} W_{\text{ADK}} =& \sqrt{\frac{6}{\pi}} \frac{2^{2n^*}\epsilon}{n^*\Gamma\left(2n^*\right)} \left(\frac{2\left(2\epsilon\right)^{3/2}}{E}\right)^{2n^*-3/2} \exp\left(-\frac{2\left(2\epsilon\right)^{3/2}}{3E}\right) \\ & \times \left(\sqrt{\frac{16\left(2\epsilon\right)^{3/2}}{\pi E}} \exp\left(\frac{2\left(2\epsilon\right)^{3/2}}{E}\right) K_{l+1/2}\left(\frac{2\left(2\epsilon\right)^{3/2}}{E}\right) - 1\right) \end{aligned} \tag{2.18}$$

The field ionisation routine selects the model for the ionisation rate based on the self-consistent electric field strength at the particle. The condition for transition from multiphoton to the tunnelling regime is $\gamma \ll 1$. Investigations into the application of the Keldysh parameter [36] show that $\gamma < 0.5$ is a typical transition point giving the tunnelling transition field strength E_M as,

$$E_M = \omega\sqrt{8\epsilon} \tag{2.19}$$

The transition between tunnelling and BSI is taken to be the point at which the self-consistent electric field strength equals the atomic field strength E_T [34],

$$E_T = \frac{\epsilon^2}{4Z} = \frac{Z^3}{16n^{*4}} \tag{2.20}$$

To ensure that the ionisation rate is smoothly monotonically increasing through the model transitions it is necessary to enforce restrictions on the models because the multiphoton rate grows very quickly and the BSI transition cause a large jump in the rate. The difference between the restricted and unrestricted models can be seen in Fig. 2.2. For E_B where ${}^{dW_{\mathsf{ADK}}(E_B)}/_{dE} = 0$, a piecewise function defining the complete field ionisation model is,

$$W_{\mathsf{Field}}(E) = \begin{cases} \min\left(W_{\mathsf{Multi}}(E), W_{\mathsf{ADK}}(E_T)\right) & : E \leq E_M \\ W_{\mathsf{ADK}}(E) & : E_M < E \leq E_T \\ \min\left(W_{\mathsf{ADK}}(E), W_{\mathsf{BSI}}(E)\right) & : E_T < E \leq E_B \\ W_{\mathsf{BSI}}(E) & : E > E_B \end{cases} \tag{2.21}$$

It is possible for multiple ionisations to occur in a single timestep. To account for this the method given at the start of this section is given an additional step. The random number $U_1 \sim [0, 1]$ used for the ionisation test is kept and used for an inverse sample [63] of the cumulative distribution function in the exponential decay. This way we can sample the time by which the ionisation occurs as $t_{\mathsf{ionisation}} = -\frac{1}{W_{\mathsf{Field}}} \log(1 - U_1)$. If $t_{\mathsf{ionisation}} < \Delta t$ then it is possible for multiple ionisation to occur. The particle list is left unaffected and the species to which the particle will ionise is stored. The ionisation routine is repeated for $U_2 \sim [0, 1]$ with a test for $U_2 < 1 - \exp\left[-W\left(\Delta t - t_{\mathsf{ionisation}}\right)\right]$ after which $t_{\mathsf{ionisation}}$ is updated using U_2. This is repeated until the test for ionisation fails or $t_{\mathsf{ionisation}} > \Delta t$. At the end of this multiple ionisation cycle the particle is removed from the particle lists, an electron is added and the particle is placed in a temporary ionisation particle list for its species. This ensures that when the cycle runs for other species, the same particle is not ionised again. At the end of the ionisation routine, this temporary list is appended onto the particle lists.

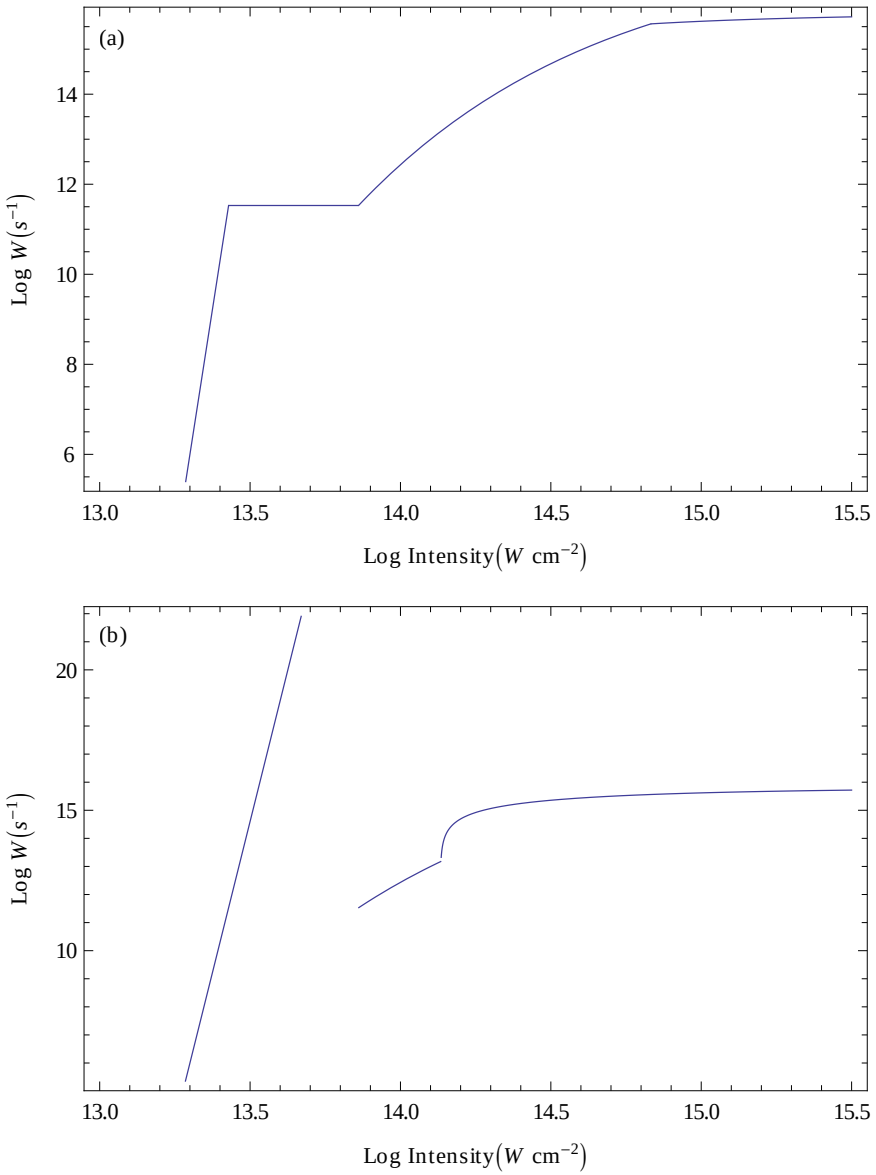

Figure 2.2: (a) Restricted and (b) unrestricted ionisation rates shown for hydrogen in the field of a 2μm laser. The restricted rate forces the ionisation rate function to be monotonic increasing across multiphoton, tunnelling and barrier suppression regimes.

In all cases of field ionisation the ion and electron are created observing momentum conservation. However the handling of the electron varies in each model; upon ionisation in the tunnelling and BSI regime the electron is released with proper conservation of momentum in the direction of the electric field. In these regimes it should be noted that the electron released through ionisation is always added to the domain at the velocity of the parent ion and the acceleration is thereafter driven by the Lorentz force in the next PIC particle push. In the multiphoton regime the additional energy absorbed by the electron at the time of ionisation is known to be $K\omega - \epsilon$ which is used to increase the kinetic energy of the electron in the direction of the electric field vector such that the momentum is increased by $-\sqrt{2m_e\left(K\omega - \epsilon\right)}\hat{\mathbf{E}}$. Though there can be many ejection angles, ejection parallel to the wavevector of the laser has the highest probability of occurrence therefore electrons are treated as always accelerating in the opposite direction of the electric field vector [34].

Work is done by the laser to ionise the particles but this is not automatically included via any mechanism in the PIC scheme. To ensure that the energy loss from the laser field due to the ionisation is accounted for we include a current density correction derived from Poynting's theorem [39] which feeds back into the Maxwell's equation during the field updates. Recall that each superparticle can be ionised multiple times over a single time step and that the energy absorbed by the superparticle during ionisation depends on the weight of the superparticle. Whether it was ionised in the multiphoton or tunnelling/BSI regime will also affect the amount of energy absorbed; for the former it will depend on the of the number of photons absorbed or and for the latter it will depend only on the ionisation energy. To implement this, at the end of each step during multiple ionisation the total energy ϵ_t is added to a variable for total work done by the laser on the particle for the time step. We calculate the current correction at the end of the ionisation routine for a particle weight N over the timestep Δt for $\mathbf{E}$ the self-consistent electric field strength at the grid point where the correction is applied. This is then weighted to the grid values for current density as,

$$\mathbf{J}_{\text{ionisation}} = \frac{N\epsilon_t}{\Delta t E}\hat{\mathbf{E}} \tag{2.22}$$

This is easily shown to correctly account for the energy loss; the change in energy is $\Delta u = -N\epsilon_t$ therefore over the timestep we have that,

$$\frac{du}{dt} = \frac{\Delta u}{\Delta t} = -\frac{N\epsilon_t}{\Delta t} \tag{2.23}$$

In the absence of energy flow in and out of the volume of ionising material, Poynting's theorem proves that Eq. (2.22) produces the energy loss required,

$$-\frac{du}{dt} = \mathbf{E}\cdot\mathbf{J} \Rightarrow -\frac{du}{dt} = \mathbf{E}\cdot\left(\frac{N\epsilon_t}{\Delta t\,|\mathbf{E}|^2}\right)\mathbf{E} = \frac{N\epsilon_t}{\Delta t} \tag{2.24}$$

2.3.3 Collisional Ionisation

The MBELL model given in Eq. (2.11) provides a total cross section for collisional ionisation based on all possible excitation-to-ionisation routes from both outer and inner shells. The field ionisation model used in this module considers only removal of the outermost electron and in general this is the most likely scenario due to lower ionisation energy. As such we make use of this same assumption and do not sum the cross section over all orbitals. The orbit specific parameters A and B_i are only available for $n < 4$ and $l < 3$, everywhere else the MRBEB model given in Eq. (2.15). A and B_i are provided in table 2.1.

nl	A	B_1	B_2	B_3	B_4	B_5	B_6	B_7
1s	0.5250	-0.5100	0.2000	0.0500	-0.0250	-0.1000	0.0000	0.0000
2s	0.5300	-0.4100	0.1500	0.1500	-0.2000	-0.1500	0.0000	0.0000
2p	0.6000	-0.4000	-0.7100	0.6550	0.4250	-0.7500	0.0000	0.0000
3s	0.1300	0.2500	-1.5000	2.4000	3.2200	-3.6670	0.0000	0.0000
3p	0.3880	-0.2000	-0.2356	0.5355	3.1500	-8.5000	5.0500	0.3700
3d	0.3500	1.6000	-3.0000	4.0000	2.0000	-5.0000	-1.5000	3.5000

Table 2.1: Empirical factors for electron orbitals used in Eq. (2.11). [66]

The collisional ionisation routine itself makes direct modifications to the EPOCH collision module presented in §2.1.4. When species are being paired for collisions, we test whether one is an ionising species and the other is an electron. If this is not the case the collision module continues without further modification, otherwise an addi-

tional subroutine *preionise* is called which is similar to the existing collision subroutine *inter_species_collisions* without the calls to the *scatter* function. In *preionise* the ion is set as the target and paired with impacting electrons then a test for ionisation is performed prior to scattering. The number of collision pairs is $P = \max(N_e, N_\mathrm{i})$ where N_e and N_i are the number of electron and ion superparticles respectively. If $N_e > N_\mathrm{i}$ then some electrons are used in multiple collisional ionisation tests. Although the electron and ion do not actually collide during the subroutine it is still necessary to calculate the electron-ion collision weight correction factor w for superparticle weights w_e and w_i [45, 67],

$$w = \frac{\sum_{N_e} w_e}{\sum_{P} \min(w_\mathrm{i}, w_e)} \tag{2.25}$$

Factor w accounts for the fact that if a superparticle collides with a superparticle of less weight then the larger superparticle should have a lower probability of collision. This is easily understood when thinking of the particles they represent; if superparticle A has a higher weight than superparticle B then there is a higher density of particle A than B in the space the two superparticles occupy. It is more likely that particles A collide with themselves than they collide with B which is an effect ignored under the superparticle scheme. The factor w suggested by Nanbu and Yonemura corrects the cross section of an electron colliding with the ion; note when the electron and ion weights are equal we have that $w = 1$ as no correction is needed [67]. The correction w required in the test for ionisation as it makes use of cross section; the test for ionisation is similar to that used in §2.3.2; for a uniform random number $U \sim [0, 1]$ ionisation proceeds if,

$$U < 1 - \exp(-n_e w \sigma v_e \Delta t) \tag{2.26}$$

Following successful ionisation the impact and release species are marked to be ionised, the ionising electrons are also marked. At the end of the routine, particles to be ionised are split and the ions are added to the relevant lists. The ionising impact electron and the ionised target electron are separated into new lists and returned from the

preionise routine where they are scattered off of each other separately. If ionisation does not occur the electron and ion are unaffected in their particle lists and are subsequently scattered under the usual collision routine. In calculating the rate from the cross section we use the velocity of the incident electron v_e instead of the average electron velocity since we perform the ionisations on a per-particle basis.

Following an ionisation event, the ionisation energy for the target is accounted for via a reduction of the incident electron kinetic energy. It is important to note that this energy loss is not equivalent to the ionisation energy as relativistic effects must be considered. The incident electron kinetic energy is reduced by the ionisation energy ϵ in the rest frame of the target ion before being transformed back into the simulation frame to find the final kinetic energy. Since the electron energy will be the same in any rotated frame of reference we first simplify the Lorentz transformation by rotating the simulation frame such that the ion motion is in the x-axis. Consider such an ion rest frame so that it has axes rotated by θ in the y-plane and ϕ in the z-plane with respect to the simulation frame. For ion momentum $\mathbf{p}_\mathsf{i}$ in the simulation frame we find the rotations as,

$$\theta = \arctan\left(\frac{p_\mathsf{i}^{(z)}}{p_\mathsf{i}^{(x)}}\right) \qquad \phi = \arctan\left(-\frac{p_\mathsf{i}^{(y)}}{p_\mathsf{i}^{(x)}\cos\theta + p_\mathsf{i}^{(z)}\sin\theta}\right) \tag{2.27}$$

The Lorentz transformations for the electron energy and momentum then become simply $E'_e = \gamma_\mathsf{i}\left(E_e - \beta_\mathsf{i} p_e^{(x)} c\right)$ and $p_e'^{(x)} = \gamma_i\left(p_e^{(x)} - \beta_i E_e/c\right)$ respectively, where E'_e and E_e are the electron energies in the rotated ion rest frame and the rotated simulation frame respectively. As the ion motion is in the x-axis we have that $p_e'^{(y)} = p_e^{(y)}$ and $p_e'^{(z)} = p_e^{(z)}$. When an ionisation occurs, the momentum reduction is calculated in the ion rest frame by subtracting ϵ from the kinetic energy as shown in Eq. (2.28), and the inverse Lorentz transformation $p_e^{(x)} = \gamma_i\left(p_e'^{(x)} + \beta_i E'_e/c\right)$ is applied before the rotation is reversed.

$$\mathbf{p}_e^{\mathsf{ionised}} = \left[\left(\frac{E^{\mathsf{unionised}} - \epsilon}{c}\right)^2 - m_e c^2\right]^{1/2} \hat{\mathbf{p}}^{\mathsf{unionised}} \tag{2.28}$$

In the event that the target ion is stationary Eq. (2.28) still applies, though no rotations or transformations are used. Additionally due to the method of rotation employing arctangents $\pi/2$ rotations must be caught and handled manually.

2.4 Discussion

EPOCH is an highly extensible particle-in-cell code with a pre-existing module for collisions making it well suited for including ionisation dynamics. The different modes of field ionisation are presented and a method for differentiating between regimes based on laser field strength at the particle is described. The inclusion of proper ionisation statistics in PIC is shown to require only an ionisation rate, leaving the potential for easily changing the ionisation models used. Whilst multiphoton, tunnelling and barrier suppression models can be used at once any model can be excluded at runtime through the text based input deck. The multiphoton ionisation rate functions for monochromatic laser input but in future it may be possible to allow for multiple lasers of differing frequencies or even no lasers at all by modelling photons in the simulation. Photons are already included in EPOCH through the quantum electrodynamics model [45], though on the scale required for proper modelling of multiphoton ionisation this may prove too computationally expensive. Collisional ionisation is included via electron impact ionisation models, whilst recombination effects are neglected. Future releases of the ionisation module may benefit from inclusion of three-body recombination which can be demonstrated to be significant even on picosecond timescales [50].

Chapter 3

Validating the Ionisation Module

The procedure for verifying the Monte Carlo scheme used by our ionisation model was first to demonstrate it is capable of correctly reproducing the ionisation rates found using the multiphoton, tunnelling and barrier-suppression ionisation models in §2.2. Verifying the collisional ionisation scheme proceeds somewhat differently; due to the difficulty in predicting the rate of cascading ionisation as more electrons enter the system we opt instead for reproducing published results for average charge state over time. An early iteration of the ionisation scheme is also described which is capable of resolving very small amounts of ionisation for an arbitrarily low number of superparticles. Whilst this scheme reproduces the ionisation rate to a higher resolution it is shown that the ionisation scheme laid out in §2.3 converges to the same result in less computational time. Following this the module was used to demonstrate the three major mechanisms of ionisation in laser-plasma interaction. The first is ionisation-induced defocussing of a laser in neutral gas; a well understood physical phenomena for which ionisation is directly responsible. The second is fast shuttering in laser-solid interaction; the rapid formation of a critical surface which is an effect utilised by plasma mirrors to steepen a laser pulse profile. Finally the module was used to simulate ionisation injection, a consequence of tightly bound ionisation states being ionised selectively in areas of high electric field strength. This has applications in electron acceleration by enhancing the output achieved in laser wakefield acceleration. The results from laser wakefield acceleration and a description of the partial superparticle ionisation model are in preparation for publication in the Journal of Computational Physics [45].

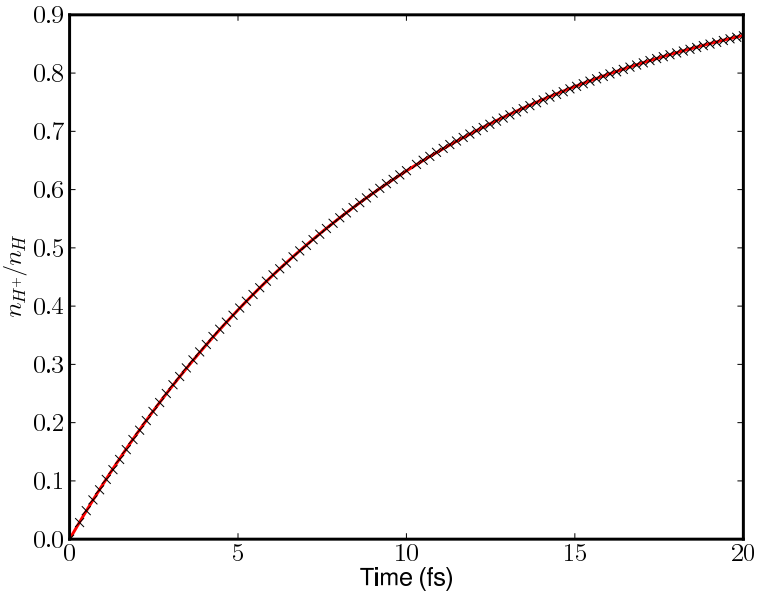

Figure 3.1: Simulations of neutral hydrogen in 1D over a $2\mu m$ domain with 64 grid points and 512 particles per cell. The ionisation rate is arbitrarily fixed to 10^{14}s^{-1} in both field ionisation only and collisional ionisation only cases. In the latter, the density of free electrons and number of electron superparticles are set equal to that of the neutral hydrogen. The ionisation rate W was recovered by fitting $1 - \exp(-Wt)$ in Gnuplot to data for $n_{H^+}/n_{H_{\text{initial}}}$ averaged over three runs, resulting in $W = 9.99 \times 10^{13}\text{s}^{-1}$ in both cases.

3.1 Ionisation Statistics and Scaling

The ionisation schemes for both collisional and field ionisation models consists of two distinct parts; the physical model which provides the ionisation rate and the statistical model which consists of an inverse sampling of an exponential decay using this rate as described in §2.3.2. As a test of the statistics in isolation, the rate was manually set to a constant in the code in 1D such that the total fraction of ionised hydrogen within the domain could be directly modelled as $1 - \exp(-W_0 t)$ where $W_0 = 10^{14}\text{s}^{-1}$ is the constant ionisation rate. This was performed separately for both field and collisional components; note in the latter case that since the rate is set to a constant there should be no increase in ionisation due to additional electrons added to the system. Fig. 3.1 shows that the expected ionisation rate is recovered in both cases.

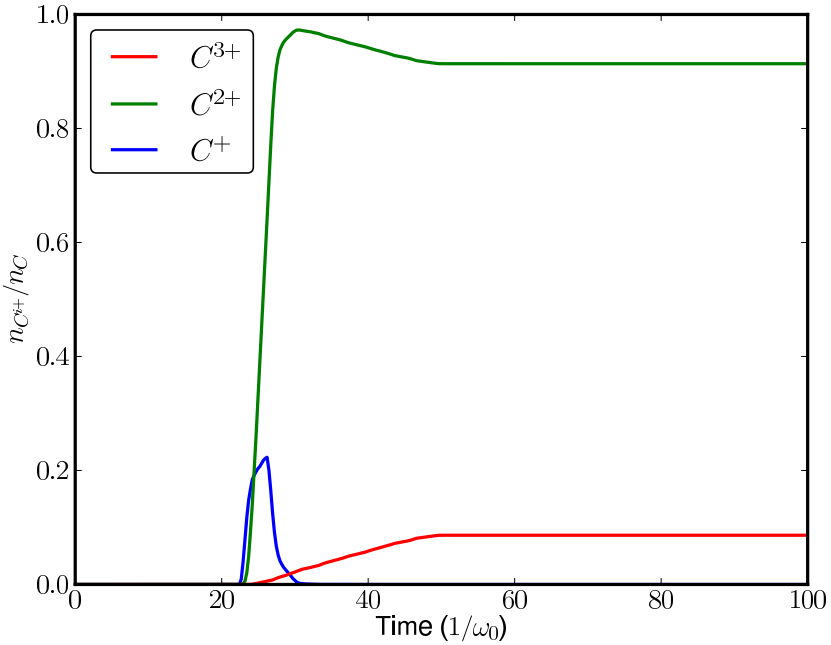

Figure 3.2: Reproduction of the simulation presented by R. Nuter *et al.* to demonstrate multiple ionisation [65] (see Fig. 2); a linearly polarised electromagnetic plane wave of intensity 3×10^{15}Wcm^{-2} and wavelength $\lambda = 800$nm propagates into a square domain of side $48c/\omega_0$ with a pin of neutral carbon at 0.1% critical density in the centre in a square of side $2c/\omega_0$. The grid used was 128×128 with 512 particles per cell in the pin, and the simulation is allowed to run for $100/\omega_0$.

The field and collisional ionisation statistics behave identically for hydrogen. However it is important to note that the field ionisation component of the ionisation module includes a scheme for multiple ionisation, whereas the collisional ionisation scheme limits to a single ionisation event per collision. Recently R. Nuter *et al.* [65] presented a field ionisation module with multiple ionisation using ADK for tunnelling in the PIC code Calder [68]. In this paper they demonstrate their module to correctly model the laser acceleration of ionising carbon atoms measured at the UHI10 Saclay facility; they also provide a simulation with detailed results for an electromagnetic plane wave passing through a carbon gas in 2D. For comparison, the simulation is repeated using EPOCH with ionisation in Fig. 3.2 and is demonstrated to give good agreement with the results presented by R. Nuter *et al.* for multiple ionisation.

If the expected ionisation over the timestep $N_a\left(1-\exp\left(-W\Delta t\right)\right) < M$ where M is the average superparticle weight and N_a is the number of particles represented in the simulation, a single ionisation causes relatively large spikes in the ionising electron density with respect to the expected ionisation. We can rewrite this as $1-\exp\left(-W\Delta t\right) < 1/N$, so the accuracy to which W is resolved under this model should depend on the number of superparticles in the simulation N. It is expected that this relationship will go with $\mathcal{O}\left(1/\sqrt{N}\right)$ as with other particle properties in PIC. To confirm this, the simulations from Fig. 3.1 were repeated varying the number of superparticles and the size of the time step. Having demonstrated that the statistical model behaves identically in field and collisional ionisation for a single ionisation level we expect that the scaling will be the same, as such the plasma is chosen to be underdense such that it can be modelled as collision-free allowing collisional ionisation to be neglected.

It is found that the accuracy of the ionisation rate scales as expected with number of superparticles as shown in Fig. 3.3. However it is also found that the accuracy of W was independent of the size of the time step. This is something of a counter-intuitive result but makes sense when considering that this test uses a constant ionisation rate meaning that the decayed fraction $1-\exp\left(-W\Delta t\right)$ is exact regardless of timestep size. This is easily demonstrated if we consider the ionised fraction when halving the timestep size; the remaining unionised particles after $\Delta t/2$ is $\exp\left(-W\Delta t/2\right)$ so after another half time step the ionised fraction is,

$$1-\exp\left(-W\frac{\Delta t}{2}\right)+\exp\left(-W\frac{\Delta t}{2}\right)\left(1-\exp\left(-W\frac{\Delta t}{2}\right)\right)=1-\exp\left(-W\Delta t\right) \quad (3.1)$$

Whilst there is no dependence of the ionisation statistics upon time there is still error in the calculated rate W which will depend on the ionisation model used. In a time varying electric field the accuracy to which the field is resolved under the finite differencing scheme goes as $\mathcal{O}\left(\Delta t^2\right)$. The scaling with electric field strength for multiphoton, tunnelling and barrier suppression is E^{2K}, $\exp\left(-1/E\right)$ and $1/E$ respectively. Considering error propagation on these scalings gives that the ionisation rate will also scale as $\mathcal{O}\left(\Delta t^2\right)$.

Where this statistical scheme fails is when a constant ionisation rate over a

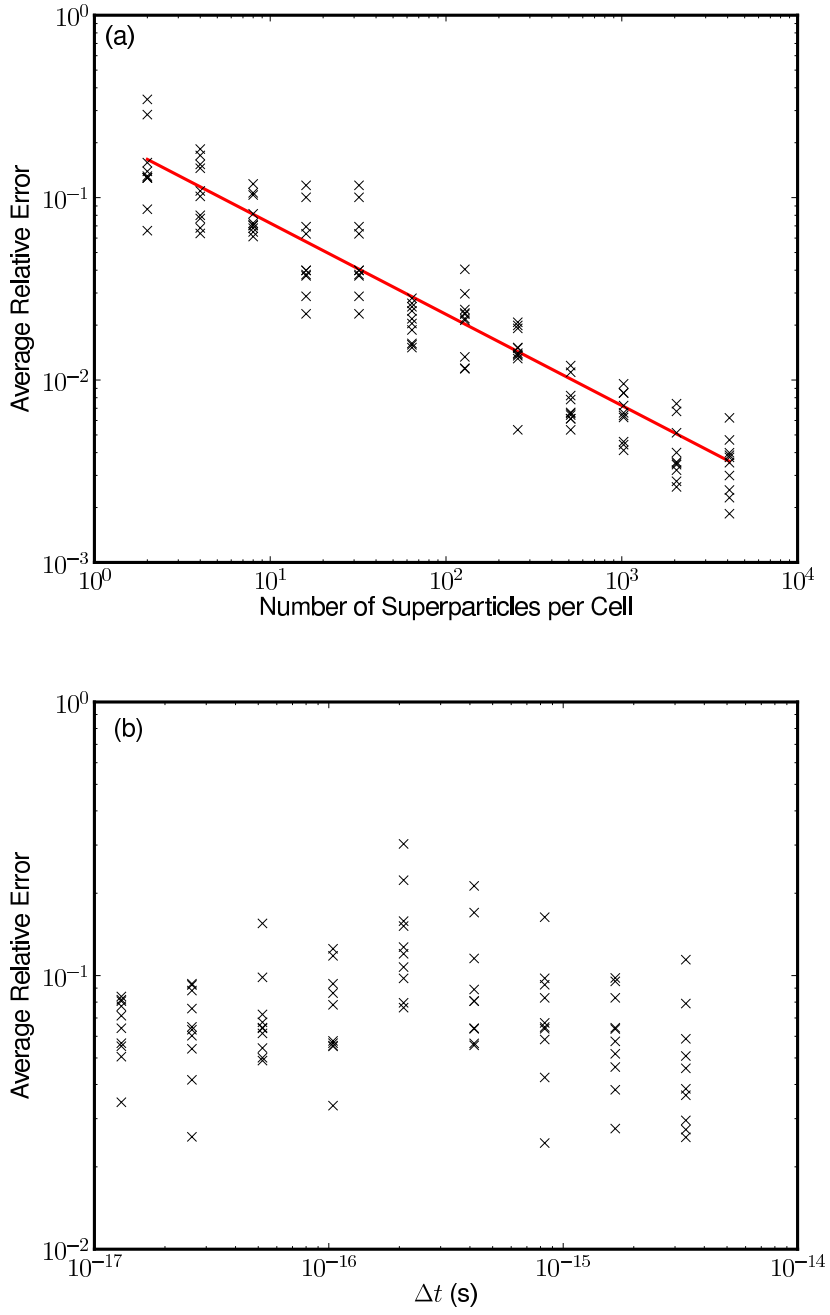

Figure 3.3: 1D simulations as described in Fig. 3.1. The domain is split over 16 cells and the (a) number of superparticles per cell and (b) time step size were varied. The average relative error from the expected ionisation state of the hydrogen was calculated for several runs. For the constant ionisation rate it is found that the average relative error scales as $0.23/\sqrt{N}$ but has no dependence on the size of the time step.

timestep is not a good approximation, as then the exponential decay does not apply. This incidentally coincides with a failure in the ionisation models themselves, as all three ionisation models all assume an instantaneously static value for the electric field. In EPOCH this is generally a reasonable assumption; from Eq. (1.68) we see that for a laser pulse propagating through the Yee grid stability requires that $\epsilon = \sin(\omega^{\Delta t}/_2) < 1$ from which we find $\omega < \pi/\Delta t$. Therefore there is a timestep at least every half-cycle of the laser; typically more than this is used and the timestep can also be manually reduced using the input deck.

3.1.1 Partial Superparticle Ionisation

The ionisation scheme outlined in §2.3 went through an initial inception in which the probability of ionisation was directly dependent upon superparticle weight M. In this scheme the ionisation rate was calculated for every particle over each time step using the rate equations from §2.2 as before but ionisation occurs when the particle is over half-ionised. This introduced an unphysical dependence between the weight of the superparticle and the ionisation rate which was alleviated by allowing the superparticle to partially ionise producing an ion and an electron whilst lowering the weight of the original ionising superparticle. As a consequence of the method used it was possible to model very small amounts of ionisation.

Whilst this partial superparticle ionisation scheme was ultimately rejected due to the intense computation requirements, it is presented here for comparison and as a means of reproducing the ionisation rate to a very high resolution for an arbitrarily small number of superparticles. It is also demonstrated that given sufficient simulation time it is possible to recover the ionisation rate under the whole superparticle ionisation scheme described in §2.3 using an equally small number of superparticles. Under the partial superparticle ionisation scheme the particle ionises after k timesteps for $M_{i,0}$ the unionised particle weight at timestep i,

$$\sum_{i=1}^{k} M_{i,0}\left(1 - \exp\left(-W_{i,0}\Delta t_i\right)\right) \geq M_{0,0}/2 \tag{3.2}$$

The choice of ionising when the particle weight falls to $M_{0,0}/2$ is based on the

observation that this is the point at which the cumulative distribution function for the exponential decay will be $> 1/2$. In other words, it would be more likely to find the superparticle in the fully ionised state than in the neutral state. Multiple ionisation is handled by storing an array containing the ionised weights for each ionisation level j,

$$M_{k,j} = \sum_{i=1}^{k} M_{i,j-1} \left(1 - \exp\left(-W_{i,j-1}\Delta t_i\right)\right) \tag{3.3}$$

In effect the ionisation events are contained within the superparticle which makes each superparticle its own self-contained partially ionised plasma. There are no internal dynamics to the superparticle other than the ionisation state therefore the net charge is unchanged by ionisation events. Under this scheme ionisation may not be observed if M is very large compared to the ionisation rate. For instance if there was one superparticle of weight 100 in the simulation and the ionisation rate was 1 every time step we'd need 50 time steps to observe any ionisation. If the simulation ran for only 10 time steps the results would show no ionisation, even though we should see 10% ionisation which could be significant to the physics being observed. As a solution we define a $M^{(S)}$ the minimum superparticle weight such that when $M_{i,j} \geq M^{(S)}$ superparticles of the ionised and electron species of weight $M_{i,j}$ are added at the same position as the parent particle and $M_{i+1,j}$ is set to zero. $M^{(S)}$ must be defined by the user since if it is very small the simulation can easily flood the memory with superparticles. The selection of a suitable $M^{(S)}$ should be based upon how much ionisation is expected and the memory available. Setting $M^{(S)}$ is achieved by specifying a maximum number of superparticles for each species. The partial superparticle ionisation algorithm is described in full in Fig. 3.4 and illustrated in Fig. 3.5.

This scheme exhibits the correct ionisation statistics as demonstrated in Fig. 3.6 and allows for capturing very small amounts of ionisation that would otherwise require a greater number of superparticles to observe. This is to say that ionisation events when $1 - \exp\left(-W\Delta t\right) < 1/N$ can still be analysed. This comes at the cost of using more memory per superparticle due to requiring as many additional double floating point numbers per superparticle as there are ionisation levels for the species. This can double the memory requirement for the simulation in 2D with as little as 8 ionisation levels.

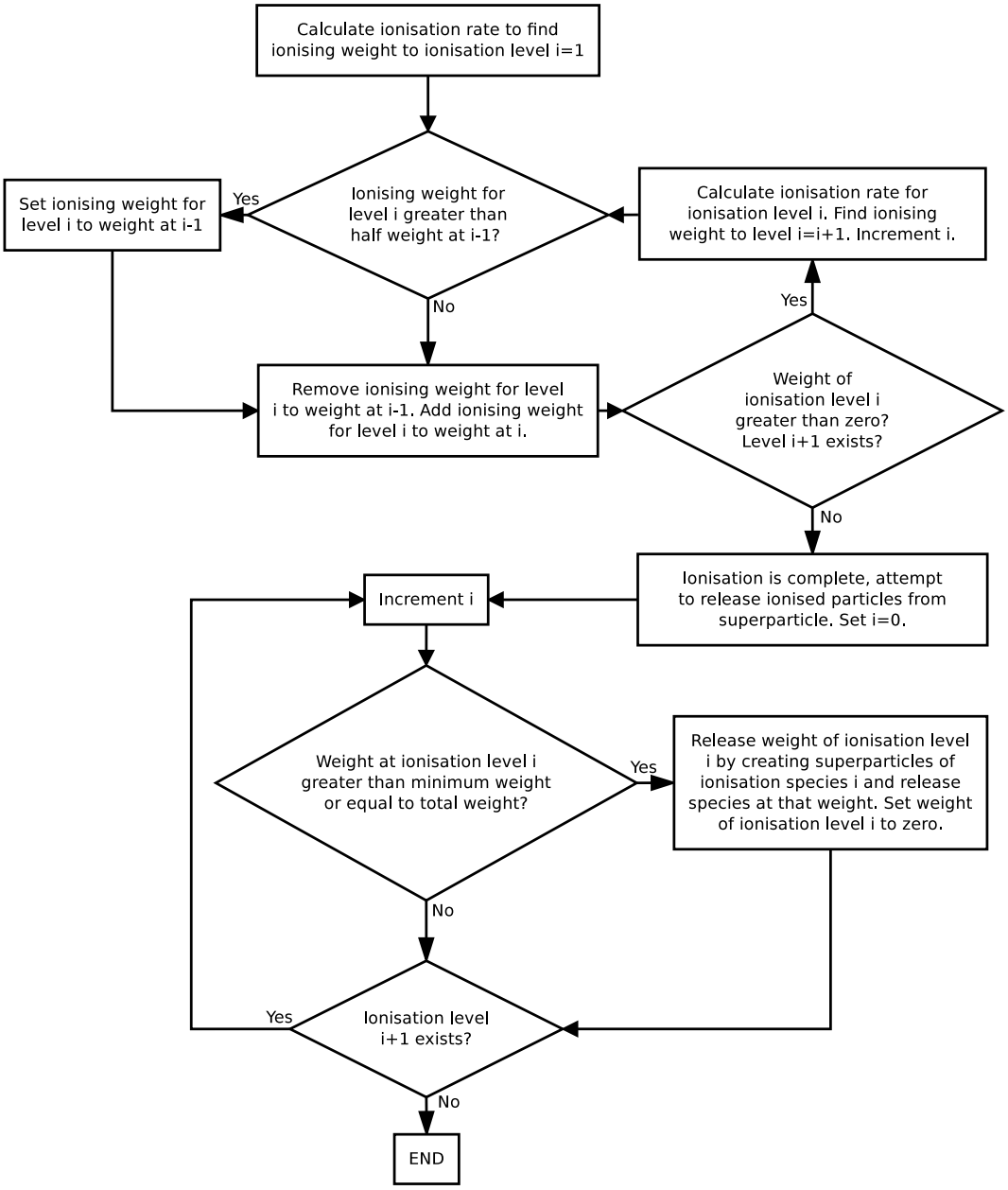

Figure 3.4: Flowchart for the partial superparticle ionisation scheme.

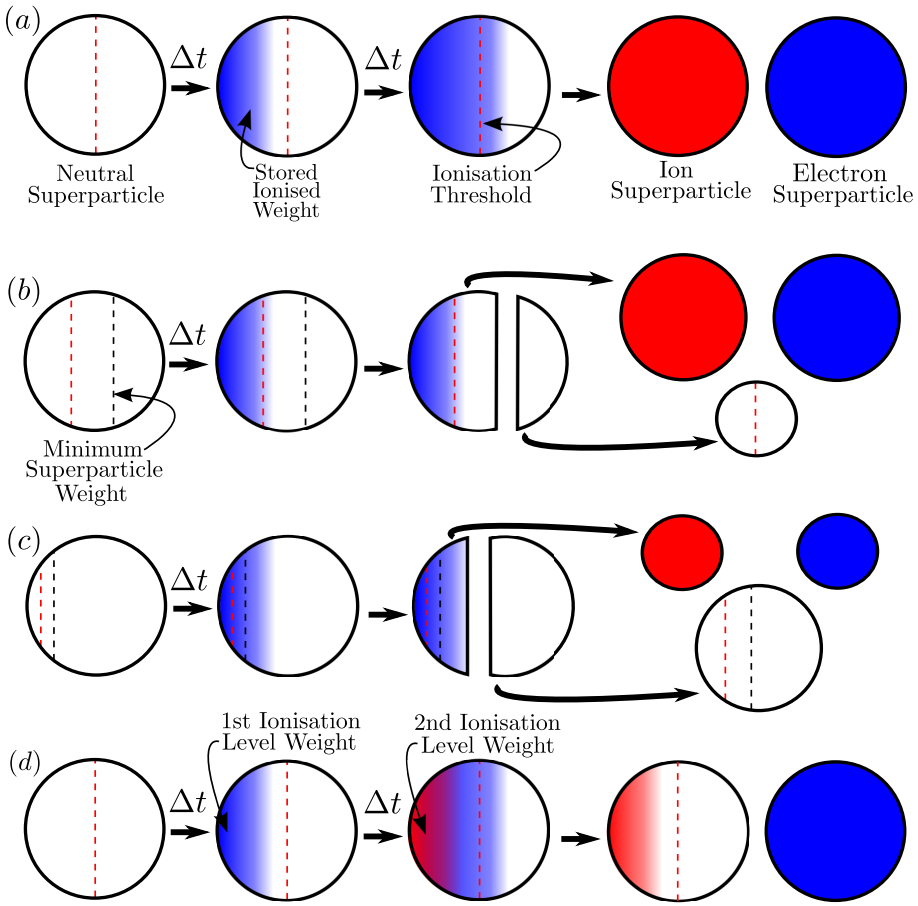

Figure 3.5: Illustration of how and when superparticles ionise under the partial ionisation scheme; (a) when the amount of ionisation is lower than the threshold it is stored in the superparticle. (b) When a minimum superparticle weight is defined the ionisation threshold is set to half of this. When this threshold is exceeded ionisation is performed up to the minimum weight and the weight of the neutral superparticle is reduced. (c) If the stored weight exceeds the minimum weight, the stored weight of ionisation products are released instead. (d) If a higher ionisation level of the neutral particle has weight, then pass this on to the ion produced.

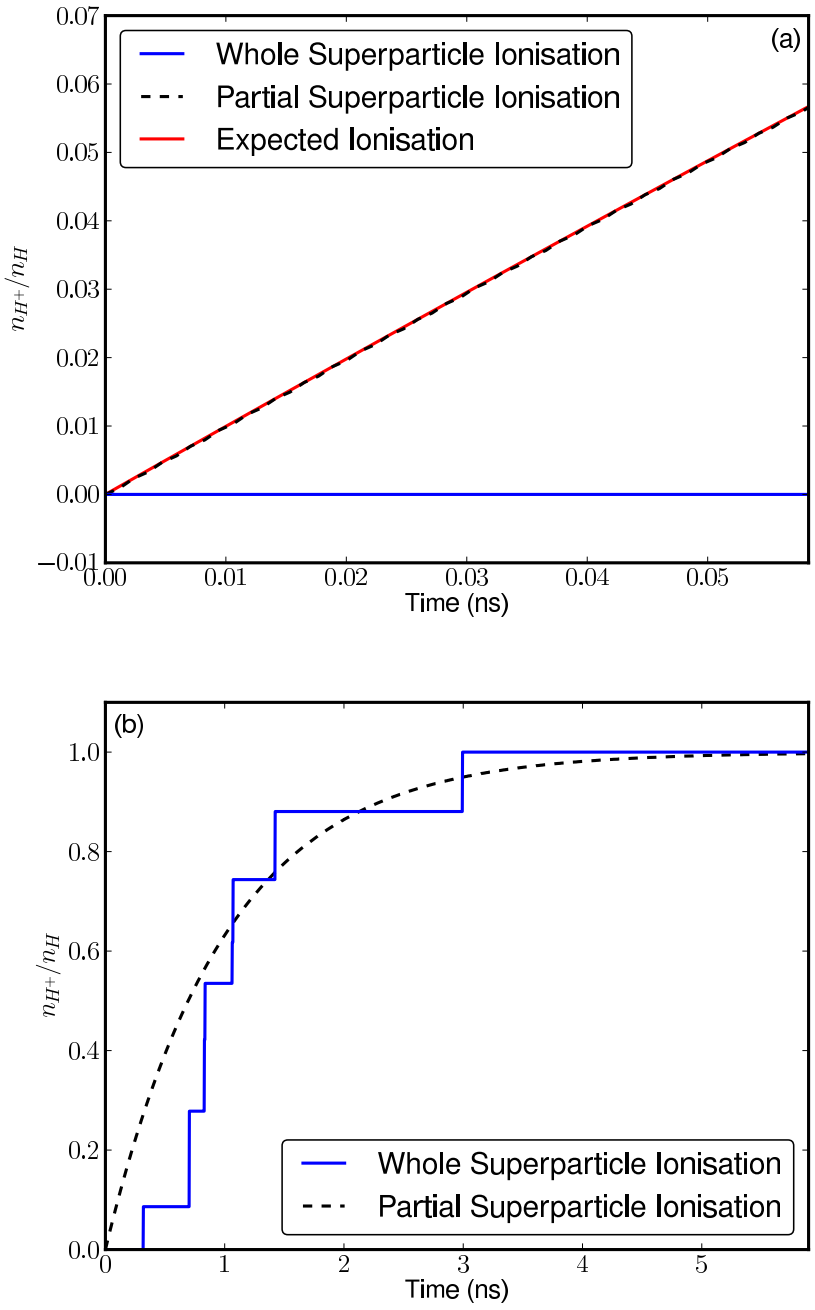

Figure 3.6: 2D simulations of neutral hydrogen ionising at a fixed rate of 1×10^{12}Wcm^2 with 10 superparticles on a 4 grid using the two different ionisation schemes outlined in §2.3 and §3.1.1. The partial superparticle ionisation scheme enforces a maximum 10,000 superparticles per species. (a) The partial superparticle ionisation scheme correctly reproduces the ionisation rate even when $1 - \exp(-W\Delta t) < 1/N$, but (b) it can be shown that under the whole superparticle ionisation scheme the correct ionisation rate can still be recovered over enough timesteps.

It also increases the computational expense of moving superparticles across processors, since extra data must be sent between the processors which in general is an expensive operation. To mitigate this the array containing the ionisation states is not allocated in memory until an ionisation event occurs; this can significantly reduce the memory requirement for simulations where ionisation is not expected to be witnessed across the entire domain.

It is worth noting that in EPOCH the amount of data passed between processors per superparticle is a constant that is independent of the species of the superparticle. Due to the fact that the size of the array of ionised weights differs depending on the species of the superparticle the message passing routines between the processors are modified to cope with a variable amount of data per superparticle. This is a simple matter of testing if the ionised weight array is allocated and adding the length of it onto the message; this does not have a significant impact on the overhead associated with message passing as the greatest overhead is almost always the interprocessor communication. Whilst use of the whole superparticle ionisation scheme in §2.3 shows poor resolution when $1 - \exp(-W\Delta t) < 1/N$ if viewed over n timesteps such that $1 - \exp(-Wn\Delta t) > 1/N$ then W is still correctly recovered. The partial superparticle ionisation scheme is best used for simulations where a low amount of ionisation is expected or if the region where ionisation occurs is small compared to the simulation domain; in this situation the computational cost can be significantly reduced.

3.2 Collisional Ionisation

Collisional ionisation statistics are not as straightforward to verify as those for field ionisation. At the densities used for testing field ionisation the energy reduction via current correction outlined in §2.3.2 is relatively negligible and would not affect the fitting of a constant rate exponential decay to the ion density shown in Fig. 3.1. However at the densities in which collisions become significant the energy reduction from the laser can become more noticeable. In addition the electron impact ionisation rate is proportional to the available electron density which increases with successive ionisation events, therefore the ionisation rate increases in time. Instead of attempting to fit an

expected ionisation rate, we compare our results to comparable results from a collisional Fokker-Planck code presented by Town *et al.* [50] who make use of BED ionisation cross section modelling.

In [50] 1D simulations are presented for a solid carbon target at initial densities between $4 \times 10^{28} - 3 \times 10^{29}\text{m}^{-3}$ with an incident 10^{16}Wcm^2, 350fs, $\lambda = 0.25\mu$m laser pulse. The carbon ions are chosen to be once ionised, and their density is chosen to provide a neutralising background to the electrons. Instead of using an incident laser for ionisation we also use the initial electron density and temperature distribution given by Fig. 2(a) and Fig. 5(a) in [50]; these are included as simple piecewise linear approximations for T_e the electron temperature in eV, ρ both the electron and C^+ density in m^{-3} and x the position in μm,

$$\rho(x) = \begin{cases} 0 & : \quad x \leq 0.2 \\ \rho_{\text{max}}(520x - 100) & : \quad 0.2 < x < 0.25 \\ 30\rho_{\text{max}} & : \quad 0.25 \leq x < 0.7 \\ 0 & : \quad 0.7 \leq x \end{cases} \tag{3.4}$$

$$T_e(x) = \begin{cases} T_{\text{min}} & : \quad x \leq 0.2 \\ (T_{\text{max}} - T_{\text{min}})\frac{0.5-x}{0.3} + T_{\text{min}} & : \quad 0.2 < x < 0.5 \\ T_{\text{min}} & : \quad 0.5 \leq x \end{cases}$$

In the above $\rho_{\text{max}} = 10^{28}\text{m}^{-3}$, $T_{\text{min}} = 15$eV and $T_{\text{max}} = 600$eV. It is noted that it is assumed the carbon ions undergo negligible acceleration compared to the electrons during the field ionisation and so the ion temperature therefore remains at a constant $T_C = 15$eV. In this way we are able to produce the average charge profile shown in Fig. 3.7 over the correct timescale as that given for collisional ionisation in Fig. 7 of [50]. Note that the much faster rise to the fourth ionisation state is simply a result of more frequent sampling; in Fig. 7 of [50] we can see that the point at which $Z = 4$ is their first data point.

The result shown in Fig. 3.7 neglects recombination and this has the affect of causing an initially very high ionisation rate; this is found to be in good agreement with the results found by Town *et al.* for collisional ionisation in the absence of recombination [50]. In [50] the laser that illuminates the target is similar in intensity to that presented

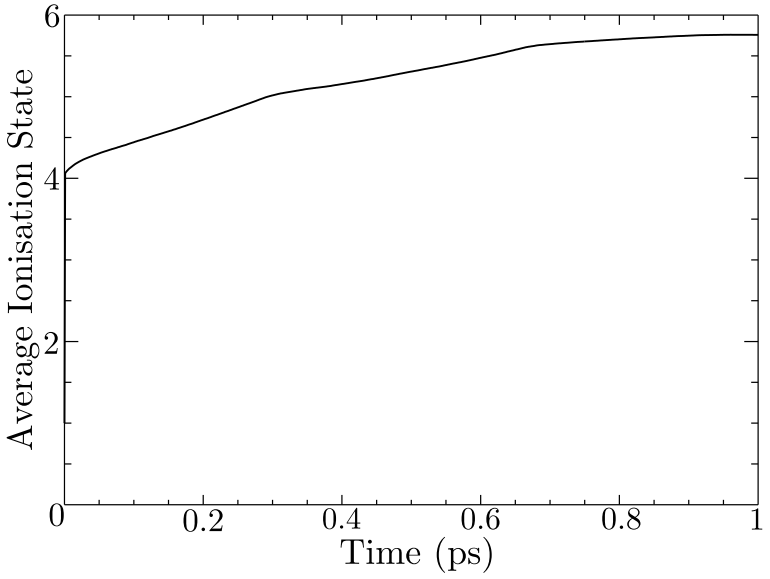

Figure 3.7: 1D simulation of collisional ionisation of C^+ based on assumed initial electron temperature and density profiles over a 1.5μm domain as given by [50]. The domain is split into 256 grid points with carbon ions at $T = 15$eV and initial density matching the electrons. Simulated with 2000 particles per species per cell for $0.25 < x\,(\mu\text{m}) < 0.7$ over 1ps. Average ionisation state is taken from 30 cells around the outermost cell.

in Fig. 3.2 where we can see that the ionisation state will reach at most C^{3+}. In Fig. 3.7 we can see that the collisional ionisation quickly rises and stops at C^{4+} on a shorter timescale than the laser field ionises, so for a simulation where this incident laser is simulated we would find that the initial field ionisation would be overestimated. We can expect that in simulations using collisional ionisation for laser-plasma interactions with carbon, that the field ionisation will be correctly predicted in cases where the electrons do not gain sufficient energy to cause ionisation before the laser field ionises the carbon up to C^{4+}.

Solutions for collisional ionisation with and without recombination eventually converge as demonstrated in the results of Town *et al.* [50], therefore after the average ionisation state rises to at least C^{4+} the modelling of field and collisional ionisation will be correct. In this case we can see that even in the absence of recombination,the inclusion of collisional ionisation still provides useful results despite causing overestimation of field ionisation. Considering the peak laser intensity in Eq. (2.21) we find that only $\sim 10^{-14}\%$ of C^{4+} will have ionised to C^{5+} during the laser pulse. In reality this figure will be even

smaller as the laser intensity will have a temporal profile, and so ionisation from C^{4+} to C^{5+} is negligible. To witness C^{4+} to C^{5+} field ionisation for the laser pulse used in [50] we would need a laser intensity of $\sim 10^{18}$Wcm^2. However Fig. 3.7 demonstrates that it is incorrect to assume that ionisation stops at C^{4+}. If the simulation runs for long enough then even a 10^{16}Wcm^2 laser will heat the electrons to ~ 400eV [50] which is enough to cause collisional ionisation of C^{4+}. Whether this is significant depends on the time-scale of the simulation; the same can also be said for the overestimation of field ionisation. If both are significant then a possible solution would be to obtain initial conditions for analysing the collisional ionisation by performing the simulation with field ionisation only for the laser pulse which would effective eliminate the initial excessive collisional ionisation.

3.3 Ionisation-Induced Defocussing

Ionisation-induced defocussing is a phenomena for which semi-quantitative estimates are available [69, 6] making it a desirable test case for the ionisation module. To discuss ionisation-induced defocussing it is useful to first consider the competing and more commonly known effect of self-focussing. It is well understood that lasers travelling through plasmas are self-focussing; this is due to the effect of electron density on the refractive index. For laser frequency ω, plasma frequency $\omega_p = \left(n_e e^2/m_0\epsilon_0\right)^{1/2}$ and critical density of the laser n_c the plasma refractive index is given by [69],

$$\nu = \sqrt{1 - \frac{\omega^2}{\omega_p^2}} = \sqrt{1 - \frac{n_e}{n_c}} \tag{3.5}$$

A laser propagating through a plasma will drive electrons out of the core of the laser into the less intense fringes via the ponderomotive force introduced in §1.2. From Eq. (3.5) we can see that the refractive index will therefore be greater in the core of the laser than in the fringes which effectively forms a focussing lens for the oncoming beam [69]. A laser with a typical Gaussian spatial profile propagating through a neutral gas will cause a higher ionisation rate at the core of the spot. So in much the same way a laser travelling through a neutral gas will increase the electron density most strongly

in the core which instead decreases the refractive index relative to the fringes and forms a defocussing lens. Ionisation-induced defocussing occurs alongside divergence of the Gaussian laser beam; the latter is given by $\theta_G = {}^{\lambda}/_{\pi\omega_0}$ [49]. By considering the propagation of a ray in the ionising medium a scaling law for the beam divergence due to ionisation-induced defocussing can be found [70]. This is given in Eq. (3.6) for z the position relative to the beam waist and $n_e(z,r)$ the electron density in cylindrical coordinates. σ_S is the Gaussian laser spot size which is the beam diameter measured where intensity in the fringes drop to ${}^{1}/_{e^2}$ peak intensity; all the relevant divergence parameters are illustrated in Fig. 3.8.

$$\theta_I \sim \frac{1}{\sigma_S} \int \frac{n_e(z,0)}{n_c} dz \tag{3.6}$$

3.3.1 Simulation and Analysis

To demonstrate ionisation-induced defocussing a set of simulations were performed to reproduce the scaling of divergence with electron density in Eq. (3.6). The domain is square with side set to $4z_R$ to ensure the fringes of the beam are not lost at the boundaries. 32 particles per cell and approximately 16 cells per wavelength are used for the domain resulting in a 256×256 grid. The domain is uniformly filled with neutral hydrogen at densities approaching n_c from 0% in 5% increments. The laser and the pulse are chosen to have $\lambda = 1\mu m$, a Gaussian spot size of $\sigma_S = 2.35$ (corresponding to an FWHM of 2μm), and $I = 10^{14}$Wcm^{-2}. The simulations run until the head of the pulse reaches the back of the domain; fig. 3.8(a) show traces of where the intensity falls to ${}^{1}/_{e^2}$ the intensity at the centre (i.e. peak at z) of the beam. This demonstrates the propagation of the laser and the increasing divergence with the axial electron density. To observe the scaling and confirm that it matches that given by Eq. (3.6) the beam divergence is measured at $z = 2z_R$ at the end of the simulation and $\int \frac{n_e(z,0)}{n_c} dz$ is found by numerical integration. Fitting the results shown in Fig. 3.8 gives a good prediction of the initial Gaussian laser spot size as $\sigma_S = 2.4\mu$m.

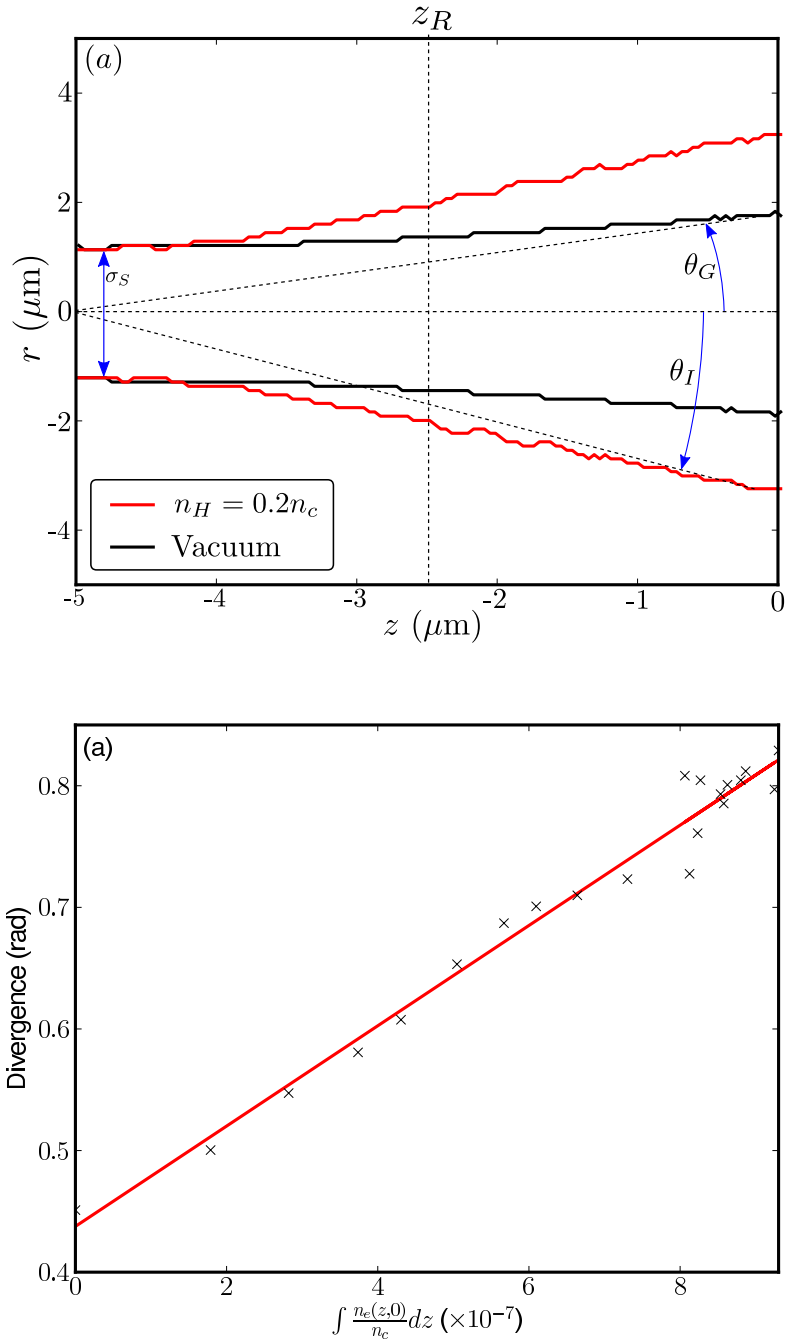

Figure 3.8: A Gaussian beam defocusses in ionising gas; (a) illustrates the impact of ionisation-induced defocussing via overlaid traces of the waists (i.e. at $1/e^2$ peak intensity) of Gaussian beams propagating through neutral hydrogen and a vacuum; the various parameters used in the fitting are also show. (b) Shows measurements of the beam divergence demonstrating the linear scaling shown in Eq. (3.6).

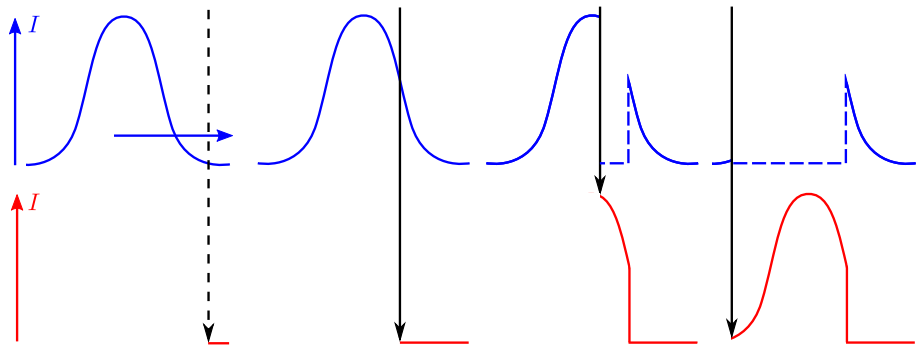

Figure 3.9: Illustration of how the reflected laser intensity profile from a plasma mirror is sharpened. Black line indicates position of the mirror, dotted when neutral and solid when ionised plasma above critical density. Blue line shows the incident laser profile; note that to the right of the mirror this line shows what is transmitted. When mirror forms we see part of the incident pulse has propagated through the mirror first. Red line shows the reflected intensity as the pulse propagates into the mirror; note the sharpened edge will be the leading edge upon reflection.

3.4 Fast Shuttering in Plasma Mirrors

In ICF the production of preplasma will reduce the amount of laser energy reaching the target [31]. For this reason it is preferable for a laser to have a short rise time and no prepulse. It is experimentally impossible to produce a real square-fronted laser pulse as the Fourier transform of a square fronted wave spans over an infinite range of frequencies. The frequencies of operation for a laser are determined by their *gain medium*; this is the material that is pumped with energy and subsequently emits photons. The range of frequencies over which these photons are emitted is called the *bandwidth* and this is inevitably a finite range. A large bandwidth laser may produce a very sharply fronted pulse but there will always be a small rise time. It is also possible to improve the laser profile through use of a plasma mirror. These are materials at solid density chosen such that no ionisation will occur for the majority of the rise time, but near the peak laser intensity ionisation occurs forming an overdense plasma which then reflects the laser pulse, this is illustrated in Fig. 3.9.

The time between initial ionisation and formation of an overcritical plasma depends on the ionisation regime and the intensity of the incident pulse. In the tunnelling regime where the ionisation rate depends exponentially upon the laser field strength this

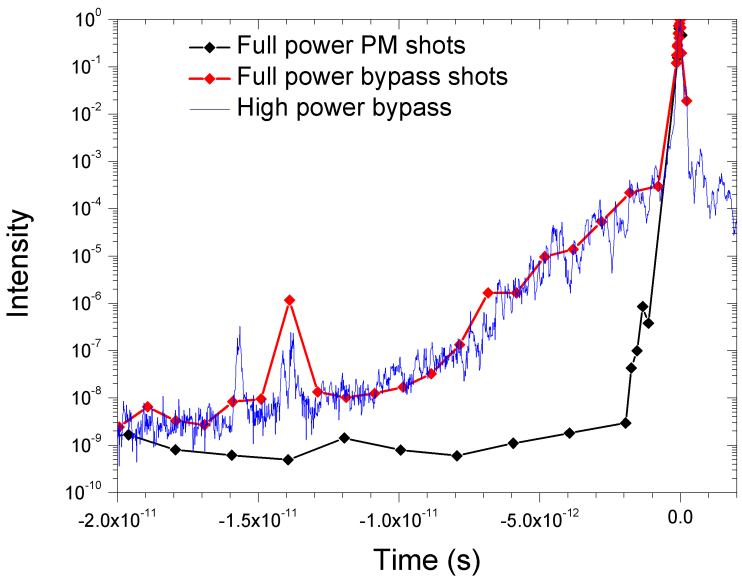

Figure 3.10: The pulse profile for the Astra Gemini laser (blue, red averaged over shots) and the resultant profile after DPM (black) (image courtesy of P. Foster at the Central Laser Facility).

switch-on time can often be considered instantaneous; an effect known as *fast shuttering* [71]. Since the fast shuttering effect is typically instantaneous with respect to the laser rise time, the ionisation rates and the material ionisation states are not overly important during the formation of the mirror [71]. However they do directly affect the intensity at which the mirror forms. The improvement a plasma mirror has on the laser pulse profile is typically quantified via the laser pulse contrast ratio (LPCR) [72] which is simply the ratio of the peak intensity and the intensity at any part of the pulse,

$$R = \frac{I_{\text{peak}}}{I_{\text{pulse}}} \tag{3.7}$$

Close to the pulse peak the LPCR is referred to as the coherent contrast [72]. In general a large coherent contrast corresponds to a sharp rising edge of the pulse which results in minimal production of preplasma. Typical plasma mirror setups will reflect the pulse directly into another mirror; these double plasma mirrors (DPM) can be used to achieve an increase in LPCR of around 4 orders of magnitude [7]. This paper discusses

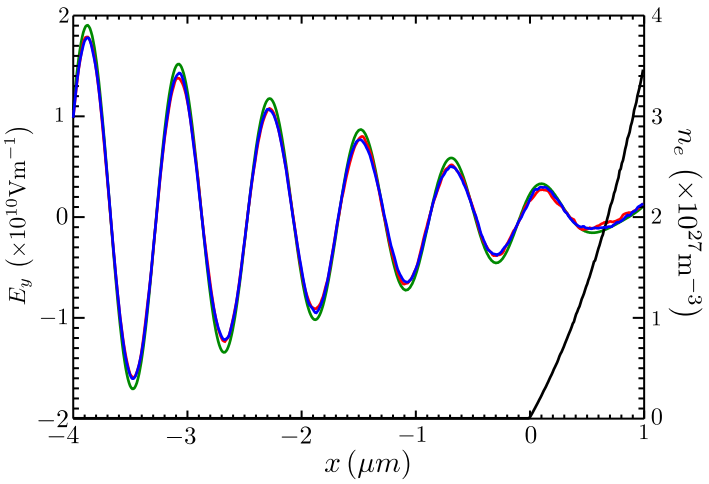

Figure 3.11: Reflected wave from plasma mirror surface found by $E_y - cB_z$ decomposition for the case of field ionisation excluding collisions (green), field ionisation with collisions excluding collisional ionisation (blue), and field ionisation with collisional ionisation (red). Dotted line illustrated position and shape of density ramp. The Astra-Gemini laser pulse profile is used from Fig. 3.10 with the laser peak at $3 \times 10^{15}\mathrm{Wcm}^{-2}$ and the density ramp for the mirror is given by $\frac{2n_c\left[\exp\left(10^6 x\right)-1\right]}{\exp(1)-1}$ with the neutral material initially cold $(296\mathrm{K})$. The simulation is performed over 512 grid cells at 2000 particles per populated cell using spline grid-to-particle interpolation.

the inclusion of a DPM system into the Astra Gemini laser setup at the Central Laser Facility; Fig. 3.10 demonstrates the laser to have a contrast ratio of 10^3 with respect to the prepulse which is improved to 10^7 by DPM.

3.4.1 Simulation and Analysis

The ionisation model was tested to first demonstrate the negligible switch-on time and its independence on material ionisation states, and then to reproduce the expected contrast ratio. These tests were performed using the pulse profile given in Fig. 3.10; the pulse profile was provided courtesy of D. Neely of the Central Laser Facility. For t in femtoseconds and I_0 the peak intensity the profile is given by,

$$I\left(t\right) = I_0\left(\mathrm{sech}^2\left(\frac{t}{28.4}\right) + 0.0002\mathrm{sech}^2\left(\frac{t}{500}\right) + 0.000002\mathrm{sech}^2\left(\frac{t}{3000}\right)\right) \quad (3.8)$$

For the switch-on time a 1D simulation is performed in a 0.9ps window around

the peak of the laser profile; outside of this region the intensity was below the threshold for ionisation and so could be neglected for this study. The neutral hydrogen density target is set to twice the critical density of the laser such that an overdense plasma could be formed. Due to the high density it should be necessary to consider collisions, therefore we include collisional ionisation in addition to field ionisation. In the case of field ionisation without collisions evanescent waves within the plasma were visible and 100% of the original intensity was reflected; the difference is illustrated in Fig. 3.11. In the case of field with collisions, it was found that the density profile of the plasma mirror formed identically and that $\sim 90\%$ of the original intensity was reflected. This absorption can be attributed to collisional damping.

The result for both modes of ionisation including collisions yielded the same results as for field ionisation with collisions in the absence of collisional ionisation. It is important to note that to achieve these results it is necessary to use the Manheimer collision frequency available within the collision module. By default the collision module will use a velocity based collision frequency that is only valid for warm plasmas, and to simulate the plasma mirror formation we use initially cold, neutral material. It was found that using the default velocity collision frequency resulted in excessive collisional damping which reduced the reflected intensity to $\sim 1\%$ and also appeared to greatly amplify the self-heating effect due to not resolving the Debye length resulting in unreasonably energetic electrons. The Manheimer collision frequency connects high and low velocity approximations to collision frequency taken from the NRL Plasma Formulary and uses a simple analytic transition between the two regimes [73, 74].

As the shape of the electron density is identical in all three cases we observe that collisional ionisation has no impact on the final state of the hydrogen plasma mirror. Next the impact on the switch-on time was considered for the three cases. Ionisation begins to occur at the same point in both cases around 10^{13}Wcm^2, this is expected and necessary as free electrons are required for collisional ionisation to occur. The switch-on time of the mirror in the absence of collisions is seen to occur over 20fs as shown in Fig. 3.12 with the simulation performed under the conditions laid out in Fig. 3.11. This is small in comparison to the pulse duration and laser frequency which is consistent with the near instantaneous fast shuttering effect expected.

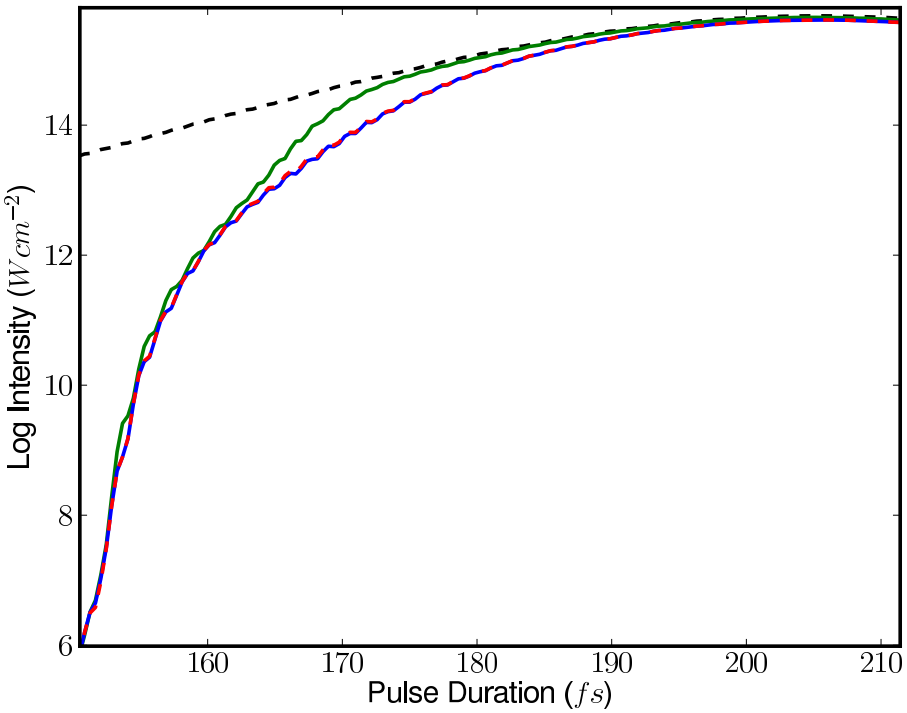

Figure 3.12: A laser strikes solid hydrogen and both the incident and reflected laser field are plotted. These are decomposed using $E_y + cB_z$ for the forward and $E_y - cB_z$ for the backward wave, averaged over $[-3.75\mu\text{m}, -1.75\mu\text{m}]$ in front of the mirror. Cases shown are field ionisation excluding collisions (green), field ionisation with collisions excluding collisional ionisation (blue), and field ionisation with collisional ionisation (red). Original pulse profile is indicated by a black dashed line.

The results seem to suggest that collisional ionisation slows hydrogen plasma mirror formation but it was seen that the switch-on time of 30fs was identical for the case using field ionisation with collisions but excluding collisional ionisation. This can be understood by considering the change in field intensity during mirror formation as the plasma produced by ionisation becomes collisional. The collisional absorption lowers the incident intensity which in turn lowers the field ionisation rate and since the absorption increases closer to the critical surface we can expect the absorption to increase as the mirror begins to form. Therefore the addition of collisions gradually impedes ionisation up to critical density. Collisional ionisation was therefore not found to play any role in the hydrogen plasma mirror formation as the field ionisation at $\sim 10^{15}$Wcm^{-2} is sufficient to quickly ionise neutral hydrogen.

It was expected that collisional ionisation would play a significant role when field ionisation is unable fully ionise the neutral material, as would be the case in higher-Z materials. This was investigated for glass, a typical material for plasma mirror substrates; this was modelled to be solid SiO_2 of the same density as the hydrogen plasma mirror. This was done by using $1/3$ of the density as silicon and $2/3$ oxygen; molecular structure was neglected such that each superparticle represented one oxygen or silicon atom for the 2000 superparticles per species per cell used. It was observed that the 3×10^{15}Wcm^{-2} pulse would field ionise oxygen and silicon to the 2nd and 4th ionisation state respectively, whilst higher states could only be reached by collisional ionisation. The result is a higher electron plasma density in the collisional ionisation case; this had the affect of greatly increasing the amount of collisional absorption as shown in Fig. 3.13, but no affect on the rate at which the plasma mirror forms. This reinforced the material independence of the fast shuttering effect asserted in [71].

It should be noted that the amount of collisional absorption observed in Fig. 3.13 is excessive for both collisional cases (up to $\sim 60\%$ in the collisional ionisation case). This appears to be due to an overestimated collision frequency as was the case with using the velocity collision frequency for hydrogen plasma mirror formation. The use of the Manheimer collision frequency only appears to mitigate this issue which is clearly present in the absence of collisional ionisation. Reviewing the electron temperature also

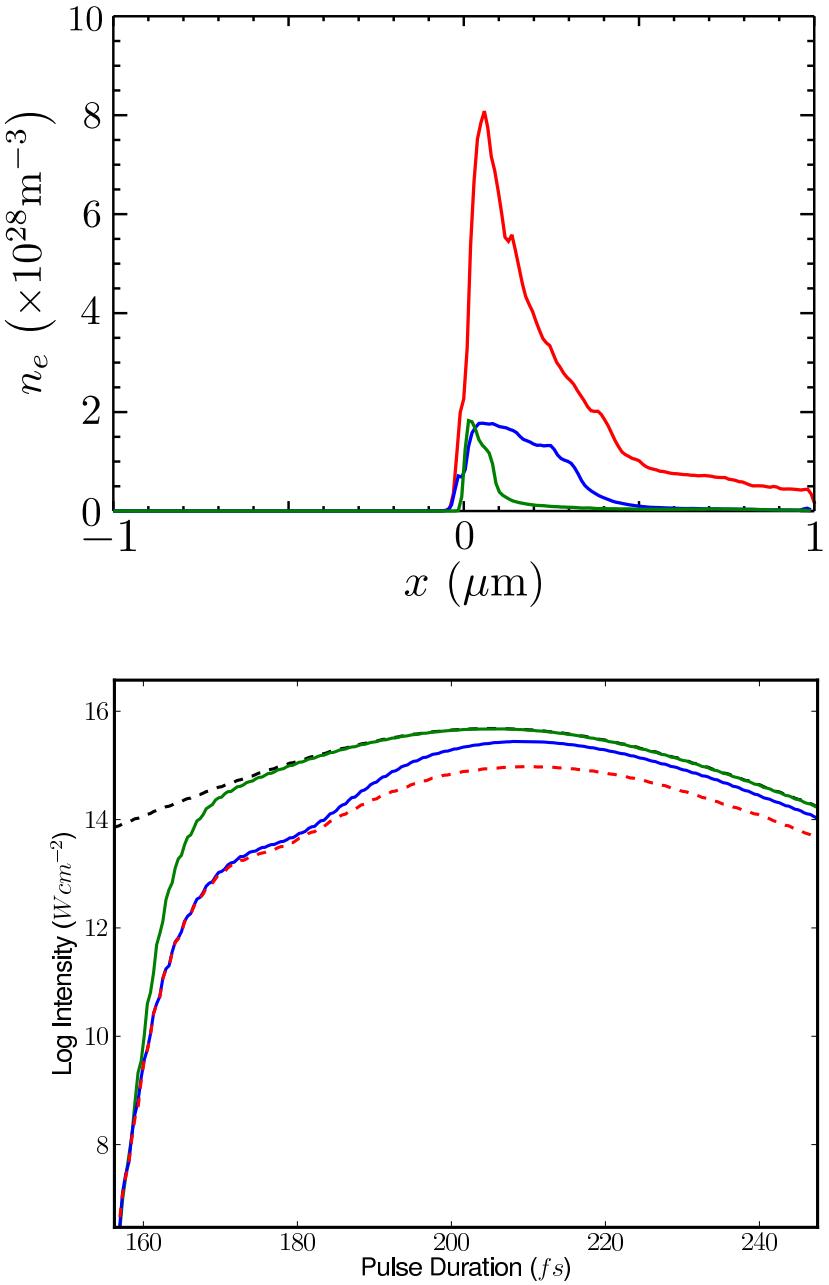

Figure 3.13: The simulation illustrated in Fig. 3.12 is repeated for glass. The electron plasma density (top) at the end of the simulation is largest for the collisional ionisation case (red), and very similar for the field ionisation only with (blue) and without (green) collisions. The reflected pulse profiles are shown for field ionisation excluding collisions (green), field ionisation with collisions excluding collisional ionisation (blue), and field ionisation with collisional ionisation (red). Original pulse profile is indicated by a black dashed line.

indicates the presence of numerical heating which increases with electron plasma density and is absent when collisions are neglected. Three potential sources of the issue were identified,

- The collisions module ignores neutral particle collisions which may serve to exaggerate the collisions between the charged particles
- The Debye length was not resolved on the simulation grid
- The electron plasma density was $\sim 10^{27}\text{m}^{-3}$ for which the electron skin depth is $\sim 50\mu$m which is not contained within the 1μm depth of the plasma mirror

To test whether the cause was neglecting neutral collision, the plasma mirror formation simulations were repeated with the neutral material initially fully ionised; it was found that this still demonstrated excessive absorption and heating. This also helped to eliminate the collisional ionisation implementation as the source of the issue. Two more test cases for initially ionised mirrors were run; firstly resolving the Debye length, then increasing the electron plasma density such that two electron skin depths were contained within the depth of the plasma mirror. It was found that both test cases exhibited the excessive absorption and heating. This appears to be an issue with the collisions module which is presently unresolved; it is expected that in future this issue will become resolved by the module authors in the near future. However at the time of writing it must be concluded that the collisional model may not be used to simulate higher-Z materials. A possible explanation for this exists in that the Manheimer collision frequency is invalid in the warm dense matter regime; whilst the plasma is rapidly heated by the laser immediately following ionisation there is both a period of heating and a falling temperature gradient into the mirror. Both are points at which the temperature of the plasma can be below the valid range for the collision model. The collision model is tested to be valid for $T > 100$eV and so as a temporary measure it is suggested to manually limit the collision frequency to that at $T = 100$eV which can be easily achieved in the collisions module within the *scatter* function.

We have demonstrated at least for hydrogen that collisional ionisation plays no role in the formation of a hydrogen plasma mirror for a sufficiently powerful laser.

We have also found that although collisions produce excessive absorption for higher-Z materials, the collisional ionisation only affects the final density of the plasma mirror and the reflected intensity but has no impact on the rate of formation in the glass plasma mirror case. The final two studies in this section are considered in the absence of collisions.

It is important to note that Fig. 3.12 and Fig. 3.13 both seem to exhibit an infinite LPCR in that the material shifts from perfectly transmitting to perfectly reflecting over the switch-on time. This is because when there is no reflection the LPCR is undefined according to Eq. (3.7), therefore it cannot be found in the absence of cold reflectivity of the neutral material prior to ionisation. Whilst it is a simple matter to approximate the LPCR prior to ionisation based on the expected reflectivity of the material, it is an equally simple matter to include a basic model for neutral reflection into EPOCH. The intention of this short study was to verify that the inclusion of neutral reflection produces expected, published results for single plasma mirrors [7].

From §1.3.2 we see that the PIC field solver uses the Maxwell equations for a vacuum. The equations are readily amended to approximate the reflectivity of the material by simply including the relative permittivity such that we replace all instances of ϵ_0 in the equations with $\epsilon_0\epsilon_r$. We assume the mirror is not strongly magnetic such that we can neglect relative permeability, and also that the material is an insulator such that conductivity can be neglected. The input deck is then modified to allow for input of relative permittivity for convenience. It should be noted that the changes to the code described here are not included in the release of the ionisation model as it is only the simplest model for inclusion of reflection and is quickly and easily replicated. For those attempting reproduction note that the relation $c = (\epsilon_0\mu_0)^{-1/2}$ is used in the field update and this too requires the inclusion of ϵ_r.

As including the relative permittivity in Maxwell's equations is a very basic model to achieve cold reflectivity, we tune ϵ_r such that the neutral reflection is at the 0.7% reported for the glass substrate mirror used in the Astra-Gemini laser [7]; it is found this is the case for $\epsilon_r = 1.5$. The glass plasma mirror including cold reflectivity is shown in Fig. 3.14 and the LPCR for a single mirror is found to be 10^2. This is the maximum expected value in the absence of collisional absorption as limited by the cold

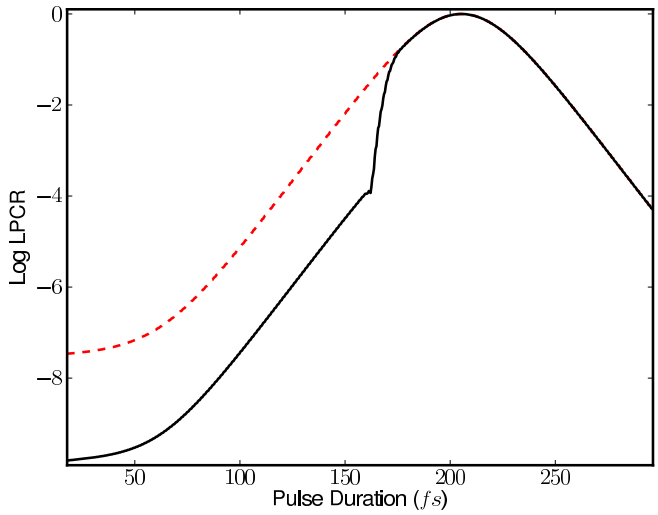

Figure 3.14: Simulation as laid out in Fig. 3.13 in the absence of collisions with the inclusion of a relative permittivity of $\epsilon_r = 1.5$ to give a 0.7% cold reflectivity from the neutral material. Plot gives the LPCR with respect to the peak of the incident laser field for the incident laser (red) and the reflected laser (black).

reflectivity (e.g. $\sim 1\%$ reflectivity to 100% on ionisation), and is consistent with the LPCR for double mirrors of 10^4 presented in [7]. In choosing a material for a plasma mirror, minimising the cold reflectivity to increase the contrast ratio per single mirror is a primary consideration. However in this collision-free model, the switch-on time may be underestimated as Fig. 3.12 demonstrates.

Although these 1D simulations are useful for analysing the switch-on and material dependence of a plasma mirror, in reality the mirror will not be reflecting directly back into the optics. When considering an oblique incident angle we have the possibility of the laser being s- or p-polarised (e.g. electric field perpendicular or parallel to the plane of the mirror). When p-polarised we will encounter damping even in the absence of collisions due to resonance absorption at the critical surface as described in §1.2; Fig. 3.15 demonstrates the intensity loss of the p-polarised laser. In both instances the pulses have lost energy as they are measured away from the mirror and thus have undergone diffraction.

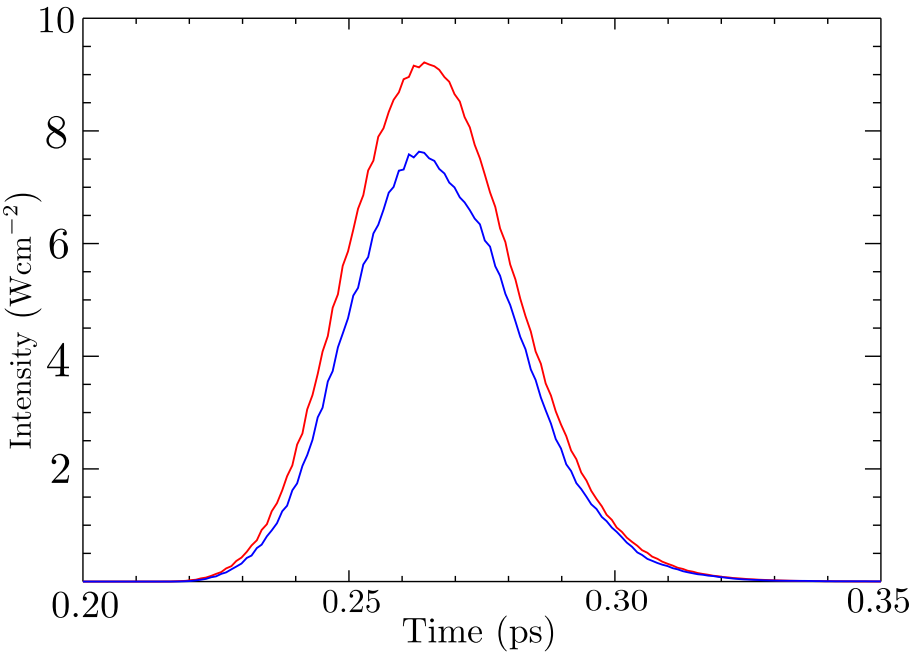

Figure 3.15: Astra-Gemini laser pulse with spot size 2μm striking neutral hydrogen presenting a mirror plane at $\pi/4$ to the incident pulse. Domain is $16\mu\text{m} \times 24\mu\text{m}$ split over 512×512, laser enters the left of domain, strikes the mirror, and reflects to the bottom of the domain. The reflected laser components exiting the bottom of the domain are found using the decomposition $E_x + cB_z$ for the p-polarised pulse (red) and $E_z - cB_x$ for s-polarised (blue).

3.5 Ionisation Injection

Laser wakefield acceleration (LWFA) of electrons is a novel alternative to particle accelerators that may serve to reduce the cost and space requirements of laboratory electron accelerators. The use of a laser to accelerate electrons in the wakefield of a plasma wave was first suggested by Tajima and Dawson [75], who noted at the time that intensities of glass lasers had reached 10^{18}Wcm^{-2} whilst the electron beams produced by conventional radiofrequency particle accelerators had only reached 10^{13}Wcm^{-2}. Whilst certainly not directly comparable devices, this simple fact did motivate an investigation into how to use lasers for reliable electron acceleration.

The mechanism by which wakefield acceleration occurs is now well understood and verified by numerous published experimental results; modern investigation focusses upon how to increase the population of electrons being accelerated by this mechanism. Umstadter *et al.* suggested selecting the gas and laser intensity used for LWFA such that field ionisation of tightly bound electrons would occur in such a way that the ionised electrons would be added exclusively to the accelerated electron bunch [76]. McGuffey *et al.* presented the first experimental results of this *ionisation injection* as a means for enhancing the high energy electron population for LWFA [5]. We initially describe the mechanism of laser wakefield acceleration and show simulations of the plasma wave formation with the subsequent wakefield structure, then LWFA is discussed in the context of ionisation injection and the results presented by McGuffey *et al.* are reproduced.

3.5.1 Wakefield Acceleration

During the oscillation of an electron plasma wave, the electrostatic field at the centre of the oscillation can become extremely high. At the most fundamental level, wakefield acceleration is the acceleration of electrons within this strong electrostatic field. This does of course imply that the acceleration occurs within a plasma and as we shall discuss this has some interesting consequences on the electron beams produced. A typical conventional electron accelerator uses radiofrequency within a long cavity. However these devices are fundamentally limited below the electric field strength at which the cavity begins to break down and, somewhat ironically, become a plasma. To increase the

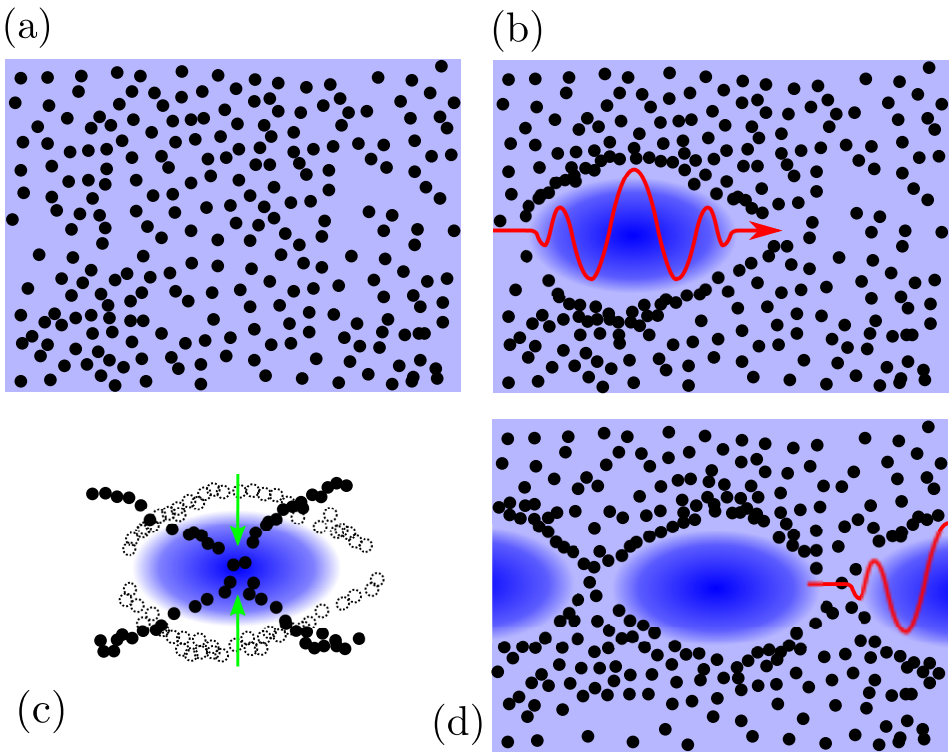

Figure 3.16: Illustration of wakefield formation; (a) the plasma is initially quasi-neutral, electrons are indicated by black dots and the neutralising ion background is shown in blue, (b) an incident laser *blows* the electrons out of the path of the pulse creating a *bubble* of high positive charge density (dark blue), (c) the strong electrostatic field initiates an electron plasma wave, (d) the structure appears to trail in the wake of the pulse giving rise to a laser wakefield.

resultant electron energy from the process of acceleration, the only option is to increase the length of the accelerator or make it cyclical as with synchrotrons. However even with synchrotrons, the device becomes very large as the maximum angular acceleration is limited by the breakdown field; this puts a limit on rate of curvature. In Tajima and Dawson's work they note the maximum electric field in these devices is $10^{9}\mathrm{Vm}^{-1}$ but in a plasma wakefield the electrostatic field rise as high as $10^{11}\mathrm{Vm}^{-1}$ using $10^{18}\mathrm{Wcm}^{-2}$ lasers as drivers [75].

Wakefield acceleration describes a few different methods of electron acceleration, the key mechanism uniting them being the acceleration of electrons within an electron plasma wave. In general, the method of wakefield acceleration is defined by the driver used to initiate the electron plasma wave; this can be a laser (LWFA), an electron

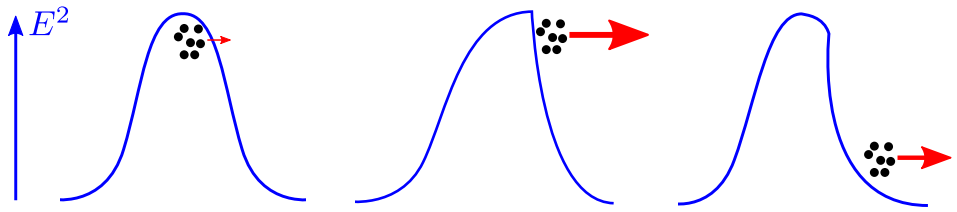

Figure 3.17: The electron acceleration is maximised at the rear of the bubble as the amplitude of the electrostatic wave begins to break. The velocity of the electrons can be such that they can keep up with the group velocity of the electron plasma wave and thus "surf" it.

beam (plasma wakefield acceleration, PWFA) [77], or in a more unusual case the beat frequency of multiple laser pulses (laser beat wave accelerator, LBWA) [78]. In explaining wakefield acceleration we will focus exclusively upon LWFA, but it is helpful in following and understanding modern research to know that the use of a laser is not necessarily key. As discussed in §3.3 a typical Gaussian profile laser propagating through a plasma will ponderomotively expel electrons out of the most intense regions of the laser and into the fringes. In the most extreme case the electron population can be entirely vacated from the core of the laser; a situation known as *blowout*. In this case the charge density becomes highly positive in the core of the laser and highly negative in the fringes; this sets up an electrostatic field which initiates the electron plasma wave. This region of positive charge density surrounded by the expelled electrons is called the *bubble* and is more clearly illustrated in Fig. 3.16.

The strength of the electrostatic field in the wakefield is dictated by the electron plasma density but as it transpires even a hydrogen gas at atmospheric pressure will yield $\sim 500\text{GVm}^{-1}$ for a laser sufficiently intense to produce a bubble structure. Up to this point we have only discussed how to produce this structure and not how the electrons become accelerated through it. As it transpires the electrons are self-injecting at the rear of the bubble. As can be seen in Fig. 3.16(c) the electron density reaches a maximum where the the top and bottom of the bubble structure cross after the initiation of the electron plasma wave. The electrostatic field becomes so strong here that electrons can be accelerated forward and begin to outrun the propagation of this crossing point (i.e. exceed the group velocity of the electron plasma wave and enter the bubble). This is a specific case of wakefield formation called *wavebreaking* first highlighted by Modena

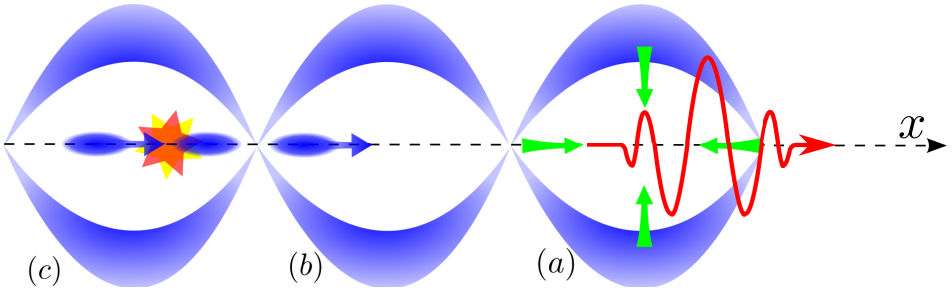

Figure 3.18: Summary of laser wakefield acceleration by self-injection; (a) the incident laser pulse that sets up the *bubble* structure with strong electrostatic fields that all point to the centre, (b) electrons can subsequently be driven inside the bubble at the back of the wave during wavebreaking, (c) as the electrons outrun the wakefield they can meet the trapping field at the front of the bubble, become decelerated, and collide with oncoming electrons. This can spread the energy and spatial distribution of the resultant accelerated electron beam.

et al., in which the amplitude of the electron plasma wave reaches the maximum that can be supported by the plasma and electrons are thrown forward into the bubble. This was demonstrated in experiment to produce an electric field of up to $10^{11}\mathrm{Vm}^{-1}$ and accelerate electrons to $44\mathrm{MeV}$; this required relativistic driving lasers to produce [79].

3D PIC simulations at these relativistic laser intensities gave more insight into the plasma structures involved in wave breaking in the bubble regime [80]. Electron acceleration by wavebreaking is often explained using a surfing analogy; consider surfers on a water wave, the wave begins to break as the rear of the wave begins to outrun the front. The front becomes steeper allowing the surfers to become gradually accelerated and travel with the wave; at the point where the wave breaks the acceleration will have reached a maximum. Where the surfers are the electrons and the wave is the electric field amplitude this helps visualise how the electrons enter the bubble; this is illustrated in Fig. 3.17.

The surfing analogy raises another important issue in that it is possible for an electron to fail to "catch" the wave; this method of trapping electrons in the wakefield is particularly difficult to control. In addition it is possible that the electrons are accelerated to the point that they can catch up with other electrons trapped in the bubble and collide, this is summarised in Fig. 3.18. In experiment [81] the electron beam produced via this self-injection was shown to be well collimated but have a Maxwellian energy

spread; this is proposed to be a result of this uncontrolled injection and the collision of meeting accelerated and decelerated electron beams within the wakefield. Most recent investigation has been directed towards the better controlling the injection and trapping so as to produce the monoenergetic electron beams necessary for many accelerator applications [82, 83].

The wakefield is fairly stable structure and is readily produced in 2D PIC simulation; initially this was produced with EPOCH in a preformed plasma. The domain was 64μm wide reflecting boundaries top and bottom to simulate a gas capillary; it was then set 64μm long with a moving window that would follow the laser pulse for 0.75mm. The laser was 800nm with a 10μm spot and a Gaussian temporal profile with a 30fs full width at half maximum, and the domain was divided into 1024×1024 cells; it was found that any less than 8 cells per wavelength caused the wakefield structure to break up after relatively short propagation distance. The capillary was uniformly filled with a hydrogen plasma using 64 particles per cell and a density $\sim 1\%$ critical density. The wakefield was seen to form after a relatively short distance as shown in Fig. 3.19 and remain stable for the full propagation distance with a population of electrons accelerated into the rear of the bubble. As reported in previous works the relativistic laser intensity sees the electrons almost entirely vacating the wake of the laser and the electric fields within the bubble are large and mostly longitudinal.

3.5.2 Electron Injection by Ionisation of Higher-Z Gas

In the bubble regime, electrons are self-injecting into the trapping region as shown in Fig. 3.17 and Fig. 3.19. As the trajectory of electrons sees two beams from opposite sides of the oscillation meeting, collisions thermalise the distribution such that those injected into the rear of the bubble are fairly Maxwellian [81]. To obtain a monoenergetic electron beam it is necessary to control the injection of electrons into the bubble, for which various methods exist. Bulanov *et al.* suggest that the laser propagate down a density ramp [84]; since the electron plasma wave depends on the electron density this has the effect of slowing the oscillation thereby trapping more electrons whilst also lowering the intensity requirement for the bubble regime.

It is also possible to inject electrons using a separate laser travelling opposite

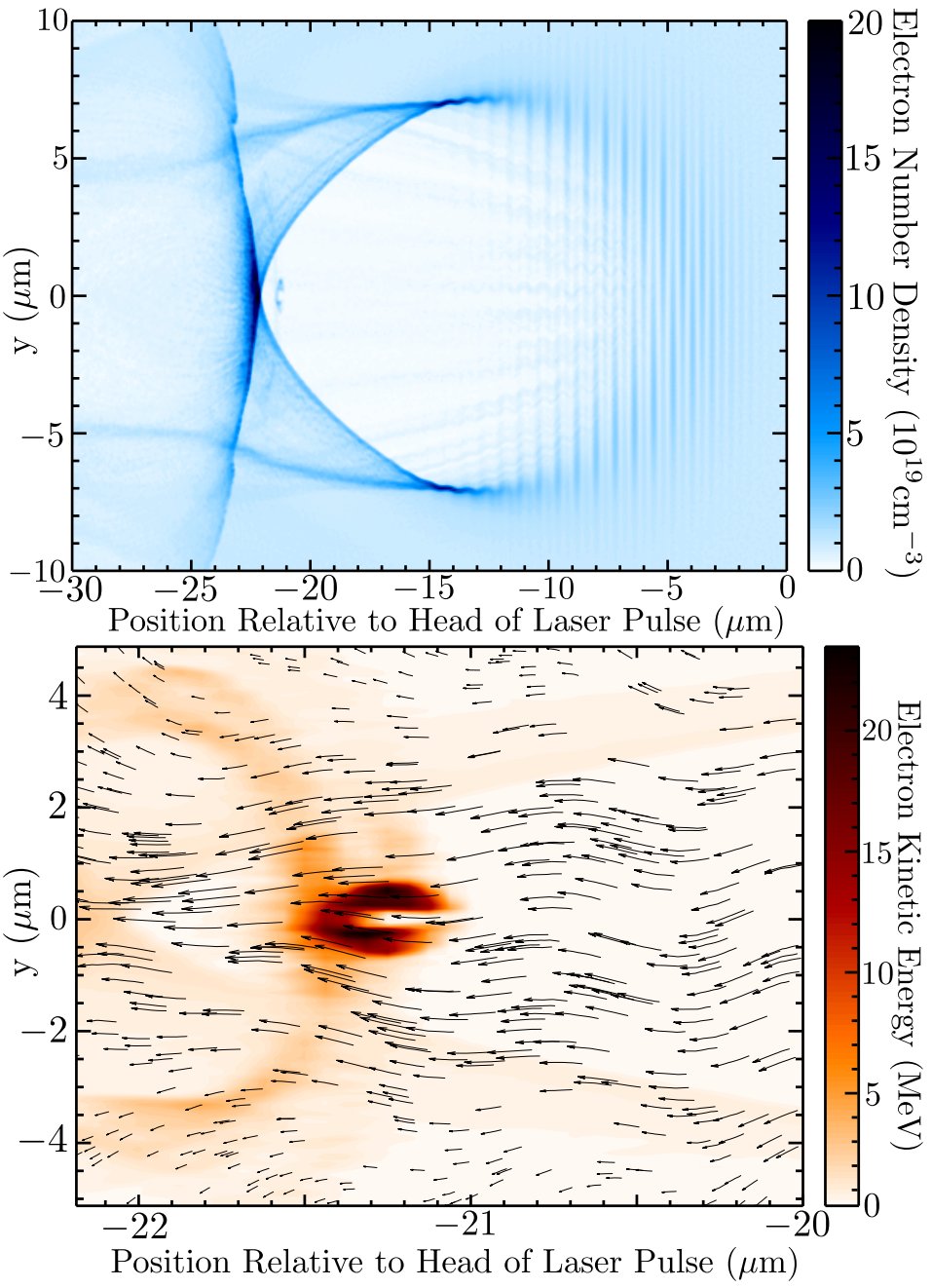

Figure 3.19: Simulation of 10^{20}Wcm^2, 800nm laser with a 10μm spot and a 30fs pulse (FWHM, Gaussian temporal spread) propagating into a capillary 64μm wide uniformly filled with hydrogen plasma with electron density 10^{19}cm^{-3}. Snapshot taken after 80μm propagation, top shows the bubble formation with electrons entering the rear, bottom shows the average electron kinetic energy with the direction of the electric field vectors plotted to illustrate the strong electron acceleration at the rear of the bubble.

to that driving the electron plasma wave; this is the previously mention LBWA scheme [76]. In this case where the laser pulses interact a ΔE^2 interference pattern occurs longitudinally such that some electrons may be accelerated into the bubble. Both of these methods require careful tuning of either the density of the plasma or the secondary laser pulse. In recent years, Rowlands-Rees *et al.* presented experiments in partially ionised hydrogen plasma channels where it was found that strong ionisation in the core of the laser tended to cause ionising electrons to be deposited inside the wakefield [85]. Rowlands-Rees *et al.* showed that ionisation could be used as a highly repeatable method for injecting electrons into the bubble structure, and went on to suggest that higher-Z gases may be used for more intense lasers to tune the ionisation energy to the self-focussed intensities reached.

McGuffey *et al.* present results [5] experimentally verifying the ionisation injection mechanism using a neutral helium gas mixed with $1\% - 5\%$ additives of various high-Z gases and laser intensities in the bubble regime for low electron plasma densities $< 1\% n_c$. McGuffey demonstrates an order of magnitude increase in high energy electron density with 1% nitrogen added to helium for a 0.8nm, 30fs laser pulse of focussed intensity 3×10^{19}Wcm^{-2} and spot size 10μm. To verify these results a 2D simulation was performed using the domain parameters laid out in §3.18.

In McGuffey's results the 1% nitrogen case showed as much as a 3 order of magnitude difference in electron density in the relevant region of the energy distribution compared to the pure helium case, this is illustrated in Fig. 3.20. This placed a minimum requirement on the number of superparticles within the simulation, as they needed to be able to represent this very small number density. It was found that the smallest number of electron superparticles required to correctly produce the energy distribution was 1024 particles per cell. However this placed a heavy computational requirement on the number of ions in the simulation; the number of electron superparticles in the simulation due to ionisation is dictated by the number of ionising neutral and ion superparticles within the simulation. In this case 1024 helium superparticles and 16 nitrogen superparticles per cell would produce electron superparticles of the required weight, and so by the end of the simulation the total number of superparticles per cell have more than tripled. However it was noted that in the results presented in [5] that the mixed

gas was preionised in all cases up to the inner s-shell of nitrogen, so to match this the helium was fully preionised from a neutral gas density of 10^{19}cm^{-3} whilst the nitrogen preionised to the fifth ionisation state (i.e. N^{5+}). The N^{5+} was added at 1% the density of the helium, and the preionised electron plasma density was therefore increased by 5%. Preionising the gas in this way relaxed the requirements on the number of ion superparticles as the majority of the electron superparticles were already present at the start of the simulation; 1024 electron and 16 N^{5+} and He^{2+} superparticles per cell were used for the simulation.

As the ionisation module allows specification of multiple electron species, the electrons from the ionisation of N^{5+} and N^{6+} were given their own species which allowed easier tracking and separation of the energy distributions for comparison with the preionised electrons. By separating the electrons in this way, Fig. 3.20 reveals that these deeply bound electrons are freed near enough to the trapping region that all are trapped and contribute to the accelerated electron population. The energy distribution of the helium and weakly bound nitrogen electrons compared to that of the strongly bound nitrogen electrons are found to be in reasonable quantitative agreement with McGuffey's results; the slightly lower maximum electron energy is attributed to the lack of self-focussing in z as a consequence of 2D simulation.

3.6 Discussion

We have demonstrated the field and collisional ionisation models to produce physical results and have explored the numerical scaling of the statistics. The inverse sampling method was shown to be effective in reproducing ionisation rates for relatively small numbers of superparticles. The previously used partial superparticle scheme was also presented as an alternative statistical model and a comparison was given to demonstrate that over a long enough time-scale the currently employed statistical model will produce the same results with much less computational overhead. Collisional ionisation was validated though the importance of including recombination was outlined and stands out as the most pressing extension to the ionisation module. The module is further demonstrated to correctly produce the three main mechanisms of ionisation in laser-plasma

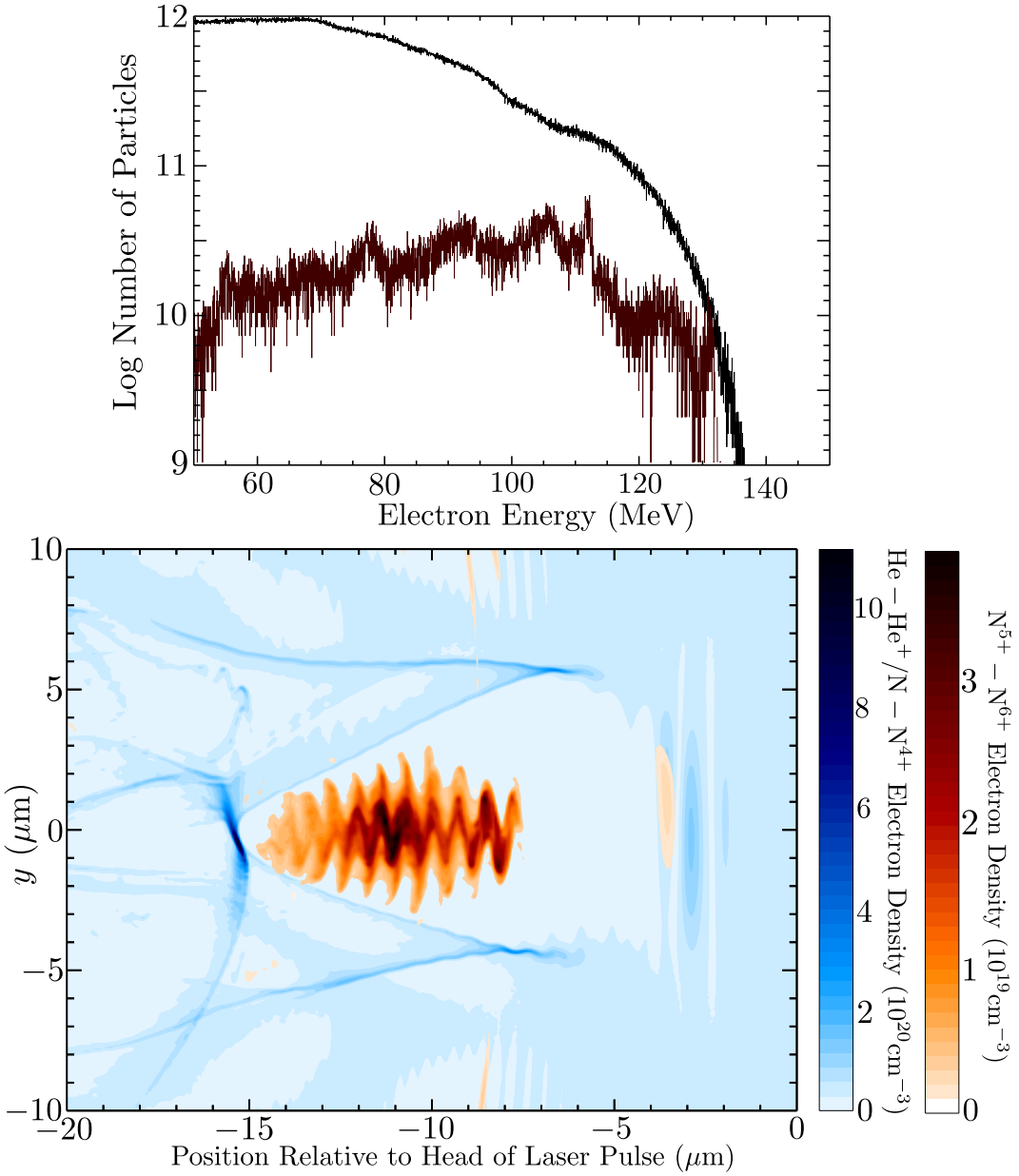

Figure 3.20: Simulation using domain parameters of Fig. 3.19, using preionised helium at neutral gas density of 10^{19}cm^{-3} with a 1% nitrogen additive preionised into the N^{5+} state; plots shown 250fs after laser pulse enters plasma. Top shows the energy distribution for the electrons produced from ionisation of N^{5+} and N^{6+} (black) and those preionised (red). Bottom shows the density of the N^{5+} and N^{6+} electrons plotted over the preionised electron density.

interaction; defocussing, fast shuttering, and injection. Defocussing is seen to match known theory, whilst fast shuttering and ionisation injection are verified against experimental result for plasma mirror formation and laser wakefield acceleration respectively. It is found that the Sentoku and Kemp collisional model used in EPOCH appears to produce excessive laser absorption at solid densities, and that this does not seem to be a consequence of ionisation. This presents difficulties for correctly modelling collisional ionisation within EPOCH. The possible resolution is to separate the collisional ionisation from the collisions module, as it is possible to model electron impact ionisation without modelling full collisions. Under this scheme the the electron-ion collisions would be neglected and the free electron-bound electron collisions would be modelled using the electron impact cross sections presented in §2.2.4. However, the validity of neglecting free electron-free electron collisions under this scheme would need to be investigated.

Chapter 4

SRS Backscatter-Induced Filamentation

The work presented in this chapter is a collaboration with C.S. Brady and T.D. Arber at the University of Warwick, the results of which were published in Physics of Plasmas in June 2012 [1] with the exception of more recent study presented in §4.2.2. Theoretical study has previously been published on the *filamentation* of ultraintense laser pulses in plasmas [86, 87]. Filamentation is an instability in which the spot of a pulse is split into multiple smaller propagating channels called filaments. At these high intensities the laser-plasma interactions must be considered relativistically; Brady takes into account the spatial distortion of the quarter critical surface due to relativistic effects when considering the seeding of filamentation by SRS backscatter [1], a parametric instability outlined in §1.2.1. Since the geometry of the plasma is critical to these effects and the ionisation of the neutral material by the laser determines this geometry, Lawrence-Douglas proposes that ionisation is a necessary consideration and may impact both the seeding of the instability and the propagation of the filaments. This chapter introduces the filamentation instability and the investigation by Brady into the seeding by SRS at the quarter critical surface, and subsequently Lawrence-Douglas' study of the impact by ionisation due to defocussing and injection of electrons at the point of filamentation seeding.

4.1 Filamentation

A typical laser has a transverse intensity profile due to the Gaussian spot shape and electrons in the presence of this electric field gradient are subject to the ponderomotive force (§1.2). This drives a transverse inhomogeneity in the electron density and causes the laser to be self-focussing due to the relation between electron plasma density and refractive index (§3.3). As the self-focussing is directly due to the electron density profile it is possible for this self-focussing to occur due to a pre-existing density perturbation. In this case the laser is focussed into the minimum of the electron density which serves to sharpen the transverse intensity profile and increase the ponderomotive force driving electrons from the most intense region of the laser. Since this also serves to increase the size of the density perturbation this is a feedback effect. Therefore, a small density perturbation can grow into a channel into which the laser is focussed.

The density perturbations that the laser can become focussed into can be smaller than the spot size. In this case a portion of the laser is channelled into a *filament* whose propagation runs independently from the main pulse. It is more common for a filamenting pulse to be divided into multiple filaments. As an example, a forming filament has a high electron density at the edges; adjacent to this the unfilamented portion of the pulse may go on to interact with this density gradient and form another filament. In this way the laser energy is split amongst multiple independent focussed channels from the parent pulse.

Filamentation often occurs near a critical surface in the plasma where the laser is reflected or absorbed; the filaments form plasma channels that are below critical density due to ponderomotive electron evacuation in the core, and these can then propagate beyond the point at which the main pulse is halted. These filaments do not always propagate along the same direction as the parent pulse which can have the effect of producing random hair-like structures sprouting from the head of the pulse, giving rise to the name filamentation.

Theory for transverse plasma density fluctuations seeding unstable growth of light filamentation was first presented by Kaw *et al.* [88]. There are many ways in which a transverse density profile can be formed even in a uniform plasma; the emitted electro-

magnetic wave from SRS [89] and SBS [26, p.93] can cause interference in the head of the pulse and drive the density perturbation. These seeds have been studied further in the relativistic regime [90, 86, 87] in which the laser pulse can also undergo *relativistic self-focussing*. This is an extension of self-focussing by plasma channel described in §3.3; when electrons velocities approach the speed of light the plasma frequency is seen to depend on the relativistic mass as $\omega_p = \sqrt{\frac{n_e e^2}{\gamma m_e \epsilon_0}}$ which influences the refractive index as Eq. (3.5). Since this occurs in the most intense regions of the pulse this will tend to form a focussing lens. Theory predicting relativistic filamentation due to SRS has previously been established by Shukla *et al.* [91] who suggests the effect will be critical in the nonlinear propagation of relativistic circularly polarised electromagnetic waves in a uniform plasma.

Filamentation has also been investigated in the context of ionisation-induced defocussing in neutral gases [92, 93]; it is observed that this could be a counteracting effect to the self-focussing that occurs during filamentation. Since the filaments may remain close to each other during propagation, it is suggested that ionisation-induced defocussing may serve to recombine filaments. Ionisation-induced defocussing has also been investigated next to a competing effect called Kerr-induced self-focussing [94]. Kerr-induced self-focussing occurs due to a material refractive index dependence on laser intensity of the form $n = n_0 + n_2 I$ for n_0 the unperturbed refractive index, I the laser intensity, and n_2 the component of material response to intensity. When n_2 is positive then there will be a transverse profile in refractive index with a maximum at the core of the laser therefore a focussing lens is formed. Due to self-focussing the intensity in a filament can be higher than the parent pulse and in this case the impact of Kerr self-focussing is maximised within the filament. This may serve to prevent recombination of the filaments by ionisation-induced defocussing.

Couairon and Bergé find a limiting gas density above which the strength of the defocussing can overcome Kerr self-focussing and cause recombination of the filaments [92]. For σ_{brem} the inverse Bremmstrahlung cross section, a the radiative recombination coefficient (units m^3s^{-1}), n the refractive index and ϵ the ionisation energy all in SI units this density limit is given by,

$$\rho_{\text{lim}} = \frac{2\sigma_{\text{brem}} I}{a n^2 \epsilon} \tag{4.1}$$

Filamentation is of particular interest to ICF (§1.1.1) as the filaments cause uneven illumination of the target sphere which can damage compression. In addition the filaments can drive further parametric instabilities or undergo resonant absorption closer to the D-T core resulting in fast electron heating before the desired compression has been achieved. MacPhee *et al.* [31] present PIC simulations of a 10^{20}Wcm^{-2} pulse in the cone-guided fast-ignition ICF scheme where the size of the prepulse is varied from 10^{10}Wcm^{-2} to 10^{12}Wcm^{-2}. Both modes demonstrate strong filamentation though in the lower intensity prepulse case this occurs $\sim 60\mu$m from the tip of the gold cone, and $\sim 120\mu$m for the higher intensity case. MacPhee's simulations show that this has a tremendous impact on the high energy electron density being driven into the core of the compressed D-T target; as much as an order of magnitude increase for the smaller prepulse. The PIC simulation in MacPhee's work was performed without ionisation, so to calculate the the preplasma used for these simulations MacPhee initially uses radiation hydrodynamics modelling with HYDRA for the prepulse [95]. Using the resultant preplasma for initial conditions, the PIC simulations for the main pulse are performed by using PSC [12]. In each case the filaments are seen to propagate approximately the same distance into the density ramp without recombining, therefore the point at which filamentation is initiated could be a key metric for determining success of the gold-cone fast ignition scheme.

Kaw *et al.* present a linear analysis of transverse density perturbations of a uniform cold collisionless plasma for an plane electromagnetic wave propagating in z [88]. By considering small perturbations of the field they demonstrate that unstable modes

grow in the direction of the wavevector due to a perpendicular density gradient. They go on to provide the fastest growth rate for the instability for ω and k the EM plane wave frequency and wavenumber respectively, ω_{pe} the plasma frequency, $v_p = {}^{eE}/_{m\omega}$ the cycle averaged electron quiver velocity, and v_T the electron thermal velocity,

$$\gamma = \frac{3k}{8}\left(\frac{\omega_{pe}}{\omega}\right)^2\left(\frac{v_p}{2v_T}\right)^2 \exp\left[-\frac{3}{8}\left(\frac{v_p}{v_T}\right)^2\right] \tag{4.2}$$

SRS occurs on the timescale of the laser frequency [26] whilst filamentation exhibits exponential dependence on the electric field strength and so can occur faster for more intense lasers. In general filamentation is relatively rapid following the onset of SRS. However the exponential dependence on electric field strength is also seen in the rate for tunnelling ionisation and so it is possible that field ionisation may occur rapidly enough to have a feedback effect on the increasing electric field associated with these unstable modes.

4.1.1 SRS Backscatter at the Relativistically Corrected Quarter Critical Surface

Brady states that the filamentation observed in MacPhee's work may be seeded by transverse density perturbation inherent from using radiation hydrodynamics to find the initial conditions for use in PIC simulation [1]. By simulating the idealised case of a relativistic laser pulse with a purely Gaussian transverse profile propagating up a smooth density ramp, Brady finds that filamentation still occurs near the *relativistically corrected quarter-critical surface* (RCQCS). He notes that the appearance of the filamentation at the quarter-critical surface is indicative of seeding by parametric instability and proceeds to eliminate the possible causes. By comparing a mobile and immobile ion case, SBS and the plasma decay instability are effectively eliminated as a source by suppressing ion-acoustic waves. Similarly the two-plasmon instability is suppressed by having the E-field component of the plane wave perpendicular to the plane of the 2D simulation since the $\mathbf{k}$ vectors of the incident electromagnetic and the produced electron-plasma waves cannot be in the same plane from the matching conditions (§1.2.1). In all cases the filamentation is seen still to occur; this implies that the seed for this filamentation

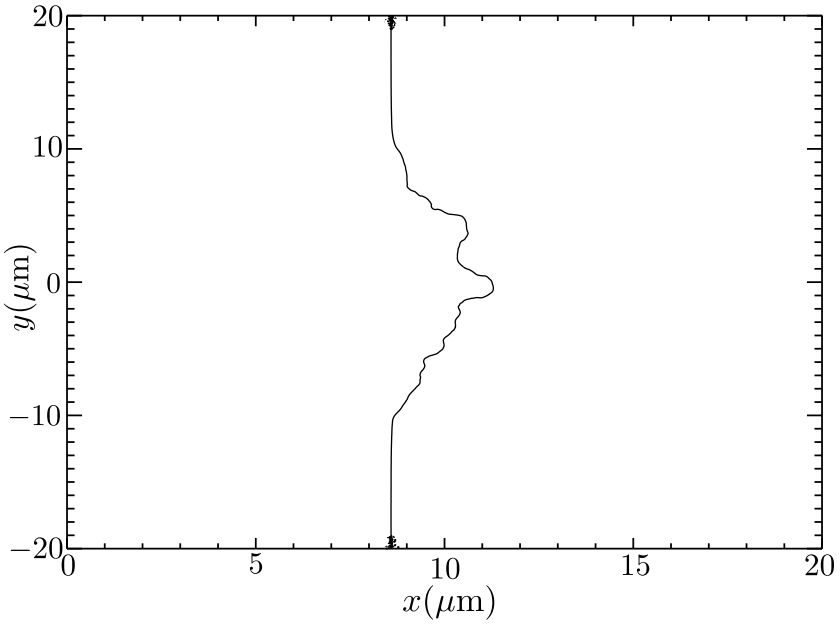

Figure 4.1: Shape of the relativistically corrected quarter critical surface (RCQCS) in an incident $\lambda = 1\mu$m, 10^{18}Wcm^2 laser of Gaussian waist 8μm. Boxcar averaged over 1μm and averaged over three simulations with initial conditions described in §4.2). Then subsequently time averaged from arrival of laser at the RCQCS to the initiation of filamentation.

is SRS.

The strongest mode of SRS is backscatter [26] and Brady finds the peak amplitude of SRS to be 20% at the quarter critical surface. The quarter critical surface therefore acts as a partially reflecting mirror but in a uniform density this does not in itself seed any density perturbation. However when considering the RCQCS we note that electrons are being driven to relativistic velocities in the core of the laser compared to the fringes; under relativistic correction the result is a curved mirror shape shown in Fig. 4.1. This reflection off of a curved mirror into the path of the oncoming laser causes a non-uniform interference pattern resulting in a transverse $\nabla\mathbf{E}^2$ force which drives the density perturbation and seeds the filamentation instability. Brady further verifies his analysis by using a parabolic reflection model to estimate the interference pattern based on averaged and fitted RCQCS curvature; using this he is able to closely predict the number and position of filaments [1].

4.2 Ionisation at the Relativistically Corrected Quarter Critical Surface

The work presented by Couairon and Bergé [92] is of limited application to this study; the ionisation-induced defocussing of the filaments did not take into account relativistic distortion of the plasma density and was considered in the multiphoton regime at intensities of $\sim 10^{13}$. Assuming that their findings apply in the ultraintense regimes where tunnelling and barrier-suppression are likely to be the dominant modes of ionisation, we can use Eq. (4.1) to find that for the first ionisation state of argon and a 5×10^{17}Wcm^{-2} laser we have $\rho_{\text{lim}} \sim 10^{28}$m^{-3}. This makes use of the values $\sigma_{\text{brem}} = 5.46 \times 10^{-24}$m^2, $a = 7 \times 10^{-13}$m^{3}s^{-1} and $n = 1.0003$ from [92]. This is greater than the critical density for $\lambda > 0.25\mu$m, and so for filamentation in a density ramp occurring near the quarter critical surface it is not expected that ionisation-induced defocussing will overcome the self-focussing of the filaments. However, we can see that with greater ionisation energy the value of ρ_{lim} drops, and so it is possible that defocussing may become relevant with successive ionisations. However this is beyond the scope of the analysis presented in [92] as self-focussing by plasma channel is not included therefore it is only applicable to neutral gas. We can still see that ionisation will have the strongest impact for the lowest relativistic intensities and so all simulations were performed at $\sim 10^{17} - 10^{18}$Wcm^{-2}.

4.2.1 Simulations of Hydrogen and Plastic

To investigate the impact of ionisation, initially the simulations as presented in [1] were repeated with a neutral hydrogen density equal to the electron density used by Brady; this study is performed in the absence of collisions so as to neglect damping, and as such collisional ionisation effects are not taken into account. The domain was 44μm $\times$ 40μm with the first 4μm set as empty space followed by a density ramp of cold neutral hydrogen rising exponentially to $0.8n_c$ over 20μm; the remainder of the domain is filled at $0.8n_c$. The incident laser has wavelength $\lambda = 1\mu$m and intensity $I = 10^{18}$Wcm^2 with a transverse Gaussian waist of 8μm and temporal profile for field amplitude A, peak field amplitude A_0, laser period T, and time t given by,

$$A(t) = \begin{cases} \frac{A_0}{2T\sqrt{2\pi}} \exp\left[-\frac{1}{2}\left(\frac{t-2T}{2T}\right)^2\right] & : \quad t < 2T \\ A_0 & : \quad 2T \leq t \end{cases} \tag{4.3}$$

The domain is divided into 2048×1024 or approximately 40 cells per wavelength in x and 20 in y with 64 particles per cell. The simulation was allowed to run for 1ps with results presented in Fig. 4.2; filamentation was observable through plots of the electromagnetic energy density and a comparison between the RCQCS in the ionisation and preformed plasma cases showed that ionisation did have some impact on the shape of the RCQCS. This was seen in the wings of the RCQCS which showed the position to be advanced in x; this occurs due to the fringes of the laser being insufficiently intense to cause full ionisation of the neutral gas initially, later in the simulation when the laser is at peak intensity these wings also ionise. These transient wings have no appreciable effect on the filament formation; this is easily understood as SRS backscatter in these regions is not directed into the the parabolic mirror so the interference pattern is not affected.

The simple hydrogen case provides a very powerful illustration of how fundamental this RCQCS mirror mechanism is in seeding filamentation. However this does not suffice for investigating the role of ionisation in the effect; under present designs for the gold cone scheme in ICF the laser can be expected to strike elements with more complicated electron orbitals such as plastic, aluminium and gold [96]. The runs demon-

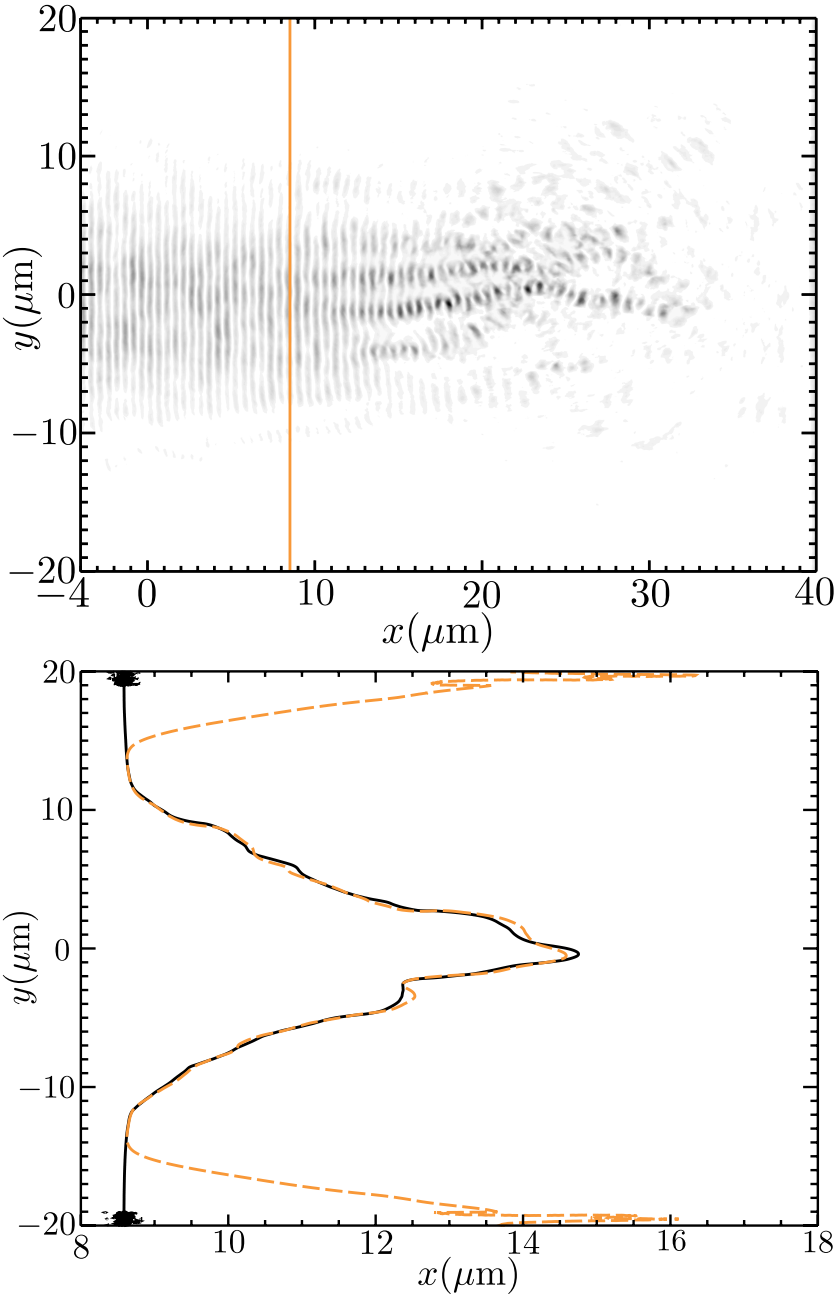

Figure 4.2: Mirror formation (bottom) and subsequent filamentation (top) in ionising neutral cold hydrogen for $\lambda = 1\mu$m, 10^{18}Wcm^2 laser of Gaussian waist 8μm. Top plot shows electromagnetic energy density with initial position of quarter critical surface indicated with orange line were the hydrogen fully ionised. Bottom plot shows the RCQCS averaged using method described in Fig. 4.1; black shows the initially fully ionised case and orange dashed shows the neutral hydrogen case.

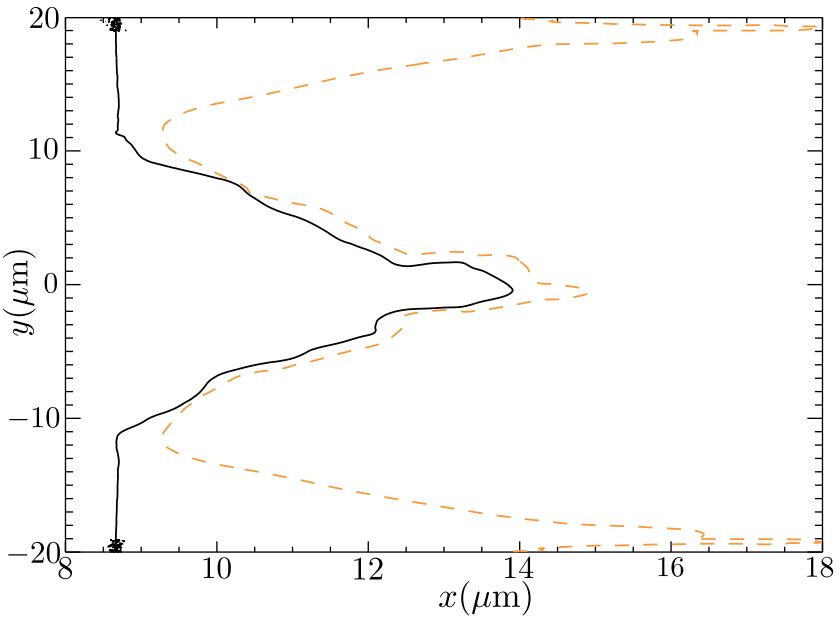

Figure 4.3: Position of RCQCS for cold CH_2 (plastic) in ionising (dashed orange) and pre-formed plasma (black solid) cases with incident laser of $\lambda = 1\mu$m, intensity 10^{18}Wcm^2, and Gaussian waist 8μm. Surfaces averaged using method described in Fig. 4.1.

strated in Fig. 4.2 were repeated for plastic modelled as cold CH_2 which may not fully field ionise in a 1ps 10^{18}Wcm^2 laser pulse. The molecule was approximated as a single free carbon atom and two free unbound hydrogen atoms; this affects the accuracy of the ionisation energies only due to the cold start. However it was found in simulation that the average charge on carbon ions was $Z \approx 4$ after the laser pulse and so only the innermost s-shell electrons are not fully ionised by the laser. As it is the $n = 2$ shell of carbon that bonds to hydrogen, the 1s-shell ionisation energies for free carbon should be a reasonable approximation.

For comparable runs to the hydrogen case, the density of CH_2 was chosen such that when the average ionisation state of carbon is reached the electron density would be $0.8n_c$ as in the hydrogen case. The number density of CH_2 was set assuming 6 electrons from each molecule. This resulted in RCQCS formation at a comparable location in the density ramp. Filamentation was observed initiating slightly further from the initial quarter critical surface as shown in Fig. 4.3 and it was was found that the whole position of the RCQCS was advanced in x compared to the fully ionised case. This can be attributed to the partial ionisation of the C^{4+} and C^{5+} states lowering the

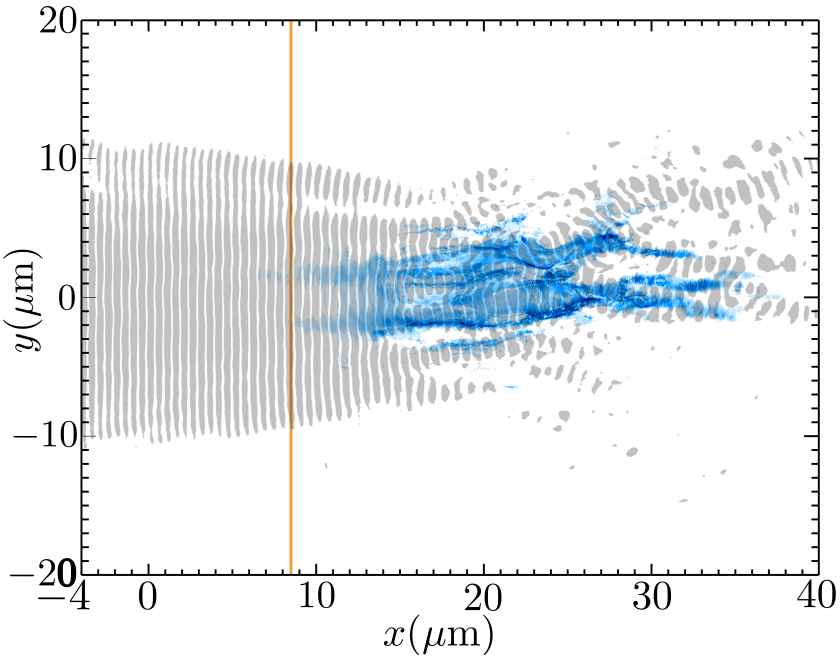

Figure 4.4: Number density of C^{5+} and C^{6+} ions (blue) within the incident laser pulse illustrated by electric field energy density (transparent grey) over the domain. Orange line shows the initial position of the quarter critical surface.

electron number density with respect to the hydrogen only case. This can be considered a consequence of reduced electron number density in the ionising plastic case due to incomplete ionisation rather than the influence of a key mechanism of ionisation of RCQCS formation.

In neither the hydrogen nor plastic case is ionisation-induced defocussing seen to recombine the filaments in any of the simulations. In the plastic case the 5th and 6th ionisation levels of carbon activate only in the filaments and weakly in the self-focussed portion of the laser pulse as shown in Fig. 4.4. This is ideal for defocussing of the filaments but the filamentation is seen to continue propagating into the gas suggesting that the self-focussing is dominant over the simulation domain. In MacPhee's simulations it is seen that the laser continues propagation in self-focussing filaments over a maximum of $\sim 60\mu$m from the point of filamentation. Further simulations were performed with increased domain length in x. These showed similar filamentation without recombination to that demonstrated in Fig. 4.2 and 4.4. It is therefore suggested that ionisation-induced defocussing does not overcome the effects of Kerr-induced and

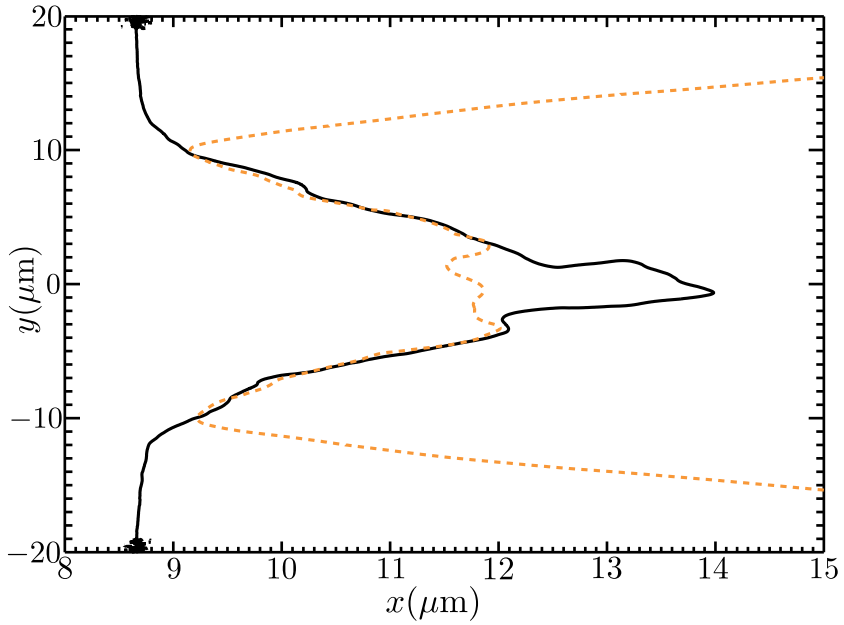

Figure 4.5: RCQCS flattening as a result of ionising Ar^{8+} through to Ar^{13+} in cold argon (dashed orange) compared to preformed plasma case (black solid) for an incident laser of $\lambda = 1\mu$m, intensity 10^{18}Wcm^2, and Gaussian waist 8μm. Surfaces averaged using method described in Fig. 4.1.

relativistic plasma self-focussing in the density ramps seen in ICF.

4.2.2 Higher-Z Materials and Relativistically Corrected Quarter Critical Surface Flattening

Following publication of these results, subsequent investigation by Lawrence-Douglas focussed on the introduction of electrons in the mirror by higher ionisation energies as seen in the plastic simulations in Fig. 4.3. In cases where the ionisation rate of higher ionisation levels are significantly increased during the self-focussing stage of RCQCS formation we see a new effect of RCQCS flattening. As the laser begins to break up into filaments the increased intensity caused by the self-focussing and the interference pattern from SRS backscatter is seen to increase the ionisation rate. This causes strongly-bound electrons to become ionised and inject at the location of filament formation. This occurs rapidly enough that it causes flattening of the curvature in the RCQCS during the onset of filamentation.

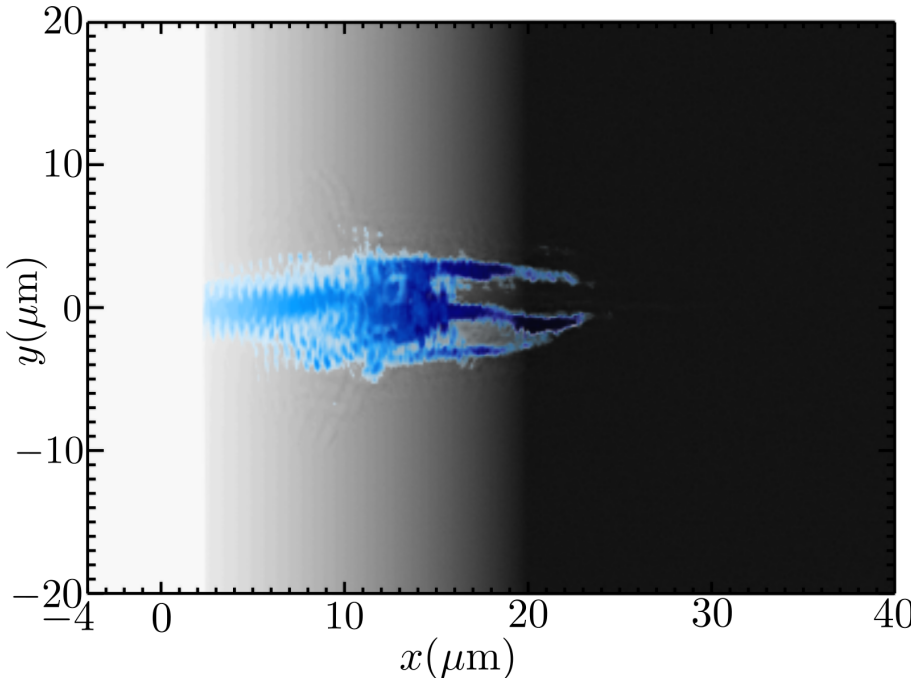

Figure 4.6: Summed number density of Ar^{+} through to Ar^{8+} (grey scale), and Ar^{9+} through to Ar^{14+} (blue); darker is more dense. Shown at 200fs; long after onset of filamentation.

RCQCS flattening was first observed under simulations of neutral argon with an incident $\lambda = 1\mu$m, 10^{18}Wcm^2 laser shown in Fig. 4.5. The simulation parameters are as presented in the hydrogen and plastic cases, with the density of argon again chosen such that the RCQCS forms in approximately the same place as for the hydrogen simulations with a maximum electron plasma density of $\sim 0.8n_c$. The average ionisation level is found to be Ar^{8+} so the density ramp of argon is set to be $n_e/8$. Fig. 4.6 shows the density ramp forming uniformly by ionisation of Ar up to Ar^{7+}. It is seen that the ionisation of Ar^{8+} through to Ar^{13+} occurs exclusively near the region of filament formation only as in the plastic simulations. RCQCS flattening is seen for argon but not plastic as there are more ionisation levels in argon releasing electrons at the intensities reached at the RCQCS. This creates a sharper density transition in the region of the filaments. Despite the change in the curvature of the RCQCS neither the time-scale for filamentation formation nor the number of filaments formed is altered from the equivalent preionised case.

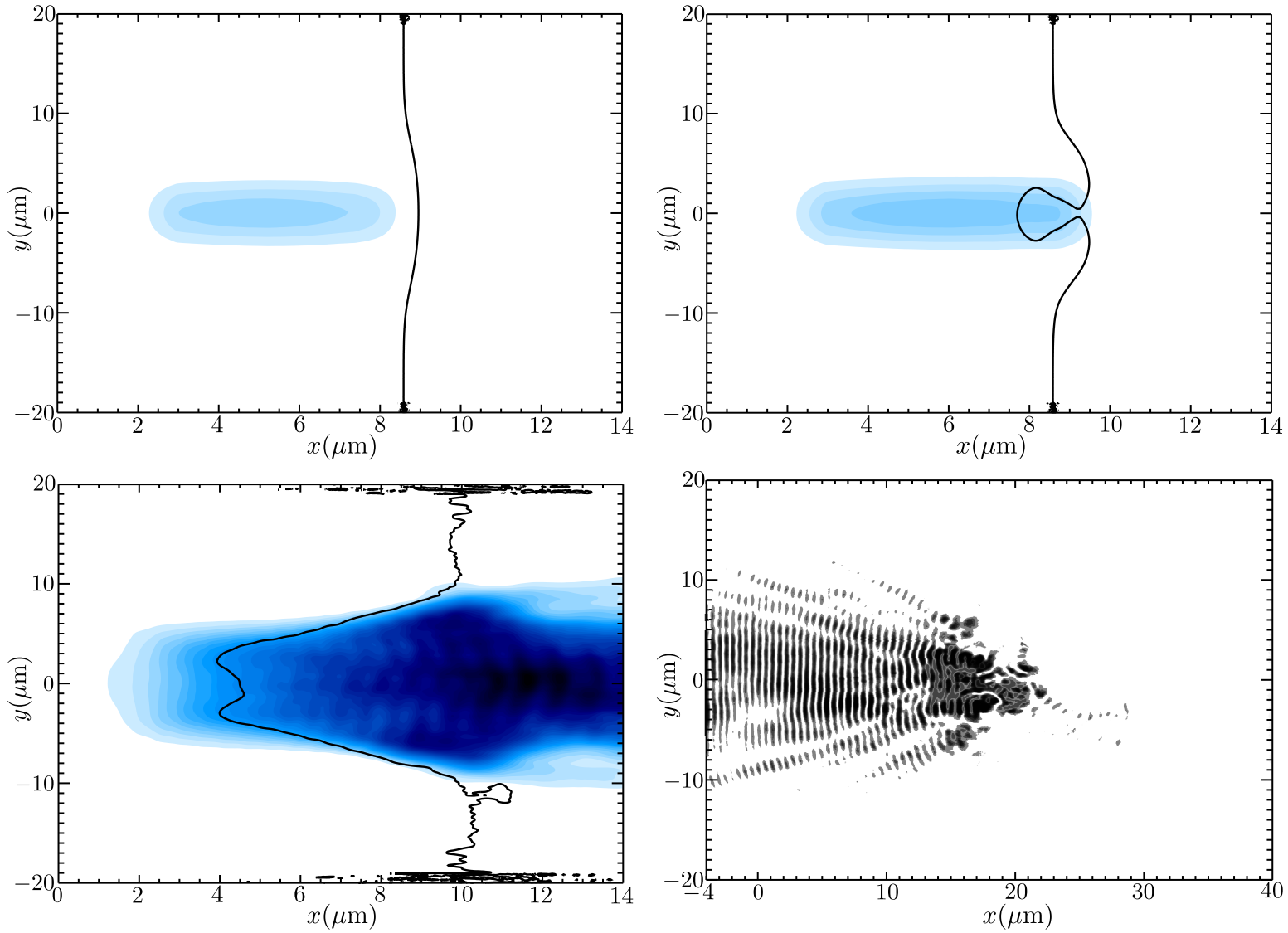

Figure 4.7: RCQCS (black line) flattening by a material with three ionisation levels (density of the ions produced by these levels shown in blue) activating as the laser self-focusses and the RCQCS begins to form (top left). Rapid ionisation causes the RCQCS to flatten (top right, 48fs) and subsequently invert (bottom left, 52fs) preventing filamentation and keeping the head of the pulse (energy density in grey scale) contiguous and hole-boring (bottom right,1ps).

To investigate if RCQCS flattening has the potential suppress filamentation an extreme case was invented for a test species starting singly ionised but with three additional ionisation levels activating strongly near the intensity found as the laser begins to self-focus. As ion motion is shown to be unimportant for this instability the mass of the test species was arbitrarily set to that of hydrogen, and the density was chosen such that the preformed plasma was identical to that of the hydrogen case. Under these conditions when the RCQCS begins to form, strong ionisation in the mirror curvature exaggerates the flattening effect. The ionisation energy that best promoted this effect was found through simulation to be $\epsilon \sim 225$eV. One such element with three ionisation levels near this energy is magnesium whose fifth, sixth, and seventh ionisation states ionise at 187eV, 225eV, and 266eV respectively. With three ionisation states releasing electrons at the intensities reached as the RCQCS begins to curve, we find that a critical surface forms and prevents the formation of the curved mirror surface. Without the curvature of the RCQCS the filamentation instability is not seeded and instead the pulse is forced to become hole-boring, driving into the overdense plasma by radiation pressure as a single contiguous laser spot. In the case presented here, the instability is suppressed by advancing the position of the RCQCS and causing the curvature to become convex as shown in Fig. 4.7.

4.3 Discussion

Brady demonstrates the onset of filamentation seeded by SRS backscatter to be an instability caused by fundamental relativistic geometry of the quarter critical surface [1], and is therefore likely to surface in all ICF target designs. Studying this effect in the context of ionisation shows that the filaments are robust against defocussing over the distances relevant to the MacPhee simulations and also against moderate flattening of the RCQCS by increase in electron density through field ionisation. However it is seen that in an extreme case where the density at the RCQCS can be risen to critical via rapid field ionisation that filamentation is suppressed by forcing the RCQCS to become convex, thus preventing the curvature that seeds the instability.

We have demonstrated that RCQCS flattening requires selection of materials

with ionisation energies such that strong field ionisation occurs at the intensities reached as the concave RCQCS curvature begins to form. However this affect may be difficult to reproduce experimentally as it is extremely sensitive to variation in the ionisation energy. Filamentation was seen to arise again as the binding energy of the three levels used in Fig. 4.7 was risen to $\epsilon \sim 300$eV. Since our ionisation model neglects electron excitation and molecular structure, and the ADK tunnelling rates are unverified for many higher-Z materials with the exception of noble gases, exact material selection would likely need to be determined empirically.

Whilst RCQCS flattening by ionisation does prevent filamentation the position of the critical surface moves closer to the laser source due to the increase of electron density at the head of the laser. In the context of gold cone fast ignition it may be be unfavourable for the critical surface to occur further from the tip of the cone; this was demonstrated in the MacPhee results where it was seen that the amount of energy reaching the tip dropped off greatly when the increased preplasma caused the critical surface to be further from the target [31]. However in the case where filamentation is known to occur too far from the tip due to excessive prepulse, then RCQCS flattening by ionisation could potentially suppress SRS backscatter-induced filamentation and cause the laser pulse to be purely hole-boring.

Chapter 5

Conclusions and Future Work

We have discussed various laser-plasma interactions and demonstrated the importance of ionisation in various phenomena including plasma mirror formation, laser wakefield acceleration, and laser filamentation. The particle-in-cell scheme for numerically modelling plasma physics has been described and EPOCH was introduced as being a feature-rich, highly extensible PIC code suitable for use in this project. In §2.3 we outlined a general scheme for implementing both field and collisional ionisation within the PIC code framework. It is described how this can be used for any ionisation model from which an ionisation rate can be extracted based on instantaneous physical parameters available during PIC simulation; in the case of field ionisation this was the self-consistent electric field strength at the particle and in the case of electron-impact ionisation it was the relative velocities of the colliding particles. In this way the ionisation model used can be altered without significant changes to the algorithm.

To support this extension to EPOCH, modifications are made to the text based input deck for specifying initial conditions relevant to ionisation. At present the user manually specifies the ionisation energies of the different levels for each particle species used in the simulation. An obvious extension to this may be to provide EPOCH with look-up tables to automatically find the ionisation energies of commonly used elements. Models for the two distinct regimes in field ionisation were provided from published work; for multiphoton ionisation we use of a semi-empirical WKB approximation by Ammosov *et al.* [34], and for tunnelling ionisation we use the Ammosov-Delone-Krainov or ADK rate [38]. We also use the barrier-suppression correction to the ADK rate by Posthumus

et al. for the special case of tunnelling where the electric field strength at the atom becomes so strong that the electron can escape classically [53]. We describe the use of the Keldysh parameter [35] to dynamically control which regime is implemented at runtime; the multiphoton and barrier-suppression regimes can also be deactivated in the input deck for a pure tunnelling model. Empirically determined cross-sections [56, 61] for electron-impact ionisation are also implemented and the method for handling the additional particles produced during ionisation is discussed for all ionisation models with respect to energy and momentum conservation.

The algorithm for handling an ionisation event makes use of the inverse sampling Monte Carlo method [63] using the ionisation rate determined from one of the ionisation models as the rate in an exponential decay. This method is shown to produce field ionisation rates matching with the published work of Nuter *et al.* [65] in §3.1 and similarly the collisional ionisation rates are verified against Fokker-Planck simulation results from Town *et al.* [50] in §3.2. It is found that by neglecting recombination of the ions and electrons that the total ionisation rate is overestimated by collisional ionisation for lower ionisation energies. In laser-plasma interactions exploring plasma formation from cold neutral material, it is suggested this overestimation will be most significant where field ionisation occurs slowly enough for electrons to be accelerated to collisionally ionising energies for these lower energy states. In these cases, it may be possible to model the field ionisation in the absence of collisional ionisation, and to subsequently use these results as initial conditions to analyse the collisional ionisation.

The inclusion of recombination to overcome the initial overestimation of collisional ionisation rates would be the most significant improvement to the ionisation module presented in this thesis. Modelling recombination would inevitably be computationally expensive; as an idea it would require locating each of the nearest neighbouring ions for every electron and the relative velocity would likely need to be below some threshold such that the electron could be captured. During a recombination event it would be extremely unlikely that the combining superparticles would be at exactly the same point in the domain or travelling directly towards each other therefore the effect on the current density would need to be carefully considered to ensure charge conservation is not broken. A method for grouping superparticles in the same grid cell is already

included in EPOCH and used by the collisions module; it may be possible to reduce the computational expense of recombination by modifying the collisions algorithm to test for recombination events as particles are colliding.

The effect of ionisation in laser-plasma interactions is summarised by its three main mechanisms in Chapter 2; ionisation-induced defocussing, fast shuttering, and ionisation injection. Simulations with field ionisation were performed for the first; the total divergence caused by the combined effects of Gaussian divergence and defocussing of the beam by ionisation was measured and found to be in good quantitative agreement with theory [70]. Fast shuttering was investigated in the context of plasma mirrors; due to the solid densities required both collisional and field ionisation were used in simulation. This was performed for both simple hydrogen mirrors and also glass; the laser profile from the Astra-Gemini laser at the Central Laser Facility so as to compare results with their published work [7]. Rapid switch-on of the mirror was observed for hydrogen and glass; in the latter the contrast ratio produced was found to agree with the theoretical maximum when taking into consideration the cold reflectivity and neglecting collisions. The fast-shuttering effect was found to be relatively material independent. It was also found that the switch-on time increased with the inclusion of collisions; this was attributed to the increasing laser absorption as the electron plasma density rose to critical, which had the effect of lowering the ionisation rate. In the case of glass, it was found that the amount of laser absorption became unreasonably high $\sim 60\%$ and the electrons exhibited excessive heating that appeared unrelated to the resolution of the Debye length, an instability discussed in §1.3.5. This was found to occur in the absence of collisional ionisation, and through further testing the issue was found to be due to the collision module implemented in EPOCH; it is expected that the issue will become resolved following submission of this thesis.

Ionisation injection was explored in the context of laser wakefield acceleration; the wakefield structure was produced via simulation of a laser propagating in helium gas in the absence of ionisation in EPOCH. Subsequently the simulation was modified to correspond to the experiment performed by McGuffey *et al.* using a 1% nitrogen gas dopant [5]. The results were found to agree with McGuffey's findings with all of the electrons from the ionisation of the fifth and sixth ionisation states of nitrogen be-

ing injected into the wakefield and contributing to the high energy electron population. Whilst the electron energy distributions in the pure helium and nitrogen doped cases were found to agree with those published in McGuffey's work, it required that the helium start fully ionised with the nitrogen ionised up to N^{5+} so as not to flood the simulation with unnecessarily large numbers of ion superparticles.

Also presented in this thesis is a partial superparticle ionisation scheme for modelling very small amounts of ionisation in a simulation with arbitrarily small number of superparticles; this could be modified such that ionisation releases very low weight electron superparticles whilst gathering positive charge on the ion/neutral superparticle until it reaches a threshold for releasing the ionised ion. Such a scheme would be very useful for analysing results such as McGuffey's, as it would allow viewing of the tail of the energy distribution where the electron population is relatively low. This could equally be achieved via splitting of the electron superparticles near the region of strong electron acceleration; in this case it would be necessary to develop a means of identifying where an electron is likely to become part of the high energy electron population at runtime. This could possibly be achieved using a "test" particle push where if the electrons are in or move into regions of high field strength, they are put back into their original positions and split.

The ionisation module presented in this thesis was applied to a collaborative study on SRS backscatter-induced filamentation for relativistic lasers propagating into a density ramp; this was completed with C.S. Brady and T.D. Arber at the University of Warwick [1]. Brady finds that under relativistic correction, the quarter critical surface exhibits a curvature where the laser is most intense. SRS backscatter off of this curved surface causes an interference pattern with the oncoming laser pulse which seeds the filamentation instability. Lawrence-Douglas reproduces these simulations with ionisation for initially neutral hydrogen, plastic and argon. It is found that the inclusion of ionisation does not significantly alter the shape of the RCQCS for hydrogen or plastic. However in the case of argon it is noticed that as the intensity increases at the RCQCS due to self-focussing and interference, more tightly bound electrons are injected which serves to flatten the tip of the RCQCS curvature. Whilst it is found this is not significant enough to alter the filamentation seeding, further study revealed that when the neutral

material has three ionisation levels that ionise as the intensity begins to increase, the density at the RCQCS is driven critical by the ionisation-injected electrons. This has the effect of rapidly flattening the RCQCS as it begins to form; this occurs faster than the filamentation can seed and therefore the instability is suppressed.

It is noted that RCQCS flattening is highly sensitive to the ionisation energy and that the ADK model is not experimentally verified against many higher-Z materials with the exception of noble gases. In addition the ionisation module presented here neglects electron excitation and molecular structure, instead assuming that electrons are always ionised from the ground state and that elements are monatomic. Therefore it is suggested that whilst simulation would assist in initial material selection for RCQCS flattening, experiment would be required to verify its ability to suppress the filamentation instability.

Bibliography

[1] C.S. Brady, A.A. Lawrence-Douglas, and T.D. Arber. Rapid filamentation of high power lasers at the quarter critical surface. *Physics of Plasmas*, 19(6):063112, 2012.

[2] C.P. Ridgers, C.S. Brady, R. Duclous, J.G. Kirk, K. Bennett, T.D. Arber, A.P.L. Robinson, and A.R. Bell. Dense electron-positron plasmas and ultraintense γ rays from laser-irradiated solids. *Physical Review Letters*, 108:165006, Apr 2012.

[3] T. Arber, C. Brady, and M. Haynes. Larexd user guide. *Centre for Fusion, Space and Astrophysics, University of Warwick*, 2007.

[4] P. Degond, L. Pareschi, and G. Russo. *Modeling and computational methods for kinetic equations*. Birkhauser, 2004.

[5] C. McGuffey, A.G.R. Thomas, W. Schumaker, T. Matsuoka, V. Chvykov, F.J. Dollar, G. Kalintchenko, V. Yanovsky, A. Maksimchuk, K. Krushelnick, et al. Ionization induced trapping in a laser wakefield accelerator. *Physical Review Letters*, 104(2):25004, 2010.

[6] S.C. Rae. Ionization-induced defocusing of intense laser pulses in high-pressure gases. *Optics Communications*, 97(1):25–28, 1993.

[7] M.J.V. Streeter, P.S. Foster, F.H. Cameron, R. Bickerton, S. Blake, P. Brummit, B. Costello, E. Divall, C. Hooker, P. Holligan, et al. Astra gemini compact plasma mirror system.

[8] S. Pfalzner. *An introduction to inertial confinement fusion*. Taylor & Francis, 2006.

[9] C.K. Birdsall and A.B. Langdon. *Plasma physics via computer simulation*. Inst of Physics Pub Inc, 2004.

[10] A. Pukhov. Three-dimensional electromagnetic relativistic particle-in-cell code VLPL (Virtual Laser Plasma Lab). *Journal of Plasma Physics*, 61(03):425–433, 1999.

[11] K. Fujimoto and R.D. Sydora. Electromagnetic particle-in-cell simulations on magnetic reconnection with adaptive mesh refinement. *Computer Physics Communications*, 178(12):915–923, 2008.

[12] M. Bonitz, G. Bertsch, V. S. Filinov, and H. Ruhl. *Introduction to Computational Methods in Many Body Physics*. Cambridge University Press, 2004.

[13] K. Miyamoto. *Controlled fusion and plasma physics*, volume 21. Taylor & Francis, 2006.

[14] S. Atzeni and J. Meyer-ter Vehn. *The Physics of Inertial Fusion*. Number 125. Clarendon Press, 2004.

[15] J. Nuckolls and L. Wood. Laser compression of matter to super-high densities: Thermonuclear (ctr) applications. *Nature*, 239:139, 1972.

[16] P. Amendt, M. Dunne, D. Ho, B. Lasinski, D. Meeker, and J.S. Ross. Stauts of the laser inertial fusion energy (life) hohlraum point design. Technical report, Lawrence Livermore National Laboratory (LLNL), Livermore, CA, 2012.

[17] L. Cicchitelli, S. Eliezer, M.P. Goldsworthy, F. Green, H. Hora, P.S. Ray, R.J. Stening, and H. Szichman. Volume ignition of laser driven fusion pellets and double layer effects. *Laser and Particle Beams*, 6(02):163–182, 2009.

[18] J. D. Lindl, P. Amendt, R. L. Berger, S. G. Glendinning, S. H. Glenzer, S. W. Haan, R. L. Kauffman, O. L. Landen, and L. J. Suter. The physics basis for ignition using indirect-drive targets on the national ignition facility. *Physics of Plasmas*, 11:339, 2004.

[19] D. H. Sharp. An overview of rayleigh-taylor instability. *Physica D: Nonlinear Phenomena*, 12(1):3–18, 1984.

[20] Y. Kitagawa, Y. Sentoku, S. Akamatsu, M. Mori, Y. Tohyama, R. Kodama, K.A. Tanaka, H. Fujita, H. Yoshida, S. Matsuo, et al. Progress of fast ignitor studies and Petawatt laser construction at Osaka University. *Physics of Plasmas*, 9:2202, 2002.

[21] L. Nikolić, M.M. Škorić, S. Ishiguro, H. Sakagami, F. Vidal, and T. Johnston. Particle simulations of high-intensity laser interaction with cone targets. In *Journal of Physics: Conference Series*, volume 112, page 022086. Institute of Physics Publishing, 2008.

[22] W. L. Kruer, S. C. Wilks, B. B. Afeyan, and R. K. Kirkwood. Energy transfer between crossing laser beams. *Physics of Plasmas*, 3:382, 1996.

[23] I. V. Igumenshchev, W. Seka, D. H. Edgell, D. T. Michel, D. H. Froula, V. N. Goncharov, R. S. Craxton, L. Divol, R. Epstein, R. Follett, et al. Crossed-beam energy transfer in direct-drive implosions. *Physics of Plasmas*, 19:056314, 2012.

[24] P. Michel, L. Divol, E. A. Williams, S. Weber, C. A. Thomas, D. A. Callahan, S. W. Haan, J. D. Salmonson, S. Dixit, D. E. Hinkel, et al. Tuning the implosion symmetry of icf targets via controlled crossed-beam energy transfer. *Physical review letters*, 102(2):025004, 2009.

[25] P. Michel, S. H. Glenzer, L. Divol, D.K. Bradley, D. Callahan, S. Dixit, S. Glenn, D. Hinkel, R. K. Kirkwood, J. L. Kline, et al. Symmetry tuning via controlled crossed-beam energy transfer on the national ignition facility. *Physics of Plasmas*, 17:056305, 2010.

[26] W.L. Kruer. *The physics of laser plasma interactions*. Reading, MA (US); Addison-Wesley Publishing Co., 1988.

[27] P.M. Bellan. *Fundamentals of Plasma Physics*. Cambridge University Press, 2006.

[28] N. J. Sircombe and T. D. Arber. Valis: A split-conservative scheme for the relativistic 2d vlasov–maxwell system. *Journal of Computational Physics*, 228(13):4773–4788, 2009.

[29] R.J. Goldston and P.H. Rutherford. *Introduction to Plasma Physics*. Taylor & Francis, 1995.

[30] S. Eliezer. The interaction of high-power lasers with plasmas. *Plasma Physics and Controlled Fusion*, 45(2):181, 2003.

[31] A.G. MacPhee, L. Divol, A.J. Kemp, K.U. Akli, F.N. Beg, C.D. Chen, H. Chen, D.S. Hey, R.J. Fedosejevs, R.R. Freeman, M. Henesian, M.H. Key, S. Le Pape, A. Link, T. Ma, A.J. Mackinnon, V.M. Ovchinnikov, P.K. Patel, T.W. Phillips, R.B. Stephens, M. Tabak, R. Town, Y. Y. Tsui, L.D. Van Woerkom, M.S. Wei, and S.C. Wilks. Limitation on prepulse level for cone-guided fast-ignition inertial confinement fusion. *Physical Review Letters*, 104:055002, Feb 2010.

[32] L. Divol, B.I. Cohen, E.A. Williams, A.B. Langdon, and B.F. Lasinski. Nonlinear saturation of stimulated brillouin scattering for long time scales. *Physics of Plasmas*, 10:3728, 2003.

[33] N. J. Sircombe, T. D. Arber, and R. O. Dendy. Aspects of electron acoustic wave physics in laser backscatter from plasmas. *Plasma physics and controlled fusion*, 48(8):1141, 2006.

[34] N.B. Delone and V.P. Kranov. *Multiphoton processes in atoms*, volume 13. Springer Verlag, 2000.

[35] L.V. Keldysh. Ionization in the field of a strong electromagnetic wave. *Soviet Physics JETP*, 20(5), 1965.

[36] F.A. Ilkov, J.E. Decker, and S.L. Chin. Ionization of atoms in the tunnelling regime with experimental evidence using hg atoms. *Journal of Physics B: Atomic, Molecular and Optical Physics*, 25:4005, 1992.

[37] R.W. Robinett. *Quantum mechanics*. Oxford University Press, second edition, 2006.

[38] M.V. Ammosov, N.B. Delone, and V.P. Krainov. Tunnel ionization of complex atoms and of atomic ions in an alternating electromagnetic field. *Soviet Physics JETP*, 64(6):1191–1194, 1986.

[39] P. Mulser, F. Cornolti, and D. Bauer. Modeling field ionization in an energy conserving form and resulting nonstandard fluid dynamics. *Physics of Plasmas*, 5(12):4466–4475, 1998.

[40] O. Buneman. Time-reversible difference procedures. *Journal of Computational Physics*, 1(4):517–535, 1967.

[41] JP Boris. Relativistic plasma simulation-optimization of a hybrid code. In *Proceedings of the Fourth Conference on Numerical Simulation of Plasmas, Naval Research Laboratory, Washington DC*, pages 3–67, 1970.

[42] K. Yee. Numerical solution of initial boundary value problems involving maxwell's equations in isotropic media. *Antennas and Propagation, IEEE Transactions on*, 14(3):302–307, 1966.

[43] A. Taflove and S.C. Hagness. *Computational Electrodynamics*. Artech House Boston, 1995.

[44] G.D. Smith. *Numerical solution of partial differential equations: finite difference methods*. Oxford University Press, USA, 1985.

[45] C.S. Brady, K. Bennett, M. Ramsay, N.J. Sircombe, A.A. Lawrence-Douglas, H. Schmitz, C.P. Ridgers, R. Duclous, T.D. Arber, A.R. Bell, and R.G. Evans. Stability and accuracy analysis of a modern PIC code. Journal of Computational Physics, 2013 (manuscript in preparation).

[46] E. Gabriel, G. Fagg, G. Bosilca, T. Angskun, J. Dongarra, J. Squyres, V. Sahay, P. Kambadur, B. Barrett, A. Lumsdaine, et al. Open mpi: Goals, concept, and

design of a next generation mpi implementation. *Recent Advances in Parallel Virtual Machine and Message Passing Interface*, pages 353–377, 2004.

[47] J. Villasenor and O. Buneman. Rigorous charge conservation for local electromagnetic field solvers. *Computer Physics Communications*, 69(2):306–316, 1992.

[48] Y. Sentoku and A.J. Kemp. Numerical methods for particle simulations at extreme densities and temperatures: Weighted particles, relativistic collisions and reduced currents. *Journal of Computational Physics*, 227(14):6846–6861, 2008.

[49] W.T. Silfvast and W.B. Bridges. *Laser fundamentals*. Cambridge University Press Cambridge, England, 1996.

[50] R.P.J. Town, A.R. Bell, and S.J. Rose. Fokker-planck simulations of short-pulse-laser–solid experiments. *Physical Review E*, 50(2):1413, 1994.

[51] A.M. Perelomov, V.S. Popov, and M.V. Terent'ev. Ionization of atoms in an alternating electric field. *Soviet Journal of Experimental and Theoretical Physics*, 23:924, 1966.

[52] W. Xiong and S.L. Chin. Tunnel ionization of k and xe atoms by an intense co2 laser. *Laser and Particle Beams*, 10(01):179–187, 1992.

[53] J.H. Posthumus, M.R. Thompson, L.J. Frasinski, and K. Codling. Molecular dissociative ionisation using a classical over-the-barrier approach. In *CONFERENCE SERIES-INSTITUTE OF PHYSICS*, volume 154, pages 298–307. IOP PUBLISHING LTD, 1997.

[54] A.K.F. Haque, M. Shahjahan, M.A. Uddin, M.A.R. Patoary, A.K. Basak, B.C. Saha, and F.B. Malik. Generalized kolbenstvedt model for electron impact ionization of the k-, l-and m-shell ions. *Physica Scripta*, 81:045301, 2010.

[55] M.A. Uddin, A.K. Basak, A. Islam, and F.B. Malik. Electron impact single ionization of light ionic targets with charge q¿ 2. *Journal of Physics B: Atomic, Molecular and Optical Physics*, 37:1909, 2004.

[56] A.K.F. Haque, M. Alfaz Uddin, A.K. Basak, K.R. Karim, B.C. Saha, and F.B. Malik. Electron impact ionization of m-shell atoms. *Physica Scripta*, 74:377, 2006.

[57] K.L. Bell, H.B. Gilbody, J.G. Hughes, A.E. Kingston, and F.J. Smith. Recommended data on the electron impact ionization of light atoms and ions. *Journal of Physical and Chemical Reference Data*, 12:891, 1983.

[58] Michal Gryziński. Classical theory of atomic collisions. i. theory of inelastic collisions. *Physical Review*, 138:A336–A358, Apr 1965.

[59] A.K.F. Haque, M.A. Uddin, A.K. Basak, K.R. Karim, B.C. Saha, and F.B. Malik. Electron-impact ionization of l-shell atomic species. *Physical Review A*, 73(5):052703, 2006.

[60] Y.K. Kim and M.E. Rudd. Binary-encounter-dipole model for electron-impact ionization. *Physical Review A*, 50(5):3954, 1994.

[61] M. Guerra, F. Parente, P. Indelicato, and J.P. Santos. Modified binary encounter bethe model for electron-impact ionization. *International Journal of Mass Spectrometry*, 2011.

[62] B.K. Thomas and JD Garcia. Ionization of positive ions. *Physical Review*, 179(1):94, 1969.

[63] W.L. Dunn and J.K. Shultis. *Exploring Monte Carlo Methods*. Elsevier Science, 2012.

[64] L. Devroye and L. Devroye. *Non-uniform random variate generation*, volume 4. Springer-Verlag New York, 1986.

[65] R. Nuter, L. Gremillet, E. Lefebvre, A. Lévy, T. Ceccotti, and P. Martin. Field ionization model implemented in particle in cell code and applied to laser-accelerated carbon ions. *Physics of Plasmas*, 18:033107, 2011.

[66] A.K.F. Haque, M.A. Uddin, M.A.R. Patoary, A.K. Basak, M.R. Talukder, B.C. Saha, K.R. Karim, and F.B. Malik. Generalized kolbenstvedt model for electron impact ionization of k-, l- and m-shell atoms. *The European Physical*

Journal D - Atomic, Molecular, Optical and Plasma Physics, 42:203–210, 2007. 10.1140/epjd/e2007-00029-5.

[67] K. Nanbu and S. Yonemura. Weighted particles in coulomb collision simulations based on the theory of a cumulative scattering angle. *Journal of Computational Physics*, 145(2):639 – 654, 1998.

[68] E. Lefebvre, A. Beck, M. Carrié, P. Combis, A. Compant-La-Fontaine, X. Davoine, J. Drouet, M. Drouin, A. Friou, L. Gremillet, et al. Calder: a versatile pic code suite for high-intensity laser-plasma interaction.

[69] T. Auguste, P. Monot, L.A. Lompré, G. Mainfray, and C. Manus. Defocusing effects of a picosecond terawatt laser pulse in an underdense plasma. *Optics Communications*, 89(2):145–148, 1992.

[70] P. Gibbon. *Short pulse laser interactions with matter*. Imperial College Press London, 2005.

[71] D. Bauer, P. Mulser, A. Macchi, E.C. Jarque, and R.R.E. Salomaa. Ultrafast ionization: Tdse calculations and intense laser pulse-solid interaction. *Laser Physics*, 9:58–68, 1999.

[72] S. Fourmaux, S. Payeur, P. Lassonde, J.C. Kieffer, and F. Martin. Laser pulse contrast ratio cleaning in 100 tw scale ti: Sapphire laser systems. 2011.

[73] J. D. Huba. *NRL Plasma Formulary*. Naval Research Laboratory, Washington, D. C., 2006.

[74] W. Manheimer, D. Colombant, and V. Goncharov. The development of a krook model for nonlocal transport in laser produced plasmas. i. basic theory. *Physics of Plasmas*, 15(8):083103, 2008.

[75] T. Tajima and J.M. Dawson. Laser electron accelerator. *Physical Review Letters*, 43(4):267–270, 1979.

[76] D. Umstadter, J.K. Kim, and E. Dodd. Laser injection of ultrashort electron pulses into wakefield plasma waves. *Physical Review Letters*, 76:2073–2076, Mar 1996.

[77] Pisin Chen, J.M. Dawson, Robert W. Huff, and T. Katsouleas. Acceleration of electrons by the interaction of a bunched electron beam with a plasma. *Physical Review Letters*, 54:693–696, Feb 1985.

[78] D. Umstadter, J. Kim, E. Esarey, E. Dodd, and T. Neubert. Resonantly laser-driven plasma waves for electron acceleration. *Physical Review E*, 51:3484–3497, Apr 1995.

[79] A. Modena, Z. Najmudin, A.E. Dangor, C.E. Clayton, K.A. Marsh, C. Joshi, V. Malka, C.B. Darrow, C. Danson, D. Neely, et al. Electron acceleration from the breaking of relativistic plasma waves. *Nature*, 377(6550):606–608, 1995.

[80] A. Pukhov and J. Meyer-ter Vehn. Laser wake field acceleration: the highly non-linear broken-wave regime. *Applied Physics B: Lasers and Optics*, 74(4):355–361, 2002.

[81] V. Malka, S. Fritzler, E. Lefebvre, M.M. Aleonard, F. Burgy, J.P. Chambaret, J.F. Chemin, K. Krushelnick, G. Malka, S.P.D. Mangles, et al. Electron acceleration by a wake field forced by an intense ultrashort laser pulse. *Science*, 298(5598):1596–1600, 2002.

[82] S. Banerjee, N.D. Powers, V. Ramanathan, I. Ghebregziabher, K.J. Brown, C.M. Maharjan, S. Chen, A. Beck, E. Lefebvre, S.Y. Kalmykov, et al. Generation of tunable, 100–800 mev quasi-monoenergetic electron beams from a laser-wakefield accelerator in the blowout regime. *Physics of Plasmas*, 19:056703, 2012.

[83] P. Brijesh, C. Thaury, K.T. Phuoc, S. Corde, G. Lambert, V. Malka, S.P.D. Mangles, M. Bloom, and S. Kneip. Tuning the electron energy by controlling the density perturbation position in laser plasma accelerators. *Physics of Plasmas*, 19(6):063104, 2012.

[84] S. Bulanov, N. Naumova, F. Pegoraro, and J. Sakai. Particle injection into the wave acceleration phase due to nonlinear wake wave breaking. *Physical Review E*, 58:R5257–R5260, Nov 1998.

[85] T.P. Rowlands-Rees, C. Kamperidis, S. Kneip, A.J. Gonsalves, S.P.D. Mangles, J.G. Gallacher, E. Brunetti, T. Ibbotson, C.D. Murphy, P.S. Foster, et al. Laser-driven acceleration of electrons in a partially ionized plasma channel. *Physical Review Letters*, 100(10):105005, 2008.

[86] H.C. Barr, P. Mason, and D.M. Parr. Electron parametric instabilities of relativistically intense laser light in under and overdense plasma. *Physics of Plasmas*, 7:2604, 2000.

[87] N. Kumar, V.K. Tripathi, and B.K. Sawhney. Filamentation of a relativistic short pulse laser in a plasma. *Physica Scripta*, 73:659, 2006.

[88] P. Kaw, G. Schmidt, and T. Wilcox. Filamentation and trapping of electromagnetic radiation in plasmas. *Physics of Fluids*, 16(9):1522–1525, 1973.

[89] P.K. Shukla, M.Y. Yu, and N.L. Tsintsadze. Intense solitary laser pulse propagation in a plasma. *Physics of Fluids*, 27(2):327–328, 1984.

[90] C.J. McKinstrie and R. Bingham. Stimulated raman forward scattering and the relativistic modulational instability of light waves in rarefied plasma. *Physics of Fluids B: Plasma Physics*, 4:2626, 1992.

[91] P.K. Shukla, R. Bharuthram, and N.L. Tsintsadze. Fully relativistic filamentation instability of strong electromagnetic radiation in unmagnetized plasmas. *Physica Scripta*, 38:578, 1988.

[92] A. Couairon and L. Bergé. Modeling the filamentation of ultra-short pulses in ionizing media. *Physics of Plasmas*, 7(1):193–209, 2000.

[93] M. Nurhuda and E. Van Groesen. Effects of delayed kerr nonlinearity and ionization on the filamentary ultrashort laser pulses in air. *Physical Review E*, 71(6):066502, 2005.

[94] P.L. Kelley. Self-focusing of optical beams. *Physical Review Letters*, 15(26):1005–1008, 1965.

[95] M.M. Marinak, R.E. Tipton, O.L. Landen, T.J. Murphy, P. Amendt, S.W. Haan, S.P. Hatchett, C.J. Keane, R. McEachern, and R. Wallace. Three-dimensional simulations of nova high growth factor capsule implosion experiments. *Physics of Plasmas*, 3(5):2070–2076, 1996.

[96] M.P. Mauldin, E. Giraldez, J.S. Jaquez, C.H. Shearer, R.B. Stephens, and D.M. Woodhouse. Fabrication of targets for proton focus cone fast ignition experiments. *Fusion Science and Technology*, 51(4):626–630, 2007.